

ISBN 978-82-326-6568-6 (printed ver.)
ISBN 978-82-326-6770-3 (electronic ver.)
ISSN 1503-8181 (printed ver.)
ISSN 2703-8084 (electronic ver.)

Doctoral theses at NTNU, 2021:306

Prashant S. Salimath

Numerical simulations of combustion near solid and hydrogen permeable walls

Doctoral theses at NTNU, 2021:306

NTNU
Norwegian University of
Science and Technology
Thesis for the degree of
Philosophiae Doctor
Faculty of Engineering
Department of Energy and Process Engineering

Prashant S. Salimath

Numerical simulations of combustion near solid and hydrogen permeable walls

Thesis for the degree of Philosophiae Doctor

Trondheim, 23rd of Sept 2021

Norwegian University of Science and Technology
Faculty of Engineering
Department of Energy and Process Engineering



Norwegian University of
Science and Technology

NTNU

Norwegian University of Science and Technology

Thesis for the degree of Philosophiae Doctor

Faculty of Engineering

Department of Energy and Process Engineering

© Prashant S. Salimath

ISBN 978-82-326-6568-6 (printed ver.)

ISBN 978-82-326-6770-3 (electronic ver.)

ISSN 1503-8181 (printed ver.)

ISSN 2703-8084 (electronic ver.)

Doctoral theses at NTNU, 2021:306



Printed by Skipnes Kommunikasjon AS

Dedicated to my parents, my wife Spurti and my daughter Manya.

"Time passes unhindered. When we make mistakes, we cannot turn the clock back and try again. All we can do is use the present well."

- His Holiness Dalai Lama, 14th Dalai Lama of Tibetan Buddhism.

Abstract

The goal of the present thesis was to investigate a selective and isothermal, chemically inert hydrogen-permeable or porous wall boundary condition to laminar flame simulations to understand the flow physics of near-wall flames. It provides better physical insight into a flame quenching process near a hydrogen-permeable wall, its relation to wall heat fluxes and incomplete combustion leading to pollutant formation. The simulation results are crucial to obtain prediction capabilities for eventual future utilization as novel fuel diffuser in a conventional combustor fuel nozzle. The comparison of the impermeable wall results with permeable wall results gives a good indicator towards building fuel diffuser and identifying a margin of operating conditions for improving hardware lifetime.

First, transient processes of laminar flame-wall interaction and quenching near a porous, permeable wall were investigated for the temperature of 750 K. These results were compared against a reference case of a non-porous or solid wall. The results obtained for lean, stoichiometric and rich initial mixture conditions in premixed flame show that flame wall characteristics (wall heat flux and quenching distance) are affected by the flux of hydrogen gas through a porous wall. The presence of a feedback mechanism was observed between hydrogen flux at wall and flame, which influences boundary layer flashback speeds in 2-d side wall quenching (SWQ) cases. The strong feedback effect was observed at lean-fuel conditions.

Then, a laminar 1-d head-on quenching (HOQ) of hydrogen-air mixture for the permeable wall was extended to study the effects of varying wall mass flux, stoichiometry, inert dilution and unburned-gas and wall temperatures. In all cases, the maximum reaction heat release rate occurred at the wall. For rich and stoichiometric mixtures, a moderate reduction of the quenching (i.e. maximum) wall heat flux to permeable wall in comparison to reference impermeable wall, whereas for a lean mixture, the increase of quenching wall heat flux was considerable. The lean permeable wall cases have similarities to much richer impermeable wall cases. Both a lower wall temperature and dilution reduce the burned-mixture temperature and, consequently, the wall

heat flux.

Furthermore, the flame wall interaction study with a hydrogen-permeable wall was extended to methane-air premixed flames. Permeable wall (PW) configurations were investigated for two temperatures at 600 and 750 K, of the wall and unburnt gas, and varying initial equivalence ratios. The solid wall results agreed with previous FWI studies. The mutual effects of convection heat transfer, flame behaviour and local fuel-air ratio, with reduced temperature and heat release rates, explain the flame quench before reaching the wall for PW cases. These effects were not observed for FWI of premixed hydrogen-air mixtures. The quenching definition of maximum heat flux was inappropriate to these cases. The OH radicals concentration was taken as a criterion for quenching definition and flame position.

Finally, the interaction of premixed hydrogen-air flame was extended to study local entropy generation and entropy fluxes towards a solid and hydrogen-permeable wall. Major findings were that conduction entropy generation remains dominant close to quenching, and that fuel permeation through the wall tends to reduce entropy generation per unit of converted fuel, particularly for initially lean mixtures.

Preface

This thesis is submitted to the Norwegian University of Science and Technology (NTNU) for partial fulfillment of the requirements for the degree of philosophiae doctor. This doctoral work has been performed at the Department of Energy and Process Engineering, NTNU, Trondheim, with Ivar S. Ertesvåg as main supervisor and Andrea Gruber as co-supervisor. The present work is conducted at NTNU, in close collaboration with SINTEF Energy Research.

This work is part of combustion under NTNU project CCERT (CO₂ Capture with Enabling Research and Technology), funded by the Research Council of Norway, Det Norske Veritas AS, Shell Technology Norway AS, StatOil Hydro AS and Metso Power OY.

Acknowledgements

I would like to express my deepest regards to my supervisor, Professor Ivar S. Ertesvåg, for trusting me to pursue my own ideas and thoughts, and for his continuous interest and support. Special thanks to Dr. Andrea Gruber for his valuable support in understanding of S3D code, fruitful discussions and inspiring enthusiasm. A very special thanks to Prof. Inge Gran, for initial years of supervising my work.

I am pleased to express my acknowledgement to Dr. Andrea Gruber for his co-operation and possibility on implementation of permeable wall boundary in S3D code. Many thanks to all my colleagues at Department of Energy and Process Engineering at NTNU.

Notur/The Norwegian e-infrastructure for Research and Education, Uninett Sigma, has provided the computational resources for the simulations (project No. nn9400k). Their HPC support team is thanked for all help and support in running the simulations. Special thanks to the supporting staff from IT department for their help and support with different IT issues.

Finally, my family also deserves special thanks for their support and understanding during these years of study.

Papers and Presentations

The thesis is based on following research articles.

Article 1. Andrea Gruber, **Prashant S. Salimath** and Jacqueline H.Chen, 2013, Direct Numerical simulation of 1-D and 2-D laminar flame-wall interaction for a novel H₂-selective membrane/injector configuration. *International Journal of Hydrogen Energy*, **39**, 5906-5918.

Article 2. **Prashant S. Salimath**, Ivar S. Ertesvåg and Andrea Gruber, 2018, Premixed hydrogen flames interacting with a hydrogen porous wall. *International Journal of Hydrogen Energy*, **43**, 3822-3836.

Article 3. **Prashant S. Salimath**, Ivar S. Ertesvåg and Andrea Gruber, 2020, Computational analysis of premixed methane-air flame interacting with a solid wall or a hydrogen porous wall. *Fuel*, **272**, 0016-2361.

Article 4. **Prashant S. Salimath** and Ivar S. Ertesvåg, 2020, Local entropy generation and entropy fluxes of a transient flame during head-on quenching towards solid and hydrogen-permeable porous walls. *International Journal of Hydrogen Energy*, **46**, 22616-26630.

Ivar S. Ertesvåg and Andrea Gruber are my main supervisor and co-supervisor, respectively.

Author's Contribution

The papers are co-authored. The author of the thesis has contributed to research work in the following :

Paper 1. The first author (Andrea Gruber) formulated the theoretical formalism of the permeable wall boundary conditions (BCs) while the second author (Prashant Salimath) conducted the first numerical implementation and testing of the BC in the S3D code. Further and final implementation of permeable wall BC in S3D was done by first author. The main contribution by second author to the article was on performing some of the numerical 1-d

DNS presented in the paper. The first author conceived an idea on flame back for 2-d SWQ (side-wall quenching) and performed 2-d DNS results in the paper and was responsible for writing the article with the interpretation of the results and discussion. The third author (Jacqueline Chen) contributed with suggestions and critical reviews.

Paper 2. The first author (Prashant Salimath) conducted all the numerical simulations of 1-d HOQ (head-on quenching) for the impermeable and hydrogen-permeable walls with design parameter variations (feed pressures, wall temperatures, equivalence ratios and dilution effects). The first author wrote the paper with the interpretation of the results and discussion. The second author (Ivar S. Ertesvåg) supervised the writing and article layout through discussions and suggestions. The third author (Andrea Gruber) contributed with critical reviews.

Paper 3. The first author (Prashant Salimath) conceived the idea of simulations of 1-d HOQ for methane flames with hydrogen permeable wall condition. The first author did all the numerical simulations and wrote the paper with the interpretation and discussion of the results. The second author (Ivar S. Ertesvåg) supervised the writing and article layout through discussions and suggestions. The third author (Andrea Gruber) contributed with critical reviews.

Paper 4. The first author (Prashant Salimath) conceived the idea of computing local entropy generation in 1-d HOQ for hydrogen flames with hydrogen permeable wall. The author also performed all numerical computations. The second author (Ivar S. Ertesvåg) was responsible for writing the paper with the interpretation and discussion of the results. The first author arranged numerical results in the article based on discussions, suggestions and critical reviews given by the second author.

Nomenclature

Acronyms

DNS	Direct Numerical Simulation
FWI	Flame-wall Interaction
HOQ	Head on Quenching
IW	Impermeable or Solid wall
PW	Permeable Wall
RHS	Right-hand side
SWQ	Side Wall Quenching

Greek Symbols

λ	thermal conductivity	J/(s·m·K)
μ	viscosity	Pa·s
ϕ	equivalence ratio	—
ρ	mass density	kg/m ³
$\tau_{\alpha\beta}$	viscous stress tensor	Pa

Latin Symbols

$C_p, C_{p,i}$	specific heat capacity at constant pressure (for species i)	J/(kg·K)
D_i^{mix}	mixture-averaged mass diffusivity of species i	m ² /s
D_i^T	thermal diffusion coefficient of species i	kg/(m·s)
F_i	wall flux for species i	kg/(s·m ²)
h_i	specific enthalpy for species i	J/kg
$J_{\alpha i}$	diffusive mass flux of species i in x_α direction	kg/(s·m ²)
L_x, L_y	spatial dimensions for axial and transverse direction	m
n	pressure exponent	—
N_{dim}	number of spatial dimensions	—
N_S	number of species	—
p, p_{ref}	pressure, reference pressure	Pa
Pe^*	Peclet number	—
Q''	hydrogen membrane permeance	kmol/(m·s·Pa ^{0.5})
q_α	heat flux in x_α direction	J/(s·m ²)
R	specific gas constant for the mixture	J/(kg·K)

S_L^0	laminar flame speed	m/s
t	time	s
T, T_0	temperature, ambient temperature	K
U	primitive variables solution vector	—
u_α	velocity component in x_α direction	m/s
W_i	molar mass of species i	kg/kmol
x, x_α	spatial coordinate	m
x^*, y^*	non-dimensional axial and transverse direction	—
y	spatial coordinate	m
Y_i	mass fraction of species i	—

Superscripts

f	hydrogen pressure on feed side
p	hydrogen pressure on permeate side

Subscripts

α, β	directional indices
b	property of the burnt mixture
u	property of the unburnt mixture
w	wall quantity

Contents

Abstract	iv
Preface	vi
Acknowledgements	vii
Papers and Presentations	viii
Contents	xiii
1 Introduction	1
1.1 Background and motivation	1
1.2 Objectives and research questions	6
1.3 The S3D code for computational fluid dynamics	8
1.4 Research Strategy and report layout	10
2 Models, boundary conditions and numerical methods	13
2.1 Mathematical models	13
2.2 Boundary conditions	14
2.2.1 Well-posed boundary conditions	14
2.2.2 Closed (wall) boundary conditions	15
2.3 Numerical methods	17
3 Summary of articles	18
3.1 Schematic outline	18
3.1.1 Article 1	20
3.1.2 Article 2	21
3.1.3 Article 3	22
3.1.4 Article 4	23
3.2 2-D side-wall quenching (SWQ) configuration	24
3.3 Discussion	28

4	Conclusions and further work	31
4.1	Summary	31
4.2	Future work	33
	Bibliography	42
	Appendices	43
A	Selected Papers	44
B	Chemical kinetics mechanism	108

Chapter 1

Introduction

1.1 Background and motivation

Human civilization has witnessed significant progress and development by the discovery of fire [1]. The controlled fire application as energy source made remarkable progress in human society in terms of historical pieces of evidence suggests that ancestors improved their food habits that eventually improved brain size and thinking abilities [2, 3]. Traditionally, fire has been used in various forms for heating, illumination and advanced craftsmanship, such as the development of metals [4, 5]. But as evolution progressed with time, the fire seemed to be an inadequate energy source, and alternative energy sources derived from fossil fuels were sought to meet growing energy demand. Nowadays, global energy figures indicate major concerns of by-products of combustion, leading to pollution, which has long-term environmental impact [6]. However, the availability of fossil fuels remains by a far major source of energy [7]. An increasing world population and fast pace development of third world countries led to a steep rise of the energy demand [8, 9]. The increase in energy demand began to grow further with the industrial revolution from the 18th century [10]. Until the end of the 19th century, energy demand was met by conventional fuels such as wood, charcoal and coal.

The discovery of oil and natural gas resources, significantly changed the dynamics of energy demand in the modern world [11]. The International Energy Agency (IEA) estimated that global energy consumption (including fossil fuels, renewable, nuclear and bio fuels) grew by 2.3% worldwide in 2018, which is near twice the average growth rate since 2010. The global energy consumption is largely driven by a robust economy and also higher heating and cooling needs in some parts of the world. The latter lead to an increase of the CO₂ emissions to 33.1 giga-tonnes from 2010 to 2018, which is equal to 1.7% [8]. The coal-fired power generation remains to be the single largest emitter, accounting for 30% of all energy-related carbon dioxide emissions. This results to an increase of emissions due to the release of local and global pollutants [12]. The rising energy demand trend in World Energy Outlook (WEO) suggest a 37% increase in coming 2040 as compared to 2014 [8]. WEO indicated that developed countries are stable in energy demand. In contrast, developing countries with a huge population, such as China and India, show unexpected higher energy demand in coming years [8]. Also, calculation suggests that fossil fuel reserves of oil and gas can last till 2042 and coal reserves are available up to 2112, according to Shafiee and Topal [13]. In the coming 20 years, current technology may not be relevant as oil and gas as a primary energy source may get exhausted.

Alternative renewable energies are looked upon to reduce the dependency on fossil fuels. However, in the recent years they still did not provide an attractive option to replace fossil fuels. It is predicted that dominant energy sources will still be based on oil, gas, coal and low-carbon sources, with little change in their share of total consumption [14]. The effective campaign to reduce dependency on fossil fuels and greenhouse gas emissions has not been stringent across the world. The 1997 Kyoto protocol and its signatories have not fulfilled the commitments towards reducing greenhouse emissions [15]. Although various efforts have made to reduce fossil fuels dependence by 25% to current available technologies available, it may not be enough to reduce the global greenhouse effects. If emissions continue to increase at the current rate, the atmosphere will warm up by 1.5 degrees Celsius above pre-industrial levels by 2040 [16]. The consequences are coastlines flooding

and exacerbation of droughts and poverty.

It is becoming an alarming issue to attenuate temperature increase to below 2 degrees Celsius and less than 1000 giga-tonnes of CO₂ emissions to avoid climatic changes and natural calamities. From 2014, various organizations such as Advisory Council for Aviation Research and Innovation in Europe (ACARE) set in with stricter norms on emissions to mitigate 20% of CO₂ and NO_x by 80% per passenger [17].

In the present-day situation, available energy fuel sources produce greenhouse gas emissions. There have been significant efforts put into large scale implementation of carbon capture and storage (CCS) technologies to reduce fossil-based CO₂ emissions. CCS is considered a crucial strategy for meeting CO₂ reduction targets for fossil fuels [18, 19, 20]. Most studies concluded that the costs of pre-combustion CO₂ capture from syngas in an integrated gasification combined cycle (IGCC) plant were much lower than post-combustion removal from pulverized coal (PC) or natural gas combined cycle (NGCC) plants [21, 22, 23]. One of the common strategies employed in stationary gas turbine power generation is to opt for pre-treatment of natural gas fuel, as it contains mainly methane gas. The methane gas is reformed to a syngas containing H₂ and CO [24]. The hydrogen content can be increased by the water-gas shift reaction with low CO gas content. However, the downside of considering the pre-combustion CCS technologies as an option, is that it adds costs to process, which comes from the procurement of reforming and H₂ separation units [25]. Current technology concepts available use the auto-thermal reforming (ATR) with water-gas shift reaction reactors to produce hydrogen-rich syngas from natural gas, and CO₂ produced is separated further by adsorption [26]. There is one potentially more efficient alternative introduced of hydrogen transport membrane (HTM) [27]. In HTM, water shift reaction and hydrogen separation from CO₂ are combined in the same unit [28, 29]. The hydrogen gas produced is further utilized as a fuel source mixed with compressed inert diluent, i.e. nitrogen, for the burner. The addition of diluent reduces the reactivity of hydrogen as it flows out of the fuel injection nozzles and mixes with the

compressed hot air. In the pre-mixed burner, the diluent provides flashback safety for reactive H_2 fuel.

Industrial gas turbines commonly utilize lean pre-mixed burners for NO_x control using low reactivity fuels, such as natural gas [30]. These conventional gas-fuel injector nozzles usually operate in a transverse-jet configuration, where fuel exiting the nozzle mixes with approaching oxidant at an angle that is approximately normal to the oxidant flow [31]. However, although transverse-jet nozzles typically achieve good flow penetration and mixing of the fuel in the oxidant flow, they also result in a low-velocity flow region on the leeward side of the jet. This is especially problematic in the case of the highly-reactive hydrogen fuel due to the possibility of flame attachment directly at the nozzle exit and lack of intrinsic flashback resistance (the flame is flushed downstream once the instability that displaced it upstream recedes).

Lean pre-mixed burners were originally designed for natural gas applications. Subjecting burners to a modification to accommodate more reactive fuels, such as hydrogen, leads to significant design challenges for achieving acceptable flame stability. The technical difficulties of burner handling reactive fuel are to avoid the occurrence of (a) flame flashback, an undesired event of upstream flame propagation in the premixed section of the burner and along the wall surfaces of the nozzle due to aerodynamic effects [32], and (b) stable flame anchoring near-wall surface of injection nozzles due to the presence of local fuel-rich conditions [33, 34].

In the present study, a novel burner concept development is envisaged as shown in Fig. 1.1 for a stationary gas turbine that operates as a porous diffuser coated with an H_2 selective membrane that can operate in a lean premixed mode. The porous fuel diffuser has the potential to replace conventional gaseous fuel nozzles with holes for injection, thereby avoiding point fuel sources of highly reactive H_2 fuel. In the porous diffuser, an H_2 flux can be supplied based on the high pressure difference between feed and permeate side of the membrane leading to a uniform diffusion of the fuel. The porous ceramic or steel can act as opportunely shaped diffusers. A recent

experimental study investigated the effects on premixed flame shape and stabilization of a novel approach for spatially distributed reactive hydrogen fuel injection through a porous steel surface integrated into the burner design [35]. However, great care must be taken in designing primary air flow interacting with a permeable wall surface to quickly remove reactive H_2 from the near wall region to avoid flashback of the flame and flame anchoring near the immediate vicinity of fuel injection. Other construction details of the novel burner are left out in the scope of present work and are not discussed.

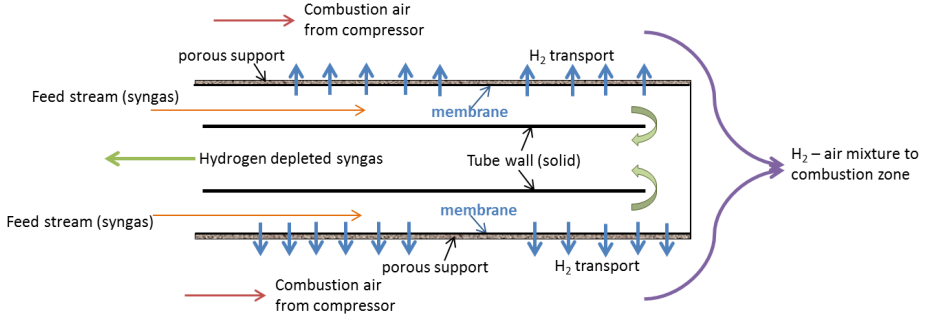


Figure 1.1: Fuel injector sketch with in-situ separation of hydrogen gas from syngas. Adapted from Article 1.

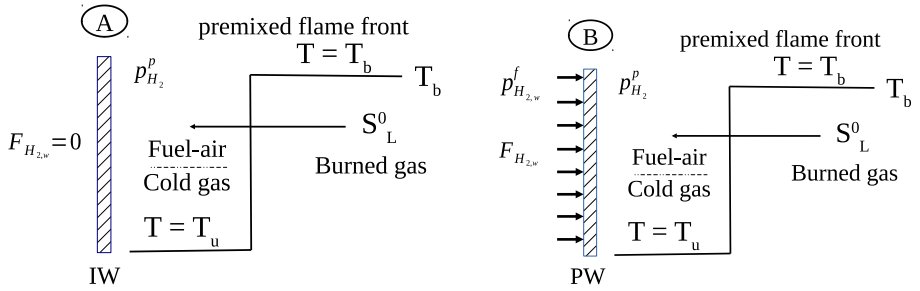


Figure 1.2: Head-on quenching configurations of (a) Impermeable wall (IW) and (b) Permeable wall (PW) with hydrogen flux. Premixed fuel can be hydrogen or methane gas.

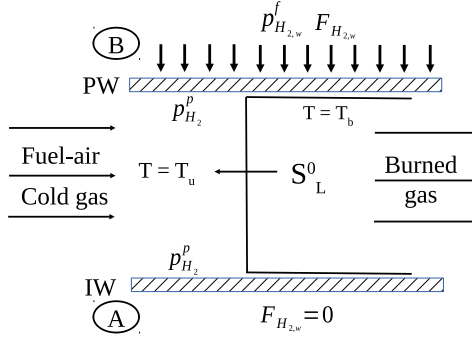


Figure 1.3: Side-wall quenching configurations of (a) Impermeable wall (IW) and (b) Permeable wall (PW) with hydrogen flux. Premixed fuel can be hydrogen or methane gas.

1.2 Objectives and research questions

Combustion near a high-temperature membrane surface with the fuel supply has the important feature of lowering the partial pressure of species consumed in the combustion process, leading to a larger driving force across the membrane. The use of membranes opens for novel applications in porous fuel nozzle design in gas turbine development such as nano or micro combustion, where wall effects are significant.

The primary aim of the work is to improve the understanding of combustion close to a porous wall. Novel designs demand particular attention to flame-wall interaction processes to understand combustion inefficiencies such as poor mixing, incomplete combustion and high wall heat flux. The main focus of the investigations will be laminar flame-wall interactions (FWI) of premixed flames with the PW in the head-on quenching (HOQ) configurations (Fig. 1.2) for laminar premixed flames of hydrogen-air and methane-air mixtures. This study will provide better estimates of wall heat flux characteristics and H_2 fluxes for operating conditions for varying fuel-air conditions, wall temperatures and diluents effects. In FWI simulations, no previous reports or literature were available on hydrogen-PW simulations. The results will be compared against reference IW cases as both walls are

will be kept isothermal and chemically inert. Laminar side-wall quenching (SWQ) as shown in Fig. 1.3 was performed to assess boundary layer flashback resulting from the feedback mechanism between membrane hydrogen flux and the propagating flame for hydrogen-air mixture.

The following research questions were addressed in the articles:

- *How does PW influence near-wall flame behaviour and flame quenching characteristics compared to IW in hydrogen-air mixtures? How do design parameter variations affect flames during the flame quenching process in PW hydrogen-air flames?*

It can be anticipated that hydrogen permeation through a PW will influence the flame behaviour and change the characteristics compared to IW. Article 1 will investigate some aspects of 1-d and 2-d cases, while Article 2 will extend the 1-d study at different stoichiometries with varying permeation pressure (wall mass flux), unburnt and wall temperature, and dilution of the hydrogen-air mixture.

- *How does hydrogen wall permeation into a methane-air mixture affect the near-wall flame behaviour and head-on quenching characteristics?*

In Article 3, hydrogen PW injection into methane-air will be investigated and compared to the corresponding IW cases.

- *How does fuel permeation through the wall influence entropy generation in the transient flame quenching process ?*

The entropy generation expresses the thermodynamic losses in the process and is important for energy conversion optimization. Article 4 will investigate the entropy generation for PW and IW cases from Article 2.

1.3 The S3D code for computational fluid dynamics

In the present work, implementation of wall boundary condition with selective hydrogen species permeability was performed in the S3D code. The permeable-wall (PW) boundary condition implementation is based on Sieverts' law of diffusion [27]. The numerical simulations were performed in S3D using high-order finite-difference stencils and numerics [36].

S3D is a Fortran-based direct numerical simulation (DNS) code. It was developed under a research program of the United States Department of Energy (DoE) at the Combustion Research Facility (Livermore, CA). The code is programmed in Fortran F77/F90 code that uses message passing interface (MPI) for inter-process communication in parallel execution. The code is portable to different platforms /architectures including Linux clustres, IBM SP, Windows PC, Cray DEC, SGI Origin and DEC Alpha clustres. This code has been successfully used previously for a range of studies, including non-premixed flames [31, 33, 34, 37], premixed flames [38, 39, 40, 41, 42] and autoignition [43, 44].

Fig. 1.4 displays a flow diagram of S3D. The structural procedures are described in this section [45, 46]. The implemented algorithm solves compressible Navier-Stokes equations in the conservative form on a structured grid mesh in 1, 2 or 3 spatial directions. The structured code runs in either an execute-in-the-run mode ('0') or a post-processing mode ('1'). However, the post-processing mode can run only when time sampling data are available from prior run-mode simulations.

The code integrates the governing equations in run mode forward in time. All necessary operations are directed by routine solve driver code for a case-specific initialization of the primitive variables. After the initialization of the primitive variables, three components of transport equations convective, diffusive and source terms update for each time step in the conservation equations by high order time advancement solver of Runge-Kutta scheme [47]. In post-processing mode, the code executes with the same processor topology as in the run mode, but all required operations are directed by

the post-driver routine. The main kernels for solver accounts for 95% of the computation.

The following is a list of main kernels given below:

- Chemistry module: This module computes source terms of species transport equations that are chemical reaction rates. The "getrates" code, generated by the Chemkin compatible utility auto-getrates package, preprocesses the chemical kinetics data and computes reaction rates. A separate module is built for routines to be packaged and interfaced to the S3D code. This module abstracts the actual implementation of the reaction rates computation, and it also offers flexibility to use different versions of the getrates subroutine targeted at different platforms.
- Transport module: This module computes species molecular transport properties. Transport properties include viscosity, thermal diffusivity and species mass diffusivities. The chemical reactions and transport coefficients are calculated from CHEMKIN and TRANSPORT packages respectively [48]. The scalar transport properties are approximated with a constant Lewis number for each species or referred to as mixture averaged properties. Soret effect or thermo-diffusion and pressure diffusion terms are included, but the Dufour effect is neglected.
- Thermodynamics module: Computes thermodynamic properties that include species enthalpy and specific heats of the mixture. Thermodynamic data are provided to Chemkin compatible format. The pre-processing of data is performed through the chemkin interpreter. The evaluation of properties using the chemkin routines, the code employs a tabulation and lookup strategy.
- Derivatives module: This module computes spatial derivatives of the primitive variables from conserved variables. It uses high-order finite-difference operators of eighth order, A finite difference explicit scheme is used with tenth-order explicit spatial filter ([49]) to remove spurious

high-frequency noise and mitigate aliasing error. The code uses non-blocking sends and receives to exchange the data at the processor boundaries among different processors.

- Other RHS module: Fig. 1.5 shows right-hand side (RHS) of the time advance equation which involves all of the operations mentioned above and the convection terms. These terms summed up, and operations involved in this procedure are lumped into the RHS module for accounting purposes.
- Time Integration module: It advances the solution in time using a six-stage, fourth-order explicit Runge-Kutta scheme [47]. This module also includes an error controller, which routinely checks through proportional-integral-derivative (PID) to achieve optimal time steps and time accuracy of the solution with desired error tolerances.

More details on chemical source terms and thermodynamics and equations description can be found in [36] and Articles 2 and 3.

The present simulations were performed in the Vilje cluster. This cluster belongs to the Norwegian e-infrastructure for Research and Education, UNINETT Sigma2, which is funded by the Research Council of Norway, NTNU and the Universities of Oslo, Bergen and Tromsø. It offers a distributed memory system that is well suited for large scale parallel MPI applications. It consists of 1440 nodes interconnected with a high-bandwidth low-latency switch network (FDR Infiniband). Each node has two 8-core Intel Sandy Bridge (2.6 Ghz) and 32 GB memory. The total number of cores is 23040.

1.4 Research Strategy and report layout

The S3D DNS code is used to perform the transient simulations of laminar flame propagation towards the wall. The reactive flow is simulated, taking into account of thermo-physical properties. The detailed chemical

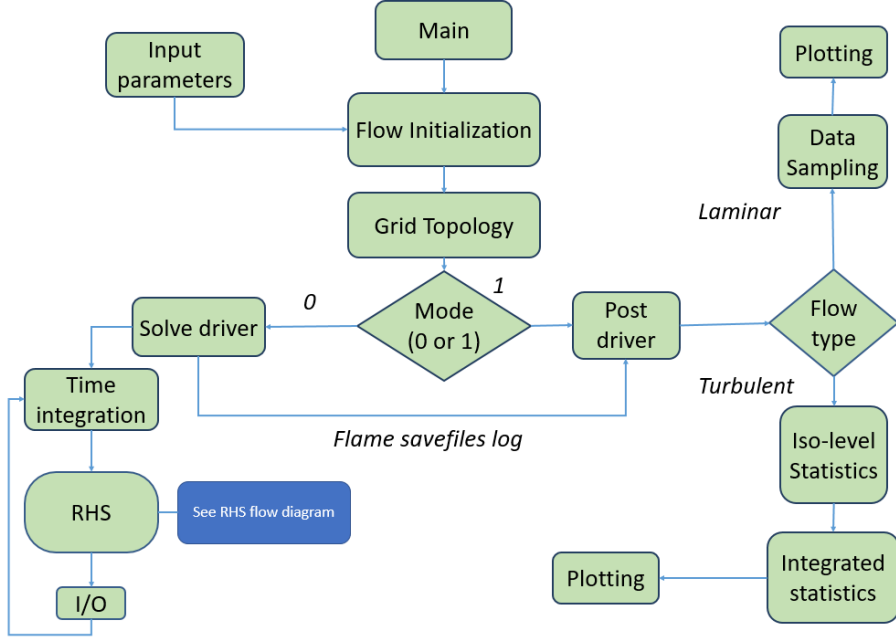


Figure 1.4: S3D code: Main program flow diagram.

kinetics is enabled to capture radical recombination reactions characterized by low activation energies in near-wall region. It was observed that modelling of quenching process with single-step chemistry approximation in previous FWI studies led to considerable uncertainties in flame quenching characteristics, which could adversely influence to other physical quantities characterizing the flow [50, 51].

The flame interaction with "cold" walls (< 400 K) results in water condensation effects are observed by [52]. This condensation of water can act as a possible reducing factor for wall heat flux. Also, wall temperatures above 400 K as "hot" wall depend upon material type and can influence as a catalyst through radical absorption, desorption and recombination, which can play an important role in the flame-wall interaction processes. However, in the present simulations, wall surfaces are assumed as an chemically inert wall and an isothermal wall condition is maintained. Both water condensation and surface kinetics are absent at the wall in the present study. This

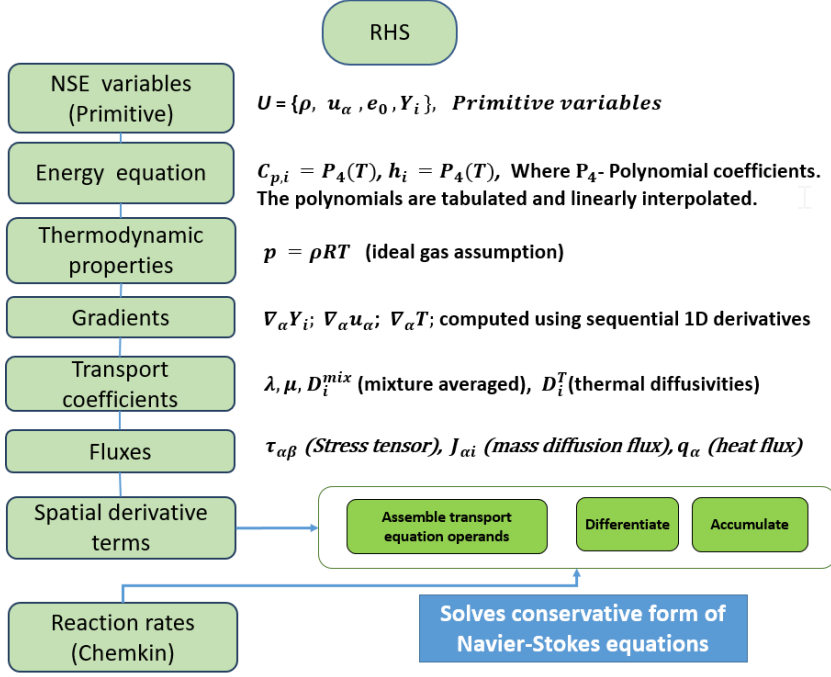


Figure 1.5: S3D RHS module : Flow diagram.

makes the conclusions of results produced independent of any particular properties of the wall surface material.

In the permeable wall boundary, the permeability of reactive hydrogen gas depends upon partial pressure difference between feed and permeate side of the wall. High pressure at the feed side is maintained at a maximum of 10 atm as the largest value in present simulations, which ensures optimum hydrogen flow rates across the wall.

The mathematical background description of governing equations, wall boundary condition formulation and numerical methods are described in Chapter 2. Chapter 3 presents the summary and contribution as articles published, and Chapter 4 is the conclusion of research work, and further work is described. The appendix includes of the peer-reviewed published papers and the chemical kinetics mechanism of hydrogen-air and methane-air.

Chapter 2

Models, boundary conditions and numerical methods

For laminar FWI studies in S3D code, Navier-Stokes equations are solved for subsonic, reacting compressible flow conditions.

2.1 Mathematical models

The governing equations, thermodynamic and transport properties are described in each article and not repeated here.

Numerical integration of governing equations as a system of partial differential equations gives the solution vector of conserved variables. Further, primitive variables solution vector is computed, U as :

$$U = (\rho, u_\alpha, p, T, Y_i)^t \quad \alpha = 1, 2, 3 \quad i = 1, 2, \dots, N_S \quad (2.1)$$

2.2 Boundary conditions

The governing equations are a coupled system of non-linear partial differential equations. Their solution for a specific flow configuration is strongly dependent upon the specification of boundary conditions at computational domain boundaries and initial conditions for all flow variables in the entire field.

2.2.1 Well-posed boundary conditions

In DNS, special care is required for the boundary conditions specification to meet objectives: (1) to represent the flow physics of the near-wall region or nature of turbulent flow conditions, and (2) compatible with high-order numerical schemes for spatial and temporal discretization [53]. For well-posedness for solving fluid flow problem, boundary conditions are distinguished into physical boundary conditions and artificial boundary conditions. The artificial boundary conditions are required to satisfy the well-posedness condition. Such boundary conditions are often difficult to formulate and act as complementary relations along with physical boundary conditions.

Table 2.1 lists boundary conditions required for well-posedness to solve Navier-Stokes equations and Euler (non-viscous) equations [54, 55, 56].

Table 2.1: Number of boundary conditions required well-posedness for the Euler and Navier-Stokes equations.

Flow type	Euler	Navier-Stokes
Supersonic inflow	$N_{\text{dim}} + 2 + (N_S - 1)$	$N_{\text{dim}} + 2 + (N_S - 1)$
Sonic inflow	$N_{\text{dim}} + 1 + (N_S - 1)$	$N_{\text{dim}} + 2 + (N_S - 1)$
Subsonic inflow	$N_{\text{dim}} + 1 + (N_S - 1)$	$N_{\text{dim}} + 2 + (N_S - 1)$
Subsonic outflow	1	$N_{\text{dim}} + 1 + (N_S - 1)$
Sonic outflow	0	$N_{\text{dim}} + 1 + (N_S - 1)$
Supersonic outflow	0	$N_{\text{dim}} + 1 + (N_S - 1)$
No flow	1	$N_{\text{dim}} + 1 + (N_S - 1)$

The physical boundaries are categorized into open and closed boundaries. In open boundaries, inflow and outflow boundary conditions are widely used in practical applications [57, 58, 59, 60]. The characteristic boundary condition (NSCBC) method is used to describe non-reflective pressure waves in open boundaries and represents an artificial cut through the flow field at both ends of the domain. In closed boundaries, there is no flow across the boundary, which represents wall condition in practical applications. The following section discusses boundary conditions treatment for wall boundaries. The radiative heat transfer is neglected in the wall boundary formulation.

2.2.2 Closed (wall) boundary conditions

In wall-bounded flows, wall boundaries play a dominant role in the FWI process. The presence of a wall boundary influences the local chemistry in the near-wall region, leading to a large wall heat release at quenching of the flame. In the following, wall formulations of an impermeable wall (IW) and a hydrogen permeable wall (PW) boundaries are discussed.

A number of $N_{\text{dim}} + 1 + (N_S - 1)$ of physical boundary conditions are required to satisfy well-posedness for an inert, isothermal, no-slip wall boundary. These conditions are applied to Navier-Stokes equations for a compressible gas mixture. One may write these as :

$$u_\alpha = 0, \quad T_w = T_u, \quad F_i = 0 \quad i = 1, 2, \dots, N_S \quad (2.2)$$

The species flux condition satisfies impermeability condition for IW, where $F_i = 0$ for all species i . For PW, $F_i = 0$ except $i = \text{H}_2$.

When applied to the momentum equation (with no body forces), the immediate consequences are for the IW formulation :

$$\frac{\partial u_\alpha}{\partial t} = \frac{Du_\alpha}{Dt} = 0, \quad \left(\frac{\partial p}{\partial x} \right)_w = \frac{\partial \tau_{\alpha\beta}}{\partial x}, \quad (2.3)$$

Numerical inversion of the pressure gradient expression, will yield the pres-

sure at the wall (p_w). Similarly, the species mass fraction at the wall ($Y_{i,w}$) are extracted by inverting the wall species gradient term.

With known values of p_w , $Y_{i,w}$ and T_w , the fluid density at wall node, ρ_w is computed from the equation of state. In summary, this wall formulation is applicable for solid or IW boundary conditions. This formulation has been widely used in wall-bounded flow studies with the S3D code [31, 33, 34, 38, 39].

For the PW formulation, a selective H_2 species flux condition is limited by diffusion and is modelled by :

$$F_{H_2} = W_{H_2} Q'' \left((p_{H_2}^f)^n - (p_{H_2}^p)^n \right) \quad (2.4)$$

The re-arranged Fick's law expression gives the species mass fraction gradient at the wall and it is given as:

$$\left(\frac{\partial Y_i}{\partial x} \right)_w = \frac{F_i}{\rho_w D_{i,w}^{\text{mix}}} \quad (2.5)$$

Note that all species except H_2 follow the species impermeability condition in Eq. 2.2.

Owing to species flux, the pressure at the wall is updated by re-arranging the momentum equation leading to:

$$\left(\frac{\partial p}{\partial x} \right)_w = - \sum_{i=1}^{N_s} \frac{\partial F_i}{\partial t} - \frac{\partial u_1}{\partial x} \sum_{i=1}^{N_s} F_i + \frac{\partial \tau_{\alpha\beta}}{\partial x} \quad (2.6)$$

The first and second RHS terms represent the unsteady and steady contributions to the wall-normal momentum of the PW hydrogen flux. Here, u_1 is the non-zero wall-normal velocity component due to hydrogen permeation. The new values of Y_i and p_w are extracted by inverting (numerically) Eq. 2.5 and Eq. 2.6, respectively. Then, density at the wall, ρ_w can be computed from the equation of state.

2.3 Numerical methods

The high-order finite-difference schemes are employed in S3D code because of their lower computing costs than those of high-order finite-volume methods [61, 62]. The high-order finite difference schemes including one-sided stencils for wall boundaries, filtering and temporal discretization details are discussed in [63] and are not repeated here.

Chapter 3

Summary of articles

The main contribution to research work is compiled into four papers which are submitted/published in peer-review journals.

3.1 Schematic outline

The author contributions are highlighted in Fig [3.1](#), and an overview of the key points in each article is summarised. Article 1 is a starting point with the implementation of PW boundary conditions in 1-d HOQ and 2-d SWQ configurations for understanding near-wall physics. It also offers forking paths (I and II) of FWI studies into Articles 2 and 3 for hydrogen-air and methane-air mixtures, respectively. Article 4 extends the Article 2 study with computations of entropy terms or irreversibilities during the transient flame quenching process.

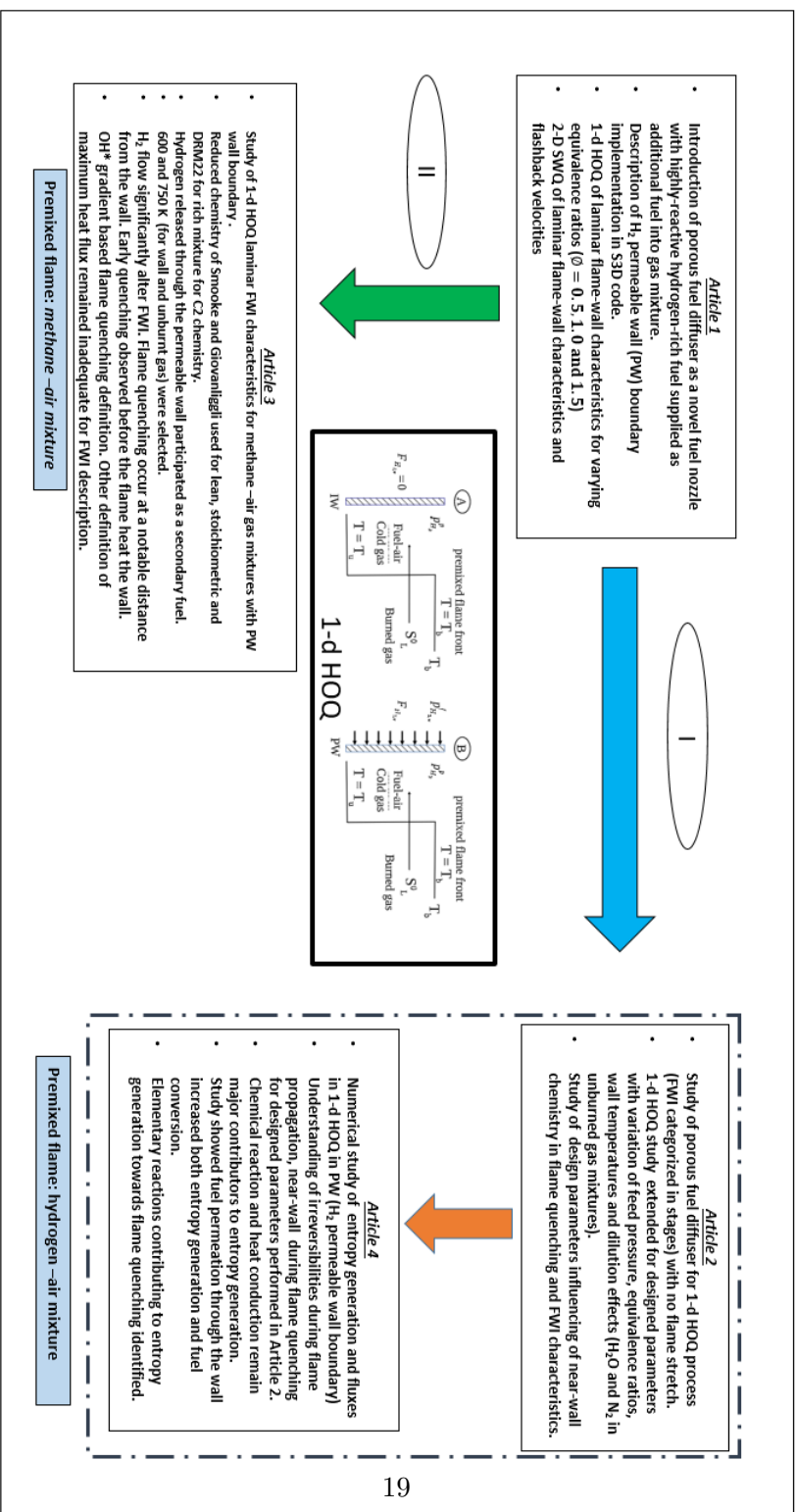


Figure 3.1: Outline of the scientific articles

3.1.1 Article 1

Title : Direct numerical simulation of laminar flame–wall interaction for a novel H_2 selective membrane injector configuration.

Co-Authors: Andrea Gruber and Jacqueline H. Chen

In this paper, transient simulations of laminar flame-wall interaction and quenching near a porous, permeable membrane wall (PW) for 1-d HOQ and 2-d SWQ configurations are presented. The comparison of these results is conducted with the reference case of a non-porous impermeable wall condition. The simulations were performed using S3D DNS (Direct Numerical Simulation) code [36] with detailed chemkin kinetics of hydrogen-air combustion [64]. The main aim of the study to future utilization of porous metal surfaces (or porous fuel diffuser) as a fuel distributing source for H_2 injection into the oxidant stream of a gas turbine burner. Also, understanding of near-wall flow physics of PW for highly-reactive hydrogen-rich fuels in the feed side. The PW wall boundary condition formulation is based on modelling selective species (hydrogen in this case) transport through a porous wall is discussed. The hydrogen flux of PW is driven by the partial pressure difference between the feed and the permeate side of the membrane. The numerical results are performed for 3 cases: lean, stoichiometric and rich initial mixture conditions on the permeate side of the membrane. It was observed that FWI characteristic parameters (wall heat flux, quenching distance) are affected to a large extent by the presence of the membrane. It is shown that quenching wall heat flux is increased by a factor of three for the (initially) fuel-lean premixed flame 0.5 in the presence of PW compared to the standard IW case. The high wall heat flux is due to the higher flame temperature attained in the near-wall region immediately before quenching and to the presence, in the initial mixture, of excess oxygen that continues to burn in a secondary non-premixed flame after quenching of the primary premixed flame. The hydrogen flux through the membrane is also strongly affected by the presence of the flame during the transient flame-wall interaction process, finally resulting in a strong feedback effect between membrane and flame that greatly increases boundary layer flashback speeds at fuel-lean

conditions. The paper suggests to having carefully designed fuel diffuser to remove hydrogen rapidly near-wall region of the permeate side of PW and mixing with oxidant more uniformly to achieve target fuel-air mixture. This work provide a starting point for understanding the interaction of PW for 1-d HOQ for different design parameters, as discussed in article 2.

3.1.2 Article 2

Title : Premixed hydrogen-air flames interacting with a hydrogen porous wall.

Co-Authors: Ivar S. Ertesvåg and Andrea Gruber

In this paper, a laminar 1-d hydrogen-air flame travelling and quenching towards a chemically inert permeable wall (PW) was studied for designed parameter variations (effects of varying wall mass flux, stoichiometry, inert dilution, and unburned gas and wall temperatures). H_2 as additional fuel seeped through the permeable wall into premixed H_2 -air mixtures based on partial pressure difference of feed and permeate side. All simulations were performed with detailed hydrogen-air chemistry in S3D code [36, 64]. These results are compared against the results of an impermeable wall (IW). All cases, maximum reaction heat release rates at the wall was observed. For rich and stoichiometric mixtures, PW with fuel influx gave a moderate reduction of the quenching (i.e. maximum) wall heat flux compared to IW. In contrast, for a lean mixture, the increase is considerable. The fuel influx effect on the importance of individual elementary reactions and radicals and intermediate species for rich and stoichiometric mixtures. The hydrogen permeation in PW led to locally richer flame (i.e. partially premixed mixture formation). It can be observed that more H radicals and less O radicals are present close to the wall and exothermic reaction recombining H to H_2 is considerably more important for PW. This consumption of H inhibits the more exothermic reaction of OH and H to H_2O . This overall influence early wall effects with more distant from the wall than for IW. Both a lower initial temperature and dilution with H_2 (inert) or H_2O (participating) reduce the

burned-mixture temperature and, consequently, the wall heat flux. Also, flame propagation and quenching are delayed.

3.1.3 Article 3

Title : Computational analysis of premixed methane-air flame interacting with a solid wall or a hydrogen porous wall

Co-Authors: Ivar S. Ertesvåg and Andrea Gruber

The objective of the paper was an investigation of flame-wall interaction process for premixed methane-air flames by direct numerical simulation using S3D code. Canonical configuration of 1-d HOQ with an isothermal, chemically inert impermeable wall (IW) and a hydrogen-permeable wall (PW) was taken with two temperatures of 600, and 750 K (of the wall and unburnt gas kept at the same temperature) were selected for the present study. Hydrogen released through the PW participated in the methane-air combustion as a secondary fuel.

For lean and stoichiometric mixtures, the reduced chemical mechanism of Smooke and Giovangigli (with slightly modified parameters) was used for simulations [65]. The mechanism does not include C2-chemistry but produced satisfactory results. For rich methane-air mixtures, the DRM22 mechanism was used that includes C2-chemistry [66]. For the permeable wall, the hydrogen gas flow significantly altered the flame-wall interactions with quenching occurring at a considerable distance from the wall. It was apparent that this was neither due to lack of oxidizer nor to heat loss to the wall and flame quenching took place before the flame heated the wall. The early quenching appeared to be a result of the mutual effects of the large local concentration of H_2 , reduced flame temperature and increased convective heat transfer away from the wall and flame. When the flame approached the wall and the increasing H_2 concentration, OH accumulation was reduced before other species (but O_2) were affected. After quenching, some modest reaction heat release still took place near the wall, and this gave a peak wall

heat flux a while after the quenching instance, although much less than for the impermeable wall. The discussion of quenching definitions showed that some are applicable to the PW case. The flame quenching instance was based on the OH gradient in the present study [67]. Also, definitions based on maximum reaction heat release and of the minimum flame thickness appeared applicable. On the other hand, the definition based on maximum wall heat flux failed to capture the cease of major reaction heat release.

3.1.4 Article 4

Title: Local entropy generation and entropy fluxes of a transient flame during head-on quenching towards solid and hydrogen-permeable porous walls

Co-Author: Ivar S. Ertesvåg

This paper presents further investigations of article 1 and 2 on 1-d HOQ premixed H_2 -air flame interacting with an impermeable wall (IW) or a permeable wall (PW) on the computation of local entropy generation and entropy fluxes. The calculation of entropy components was performed through solving post-processing subroutines in S3D code with the detailed chemical mechanism of 19 elementary reactions to identify major reactions contribution to entropy during flame quenching process [68]. The aim of the present study understands near-wall irreversibilities during the HOQ process.

Fuel permeation through the wall aid to increase both entropy generation and fuel conversion. The fuel permeation fuel had a diversity of effects near-wall region. First, it had a cooling effect on the near-wall region. Separately, thermal dilution subsides the local temperature and contribute to increased entropy generation. However, for initially lean and stoichiometric mixtures, the additional fuel provided more reaction heat release, leading to a higher temperature and reduced entropy generation per unit of converted fuel.

Permeation also increased the mass flux, and thereby the entropy flux, away from the wall. The effects of mass diffusion on entropy generation were

modest, and the altered mass diffusion made small changes from IW to PW. The Soret diffusion (thermodiffusion) had a small contribution to the mass diffusion entropy generation. During quenching, it became even smaller for IW, while it had an increase for PW. The effects of pressure diffusion were negligible. The effects of permeation were similar for all unburnt-temperatures investigated (750 K, 500 K, 300 K). As expected from theory and other studies, a lower temperature gave higher entropy generation.

In transient FWI entropy, the chemical reaction gave the major part of entropy generation, with conduction as the second most important source in accordance with previous literature. Mass diffusion was of modest importance, while viscous forces were negligible effects—the reduced entropy generation per unit of fuel converted to a lean mixture. The effect was stronger for lower temperatures because then the conduction had a greater share of the total entropy generation. At the higher unburnt-mixture temperature, similar results were seen for rich mixtures, as well. For the lower temperature, permeation into a rich mixture increased the entropy generation per unit of converted fuel.

The elementary reactions, R8 ($\text{OH} + \text{H} + \text{M} \rightarrow \text{H}_2\text{O} + \text{M}$, net forward), R5 ($\text{H}_2 + \text{M} \rightarrow 2\text{H} + \text{M}$, net reverse) and R3 ($\text{OH} + \text{H}_2 \rightarrow \text{H} + \text{H}_2\text{O}$, net forward) were most important for entropy generation towards quenching. The R5r as recombination reaction had a notable relative increase towards the flame quenching instance. High peaks of entropy generation rate of R8f and R5r observed when the flame reached the wall and quenched.

3.2 2-D side-wall quenching (SWQ) configuration

In the study of the two-dimensional configuration reported in Article 1, the laminar planar flame propagated in a channel against the approaching reactants flow speed. In SWQ, the flame burned parallel to the wall. Note that the flame propagated freely to either upstream or downstream, depending on flame speed relative to the approaching flow in the present setup. The

present study supplements Article 1 to discuss SWQ flame characteristics for an initially lean-fuel case for IW and PW. The latter led to the formation of secondary, non-premixed flame with fuel seeping through the membrane and burning with the excess oxygen from the primary premixed flame. The double-flame arrangement, consisting of a primary premixed flame and a secondary non-premixed flame was only observed in fuel-lean conditions. The stoichiometric and rich mixture conditions did not show the double-flame arrangement, as most of available oxygen was consumed in its side-on quenching sweep of the boundary layer. This caused the additional fuel supplied by PW to accumulate near the wall.

Figure 3.2 shows the flame temperature for $x^* = 0.5$ for lean-fuel conditions. The non-dimensional distances to the wall are given by $x^* = x/L_x$ and $y^* = y/L_y$ respectively. The spatial dimensions in the two-dimensional domain were $L_x = 0.02$ m and $L_y = 0.01$ m for the main flow and wall-normal direction, respectively. The non-dimensional or reduced temperature is defined as $T^* = (T - T_u)/(T_u - T_b)$, where T_b is the burned mixture temperature. The reduced temperature of IW showed that the flame moved towards the outlet because no fuel was injected into the near-wall region. The flame was convected downstream towards the outlet of the domain and blown-off by incoming fresh reactants. PW showed the opposite behaviour of flame propagating upstream of the channel at inflow boundary and reached a temperature higher than the burnt mixture temperature. Figure 3.3 shows total heat release rates for $x^* = 0.5$ at fuel-lean conditions. The peaked magnitudes of the heat release rate at the wall were observed for IW as the flame moved towards the outlet at a different time instants. PW showed a different trend of heat release rate, with decreasing peaked magnitudes at a distance from the wall compared to IW. Both walls in 2-d SWQ setup showed low peak values of quenching heat release rate at the wall, resulting in low quenching wall heat-flux values compared to 1-d HOQ (see Article 1).

It is commonly seen that experimental SWQ setup use planar laser-induced fluorescence for tracking hydroxyl distributions (OH-PLIF) to identify the

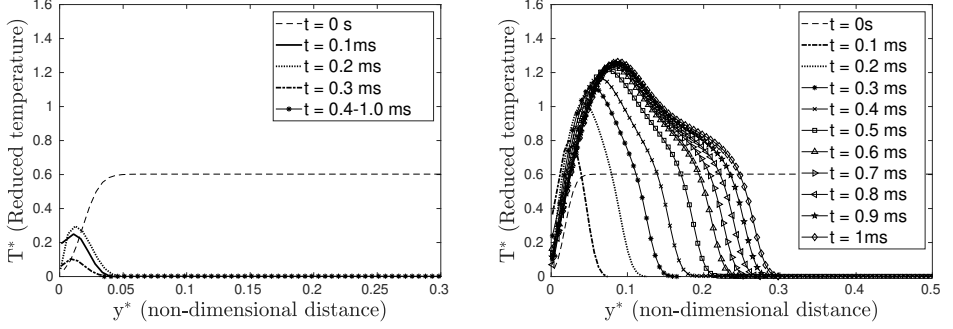


Figure 3.2: Reduced Temperature (T^*) profiles of flame at $x^* = 0.5$ for (a) Impermeable wall (IW) and (b) Permeable wall (PW) with hydrogen flux at lean-fuel conditions ($\phi = 0.5$).

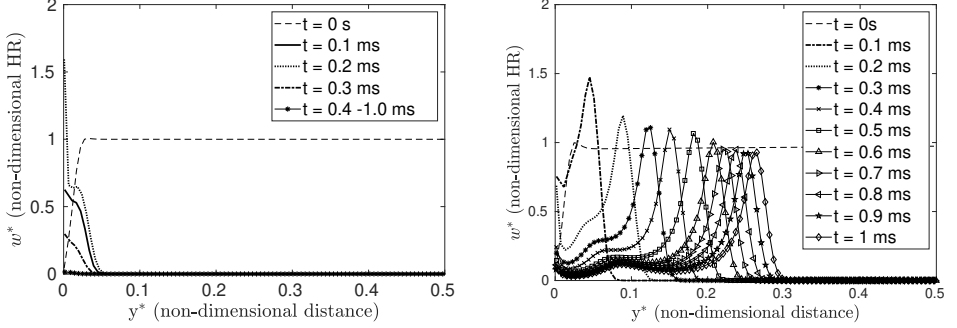


Figure 3.3: Non-dimensional total heat release rate (HR) profiles of flame at $x^* = 0.5$ for (a) Impermeable wall (IW) and (b) Permeable wall (PW) with hydrogen flux at lean-fuel conditions ($\phi = 0.5$). The HR magnitude of initialized flame away from wall is taken for normalization of HR profiles.

flame front location. Flame quenching is expressed as a wall-normal distance, y_{OH}^* , see figure 3.4. It is defined as the flame location where the normalized spatial OH gradient falls or reaches below half of its maximum value. Here, the OH gradient is normalized by the maximum OH gradient of the initialized flame at wall-normal distance. The adopted definition for numerical simulations was taken from laser diagnostics [67, 69], where the OH molecule is used to identify the flame front. The quenching Peclet number is given as $Pe_{OH}^* = y_{OH}^* / \delta_L$ where δ_L is characteristic flame thickness. The definition of δ_L can be found in Articles 2 and 3. The flame speed, S_L

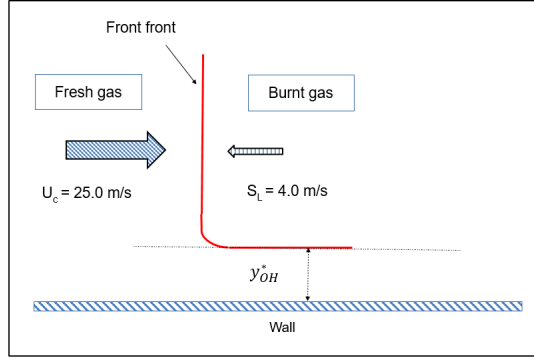


Figure 3.4: 2-d side-wall quenching (SWQ) setup at fuel-lean condition ($\phi = 0.5$). The quenching distance is given as y_{OH}^* , and the Peclet number (Pe_Q) is defined based on OH concentration.

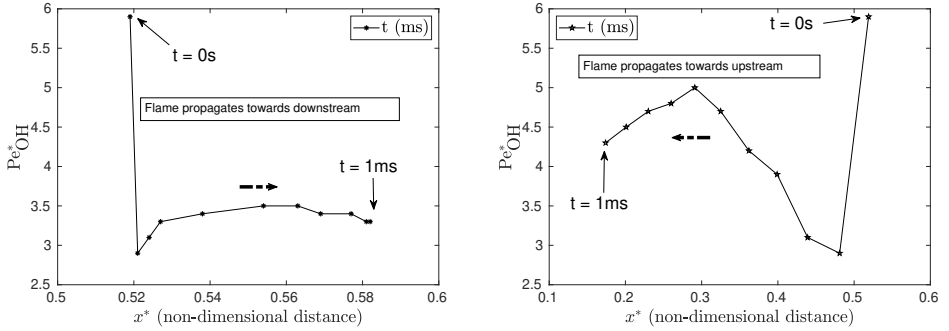


Figure 3.5: Quenching Peclet number (Pe_{OH}^*) at different time instants for (a) Impermeable wall (IW) and (b) Permeable wall (PW) with hydrogen flux at lean-fuel condition ($\phi = 0.5$).

is computed from IW after initialization of the flame at $x^* = 0.5$.

Figure 3.5 shows the different temporal evolutions of the quenching Peclet number (Pe_{OH}^*) after initialization. IW showed that flame quenching occurs much closer to the wall, as flame progress towards the outlet or downstream of the domain and reaches stable Pe_{OH}^* values around 3.2 with blow off or negative flashback velocity at 1.2 m/s. On the other hand, PW showed that flame progressed towards inflow boundary or upstream direction. The flame quenching occurred away from the wall as observed in the varying Pe_{OH}^* trend as time progressed. The hydrogen mass flux was primarily

determined by the difference of partial pressure of hydrogen at the wall and permeate sides. The hydrogen flux by PW led to an increase of the local equivalence ratio in the near-wall region. The premixed mixture changed to a stratified fuel-air mixture and propagated towards the reactants inlet at the left or upstream boundary. This led to a large flashback velocity of 5.44 m/s in the laminar channel flow configuration. The PW or novel fuel diffuser at fuel-lean conditions needs a careful designed turbulent sweep flow in the near-wall region that removes hydrogen fuel to avoid the large impact of boundary layer flashback velocities.

3.3 Discussion

Figure 3.1 outlines the pathways of articles based on flame-wall interaction (FWI) with hydrogen permeable wall boundary implemented in the S3D DNS code. The mass flux of hydrogen across the wall was based on the wall boundary formulation described in Sect. 2.2.2. PW mimics the membrane behavior of the hydrogen flow across the wall and its consumption with lowering of its partial pressure in the combustion process. The PW provides an outline of non-zero scalar, isothermal wall boundary condition that allows a hydrogen gas flow in combustion simulation. The PW membrane related constants were kept constant for all simulations. Articles 1 and 2 are performed for hydrogen-air mixtures. Article 1 was a first attempt to model hydrogen injection through the wall as a porous fuel diffuser to understand near-wall flow physics during flame quenching process. The investigations were carried out for laminar flames subjected to head-on and side-wall configurations at different equivalence ratios. In Article 2, the investigations of the 1-d HOQ configurations were extended with effects of variations in varying wall mass flux i.e permeation pressure difference, stoichiometry, dilution, and unburnt gas and wall temperatures. All studies provided FWI characteristics and influence of the hydrogen flow through the membrane on local wall chemistry and heat transfer. The implications of modeling was that initial lean-fuel mixture conditions with PW resulted in significant in-

crease of wall heat flux and large heat release rate at the wall. On the other hand, rich and stoichiometric conditions gave moderate reduction of wall heat flux due to PW boundary. The quenching instant definition based on heat flux due to PW boundary. The quenching instant definition based on heat release rate and wall heat flux was appropriate for premixed hydrogen based flames. Article 3 extends the study performed for methane-air mixtures with a hydrogen permeable wall boundary. Hydrogen released through PW as a secondary fuel participated and influenced on FWI characteristics. Different FWI characteristics were observed in comparison to hydrogen-air mixtures. The flame quenching instant based on OH gradient was more appropriate than the definition based on maximum reaction heat release rate and minimum flame thickness.

Article 4 is an extension of Articles 1 and 2 with the focus on local entropy production or irreversibilities and entropy fluxes computations near the wall. In transient FWI, chemical reactions and conduction remained important sources of entropy production. The viscous effects remained negligible for all computations.

The 2-d SWQ results of Article 1 are discussed here (Sect. 3.2) related to the FWI characteristics. They showed different results of reduced temperature profiles (see Fig. 3.2), non-dimensional heat release rate profiles (see Fig. 3.3) and higher quenching Peclet (Pe_{OH}^*) in the channel flow compared to the 1-d HOQ configuration, both for IW and PW. In 1-d HOQ, the flame quenching distance occurred close to the PW wall compared to IW at fuel-lean conditions. In the SWQ setup, the flame quenching distance tends to be farther away from the PW wall due to the impact of membrane hydrogen flux compared to the convectional IW at fuel-lean conditions. The temporal Pe_{OH}^* trend seen in Fig. 3.5 clearly shows that IW led to stable Pe_{OH}^* values as the time progressed, indicating flame blow off. In contrast, the different trend of Pe_{OH}^* was observed for PW with the flashback velocity of 5.44 m/s in the near-wall boundary. The Pe_{OH}^* trend in PW was primarily dependent on hydrogen consumption in the near-wall region and the mass flux through the wall.

The novelty of the present thesis is towards the study porous fuel injection

systems or burners with membranes that can provide reactive hydrogen fuel flow across the wall based upon the gas diffusion characteristics of membrane. This study can be interesting to further work on hydrogen-based fuel design activities, both in the industry and research. Also, investigation of transient entropy generation can be performed for PW and convectional impervious wall (IW) boundary to understand irreversibilities during the flame quenching process. The entropy study could assist in design improvements related to near-wall losses or system performance as micro combustion.

Chapter 4

Conclusions and further work

4.1 Summary

Numerical simulations of laminar flame-wall interaction for hydrogen-air and methane-air flames were performed in the high-order numerical S3D DNS code. There was successful implementation of selective species H_2 wall boundary condition for permeable wall (PW), which satisfied well-posedness conditions. The motivation of the present work is the development of eventual future utilization of porous wall boundary surfaces or porous fuel diffuser with a distributed fuel injection of reactive H_2 gas and thereby replacement of traditional fuel nozzles.

The following conclusions can be drawn from the present thesis:

1. The PW or membrane boundary facilitates H_2 fuel supply as additional fuel across the wall, based on the pressure difference between feed and permeate side. It affects near-wall radical reactions characterised by low-activation energies. H_2 permeation influences the wall heat release rate during the quenching process and exhibits different FWI characteristics in comparison to the corresponding IW cases.
2. The hydrogen flux through the wall in PW is affected by the pres-

ence of the propagating flame, that resulting in a strong feedback mechanism between wall surface and flame. This mechanism greatly increases boundary layer flashback velocities at lean fuel conditions in laminar SWQ configurations (see Article 1). The lean 2-d SWQ setup with PW showed reduced heat release rates and temperature profiles compared to the 1-d HOQ setup at quenching as flame propagated parallel to the wall. The temporal evolution of Pe_{OH}^* showed that flame quenching occurs farther away from the wall for PW in comparison to 1-d HOQ at fuel-lean conditions (See Sect 3.2).

3. The presence of PW showed different FWI characteristics for varying (initially) premixed flames in comparison to the corresponding IW cases for HOQ. The findings (see Articles 1 and 2) showed that (initially) fuel-rich and stoichiometric flames result in reduced quenching wall heat flux in comparison to the IW cases. Conversely, an (initially) fuel-lean flame at $\phi_u = 0.5$ showed an increased quenching wall heat flux magnitude by a factor of three in comparison to the IW case.
4. The influence of the wall on the flame is felt much earlier for PW than for the corresponding IW case. The fuel permeation gives a locally richer mixture at the PW, giving more H radicals than O radicals close to the wall, resulting in a notable increase of the recombination reaction $2\text{H} \rightarrow \text{H}_2$ (Reaction R5 reverse) towards flame quenching. A lower initial temperature and diluents (N_2 as inert and H_2O as participating species) reduce the burned mixture temperature and eventually reduce the wall heat flux. With diluents, flame propagation and the quenching instance are delayed (see Article 2).
5. In premixed methane-air flame interaction with PW, flame quenching occur earlier than in the IW case, and with a considerable flame wall distance owing to mutual effects of the large concentration of H_2 , reduced flame temperature and increased convective heat transfer away from the wall and flame. When the flame reaches close to the wall, increased H_2 concentration leads to a reduction of OH accumulation before other species (but O_2) are affected. The conventional flame-

quenching definition, based on maximum wall heat flux as quenching instance, is inappropriate to this study as it fail to capture the cease of major heat release (see Article 3). An alternative flame-quenching definition, based on spatial OH gradient [67] with the maximum OH as flame location, shows the cease of major reactions at quenching. This definition is also in agreement with the IW studies.

6. In the entropy analysis study on FWI for PW, permeating H_2 fuel across wall increase both entropy generation and fuel converted. The effects of fuel permeation remain similar for unburnt temperatures at 300 K, 500 K and 750 K. A lower temperature gives higher entropy generation because conduction has a major share of the total entropy generation. At lean fuel conditions, fuel permeation reduces the entropy generation per unit of fuel converted. The major elementary reactions contributing to entropy generation are R8f, R5r and R3f (see Article 4). Furthermore, as found in previous literature, the chemical reaction component of entropy generation remain a significant contributor, with conduction as the second most important source. Mass diffusion is of modest importance, while viscous forces are negligible, as sources of entropy.

4.2 Future work

FWI results of PW cases of both hydrogen and methane mixtures can represent an optimal starting point to address further with the inclusion of complex flow problems that aid to understanding of the near-wall region. These studies can also aid to model fuel diffuser or permeable wall surface on energy conversion device to improve over fuel diffuser design for reactive fuel H_2 that would improve hardware life. The present studies were based on the assumption that no wall surface catalytic reactions and same temperatures at the wall and initial mixtures ($T_w = T_u$).

The following tasks are possible to explore as further research work:

1. PW boundary modification to allow to have different wall temperature such that $T_w \neq T_u$. These simulations will have thermal boundary layer formation near the wall.
2. Modeling of water condensation effects at wall. As pointed out in [52] that "cold" walls ($T_w < 400$ K) could influence on high heat release rate at the wall. The solving of PW cases with water condensation effects aid to understanding of wall heat fluxes at quenching.
3. Extending to a higher dimension of 3-d case with PW must be verified to an understanding of spatially varying near-wall FWI characteristics in turbulent flame configuration. It is noted that direct numerical simulations of turbulent channel flow bounded by the permeable wall showed significant reduction of skin-friction at the wall, affecting overall flow structures [70]. The paper showed reports of reduction of viscous sublayer thickness and weakened vortical structures near the permeable wall. Such a study is therefore recommended to confirm the wall boundary effects that include spatially varying wall heat fluxes and vorticity structures.

Bibliography

- [1] J. D. Clark, J. W. K. Harris, Fire and its roles in early hominid lifeways, *African Archaeological Review* 3 (1) (1985) 3–27.
- [2] J. A. J. Gowlett, R. W. Wrangham, Earliest fire in africa: towards the convergence of archaeological evidence and the cooking hypothesis, *Azania: Archaeological Research in Africa* 48 (1) (2013) 5–30.
- [3] J. A. J. Gowlett, The discovery of fire by humans: a long and convoluted process, *Philosophical Transactions of the Royal Society B: Biological Sciences* 371 (1696) (2016) 20150164.
- [4] K. S. Brown, C. W. Marean, A. I. R. Herries, Z. Jacobs, C. Tribolo, D. Braun, D. L. Roberts, M. C. Meyer, J. Bernatchez, Fire as an engineering tool of early modern humans, *Science* 325 (5942) (2009) 859–862.
- [5] S. O. Drønen, Humans used fire earlier than previously known, university of bergen news, URL www.uib.no/en/news/101760/early-humans-used-innovative-heating-techniques (accessed : 19 Aug. 2020).
- [6] CO₂ emissions from fuel combustion: Overview (2020), Report, IEA, Paris, URL www.iea.org/reports/co2-emissions-from-fuel-combustion-overview, (accessed: 20 Aug. 2020).
- [7] A. Clerici, G. Alimonti, World energy resources, *EPJ Web of Conferences* 98 (2015) 01001.
- [8] World energy outlook, Technical report, IEA, Paris (2019).

- [9] Energy, Technical report, OECD Green growth studies (2020).
- [10] E. A. Wrigley, Energy and the english industrial revolution, *Philosophical Transactions of the Royal Society A: Mathematical, Physical and Engineering Sciences* 371 (1986) (2013) 20110568.
- [11] H. Ritchie, Energy, Our World in Data (2014)
URL ourworldindata.org/energy, (accessed: 20 Aug. 2020).
- [12] Global energy and CO₂ status report 2019, Technical report, IEA, Paris (2019).
- [13] S. Shafiee, E. Topal, When will fossil fuel reserves be diminished?, *Energy Policy* 37 (1) (2009) 181 – 189.
- [14] H. Ritchie, Fossil fuels, Our World in Data (2017)
URL ourworldindata.org/fossil-fuels, (accessed: 17 Aug. 2020).
- [15] N. Grunewald, I. Martínez-Zarzoso, Did the Kyoto protocol fail? An evaluation of the effect of the Kyoto protocol on CO₂ emissions, *Environment and Development Economics* 21 (2015) 1–22.
- [16] D. V. Masson, P. Zhai, H. O. Pörtner, D. Roberts, J. Skea, P. R. Shukla, A. Pirani, W. M. Okia, C. Péan, R. Pidcock, S. Connors, J. B. R. Matthews, Y. C. X. Zhou, M. I. Gomis, E. Lonnoy, T. Maycock, M. Tignor, T. Waterfield, Summary for policymakers—in: *Global warming of 1.5 C*, IPCC report (2018).
- [17] Aeronautics and air transport: Beyond vision 2020 (towards 2050), Technical report, Advisory Council for Aeronautics Research in Europe (ACARE) (2010).
- [18] D. Cebrucean, V. Cebrucean, I. Ionel, CO₂ capture and storage from fossil fuel power plants, *Energy Procedia* 63 (2014) 18 – 26.
- [19] S. M. Benson, F. M. Orr, Carbon dioxide capture and storage, *Materials Research Society Bulletin* 33 (4) (2008) 303–305.

- [20] S. Chu, Carbon capture and sequestration, *Science* 325 (5948) (2009) 1599–1599.
- [21] N. Holt, G. Booras, D. Todd, Summary of recent IGCC studies of CO₂ capture for sequestration, Gasification Technologies Conference, 12-15 Oct, San Francisco, CA, 2003.
- [22] A policy strategy for carbon capture and storage, Technical report, IEA, Paris (2012), URL www.iea.org/reports/a-policy-strategy-for-carbon-capture-and-storage, (accessed : 15 Aug 2020).
- [23] E. S. Rubin, J. E. Davison, H. J. Herzog, The cost of CO₂ capture and storage, *International Journal of Greenhouse Gas Control* 40 (2015) 378 – 400.
- [24] D. Y. C. Leung, G. Caramanna, M. M. Maroto-Valer, An overview of current status of carbon dioxide capture and storage technologies, *Renewable and Sustainable Energy Reviews* 39 (2014) 426 – 443.
- [25] K. Jordal, Benchmarking of power cycles with CO₂ capture – The impact of the selected framework, *International Journal of Greenhouse gas control* 2 (2008) 468–477.
- [26] S. F. Rice, D. P. Mann, Auto-thermal reforming of natural gas to synthesis gas, Technical Report SAND2007-2331, Sandia National Laboratories (2007).
- [27] R. Bredesen, K. Jordal, O. Bolland, High-temperature membranes in power generation with CO₂ capture, *Chemical Engineering and Processing: Process Intensification* 43 (9) (2004) 1129–1158.
- [28] E. Johannessen, K. Jordal, Study of a H₂ separating membrane reactor for methane steam reforming at conditions relevant for power processes with CO₂ capture, *Energy Conversion and Management* 46 (7-8) (2005) 1059–1071.

- [29] A. S. Augustine, Y. H. Ma, N. K. Kazantzis, High pressure palladium membrane reactor for the high temperature water–gas shift reaction, *International Journal of Hydrogen Energy* 36 (9) (2011) 5350 – 5360.
- [30] R. Cheng, H. Levinsky, Lean premixed burners, in: *Lean Combustion*, 2nd Edition, Academic Press, Boston, 2016, pp. 203 – 229.
- [31] R. W. Grout, A. Gruber, C. S. Yoo, J. H. Chen, Direct numerical simulation of flame stabilization downstream of a traverse fuel jet in cross-flow, *Proceedings of Combustion Institute* 33 (1) (2010) 1629–1637.
- [32] J. Fritz, M. Kröner, T. Sattelmayer, Flashback in a swirl burner with cylindrical premixing zone, *Journal of Engineering for Gas Turbines and Power-Transactions of ASME* 126 (2) (2004) 276 – 283.
- [33] R. W. Grout, A. Gruber, H. Kolla, P. T. Bremer, J. C. Bennett, A. Gyulassy, J. H. Chen, A direct numerical simulation study of turbulence and flame structure in transverse jets analysed in jet-trajectory based coordinates, *Journal of Fluid Mechanics* 706 (2012) 351–383.
- [34] H. Kolla, R. W. Grout, A. Gruber, J. H. Chen, Mechanisms of flame stabilization and blowout in a reacting turbulent hydrogen jet in cross-flow, *Combustion and Flame* 159 (8) (2012) 2755–2766.
- [35] J. D. Gounder, P. Kutne, A. Gruber, Experimental investigation of a bluff body burner for distributed hydrogen injection, *ASME Turbo Expo 2017: Turbomachinery Technical Conference and Exposition*, Charlotte, NC, June 26-30, 2017, Paper No. GT2017-63414.
- [36] J. H. Chen, A. Choudhary, B. de Supinski, M. DeVries, E. R. Hawkes, S. Klasky, W. K. Liao, K. L. Ma, J. Mellor-Crummey, N. Podhorszki, R. Sankaran, S. Shende, C. S. Yoo, Tera-scale direct numerical simulations of turbulent combustion using S3D, *Computational Science Discovery* 2 (1) (2009) 015001.
- [37] E. Hawkes, R. Sankaran, J. Sutherland, J. Chen, Scalar mixing in direct numerical simulations of temporally evolving plane jet flames with

- skeletal CO/H₂ kinetics, *Proceedings of the Combustion Institute* 31 (2007) 1633–1640.
- [38] A. Gruber, R. Sankaran, E. R. Hawkes, J. H. Chen, Turbulent flame – wall interaction: a direct numerical simulation study, *Journal of Fluid Mechanics* 658 (2010) 5–32.
 - [39] A. Gruber, J. H. Chen, D. Valiev, C. K. Law, Direct numerical simulation of premixed flame boundary layer flashback in turbulent channel flow, *Journal of Fluid Mechanics* 709 (2012) 516–542.
 - [40] R. Sankaran, E. R. Hawkes, J. H. Chen, T. Lu, C. K. Law, Structure of a spatially developing turbulent lean methane-air Bunsen flame, *Proceedings of the Combustion Institute* 31 I (1) (2007) 1291–1298.
 - [41] J. H. Chen, Petascale direct numerical simulation of turbulent combustion - fundamental insights towards predictive models, *Proceedings of the Combustion Institute* 33 (1) (2011) 99–123.
 - [42] E. R. Hawkes, J. H. Chen, Direct numerical simulation of hydrogen-enriched lean premixed methane-air flames, *Combustion and Flame* 138 (3) (2004) 242–258.
 - [43] T. Echekki, J. H. Chen, Direct numerical simulation of autoignition in non-homogeneous hydrogen-air mixtures, *Combustion and Flame* 134 (3) (2003) 169–191.
 - [44] R. Sankaran, H. G. Im, E. R. Hawkes, J. H. Chen, The effects of non-uniform temperature distribution on the ignition of a lean homogeneous hydrogen-air mixture, *Proceedings of the Combustion Institute* 30 (1) (2005) 875–882.
 - [45] J. Chen, R. Sankaran, E. Hawkes, J. Sutherland, D. Skinner, 2005 Joule software effectiveness study of S3D applied to the INCITE goal, URL www.researchgate.net/publication/267547950_2005_Joule_Software_Effectiveness_Study_of_S3D_Applied_to_the_INCITE_Goal_Executive_Summary (2005) (accessed:15 Aug. 2020).

- [46] R. W. Grout, S3D direct numerical simulation: Preparation for the 10–100 PF era, URL www.osti.gov/servlets/purl/1599760 (2012) (accessed: 17 Aug. 2020).
- [47] C. A. Kennedy, M. H. Carpenter, R. M. Lewis, Low-storage, explicit Runge-Kutta schemes for the compressible Navier-Stokes equations, *Applied Numerical Mathematics* 35 (3) (2000) 177–219.
- [48] R. J. Kee, L. G. Dixon, J. Warnatz, M. E. Coltrin, J. A. Miller, H. K. Moffat, A fortran chemical kinetics package for the analysis of gas-phase chemical kinetics., Technical report, Release 3.5, Reaction Design Inc., San Diego, CA (1999).
- [49] C. A. Kennedy, M. H. Carpenter, Several new numerical methods for compressible shear layer simulations, *Applied Numerical Mathematics* 14 (804) (1994) 397.
- [50] G. Bruneaux, K. Akselvoll, T. Poinso, J. H. Ferziger, Flame-wall interaction simulation in a turbulent channel flow, *Combustion and Flame* 107 (1–2) (1996) 27–44.
- [51] T. M. Alshaalan, C. J. Rutland, Turbulence, scalar transport, and reaction rates in flame-wall interaction, *Proceedings of the Combustion Institute* 27 (1) (1998) 793–799.
- [52] O. Ezekoye, Heat transfer consequences of condensation during premixed flame quenching, *Combustion and Flame* 112 (1) (1998) 266 – 269.
- [53] X. Jiang, C. H. Lai, Numerical Techniques for Direct and Large-Eddy Simulations, Chapman & Hall/CRC Numerical Analysis and Scientific Computing Series, CRC Press, 2009.
- [54] B. Gustafsson, A. Sundstrom, Incompletely parabolic problems in fluid dynamics, *SIAM Journal on Applied Mathematics*. 35 (2) (1978) 343–357.

- [55] J. C. Strikwerda, Initial boundary value problems for incompletely parabolic systems, *Communications on Pure and Applied Mathematics* 30 (6) (1977) 797–822.
- [56] J. Nordström, M. Svärd, Well-posed boundary conditions for the navier–stokes equations, *SIAM Journal on Mathematical Analysis* 43 (3) (2005) 1231–1255.
- [57] K. W. Thompson, Time dependent boundary conditions for hyperbolic systems, *Journal of Computational Physics* 68 (1) (1987) 1–24.
- [58] K. W. Thompson, Time-dependent boundary conditions for hyperbolic systems, II, *Journal of Computational Physics* 89 (2) (1990) 439–461.
- [59] C. Yoo, Y. Wang, A. Trouve, H. Im, Characteristic boundary conditions for direct simulations of reacting counter flow, *Combustion Theory and Modelling* 9 (1) (2005) 617–646.
- [60] C. S. Yoo, H. G. Im, Characteristic boundary conditions for simulations of compressible reacting flows with multi-dimensional, viscous and reaction effects, *Combustion Theory and Modelling* 11 (2) (2007) 259–286.
- [61] J. A. Ekaterinaris, High-order accurate, low numerical diffusion methods for aerodynamics, *Progress in Aerospace Sciences* 41 (3-4) (2005) 192–300.
- [62] S. K. Lele, Compact finite difference schemes with spectral-like resolution, *Journal of Computational Physics* 103 (1) (1992) 16–42.
- [63] A. Gruber, Direct numerical simulation of turbulent combustion near solid surfaces, Ph.D. thesis, Norwegian University of Science and Technology, Trondheim, Norway (2006).
- [64] J. Li, Z. Zhao, A. Kazakov, F. L. Dryer, An updated comprehensive kinetic model for hydrogen combustion, *International Journal of Chemical Kinetics* 36 (10) (2004) 566–575.

- [65] M. D. Smooke, V. Giovangigli, Formulation of the premixed and non-premixed test problems, in: *Reduced Kinetic Mechanisms and Asymptotic Approximations for Methane-Air Flames*, Vol. 384 of *Lecture Notes in Physics*, Berlin Springer Verlag, 1991, p. 1.
- [66] A. Kazakov, M. Frenklach, Reduced reaction sets based on gri-mech 1.2, URL www.combustion.berkeley.edu/drm (1994) (accessed 14 Nov. 2020).
- [67] C. Jainski, M. Reißmann, B. Böhm, J. Janicka, A. Dreizler, Sidewall quenching of atmospheric laminar premixed flames studied by laser-based diagnostics, *Combustion and Flame* 183 (2017) 271 – 282.
- [68] Z. Li, S. Chou, C. Shu, W. Yang, Entropy generation during micro-combustion, *Journal of Applied Physics* 97 (8) (2005) 084914.
- [69] C. Jainski, M. Reißmann, B. Böhm, A. Dreizler, Experimental investigation of flame surface density and mean reaction rate during flame–wall interaction, *Proceedings of the Combustion Institute* 36 (2) (2017) 1827–1834.
- [70] S. Hahn, J. E. Jongdoo, H. Choi, Direct numerical simulation of turbulent channel flow with permeable walls, *Journal of Fluid Mechanics* 450 (2002) 259–285.
- [71] G. P. Smith, D. M. Golden, M. Frenklach, B. Eiteener, M. Goldenberg, C. T. Bowman, R. K. Hanson, S. Song, W. C. Gardiner, V. V. Lissianski, Z. Qin, GRI-Mech 3.0, URL www.combustion.berkeley.edu/gri_mech (accessed 15 Nov. 2020).
- [72] S. Ganter, A. Heinrich, T. Meier, G. Kuenne, C. Jainski, M. C. Reißmann, A. Dreizler, J. Janicka, Numerical analysis of laminar methane–air side-wall-quenching, *Combustion and Flame* 186 (2017) 299 – 310.

Appendices

A Selected Papers

Article 1

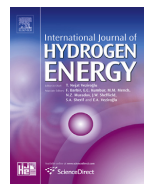
Direct numerical simulation of laminar flame-wall interaction for a novel H₂-selective membrane/injector configuration

Andrea Gruber, Prashant S. Salimath, Jacqueline H. Chen

Published in International Journal of Hydrogen Energy

Available online at www.sciencedirect.com

ScienceDirect

journal homepage: www.elsevier.com/locate/ije

Direct numerical simulation of laminar flame–wall interaction for a novel H₂-selective membrane/injector configuration

Andrea Gruber^{a,*}, Prashant S. Salimath^b, Jacqueline H. Chen^c

^a SINTEF Energy Research, Dept. of Thermal Energy, K. Heiesvei 1A, 7465 Trondheim, Norway

^b Norwegian University of Science and Technology, Dept. of Energy and Process Engineering, Trondheim, Norway

^c Combustion Research Facility, Sandia National Laboratories, Livermore, CA 94550, USA

ARTICLE INFO

Article history:

Received 7 November 2013

Received in revised form

10 January 2014

Accepted 13 January 2014

Available online 26 February 2014

Keywords:

Pre-combustion CCS

Hydrogen transport membrane

Flame–wall interaction

Head-on quenching

ABSTRACT

Direct numerical simulations are performed to investigate the transient processes of laminar flame–wall interaction and quenching near a porous, permeable wall and compared against a reference case of a non-porous impermeable wall. A boundary condition formulation that models species (hydrogen in this case) transport through a permeable wall, driven by the fuel species partial pressure difference between the feed and the permeate side of a selective membrane, has been implemented in a high-order finite difference direct numerical simulation code for reactive flows (S3D) by Chen et al. (2009) [1]. The present results are obtained for lean, stoichiometric and rich initial mixture conditions on the permeate side of the permeable wall and indicate that the characteristic parameters of the flame–wall interaction (wall heat flux, quenching distance) are affected to a large extent by the presence of the membrane hydrogen flux. Concurrently, the hydrogen flux through the membrane is also strongly affected by the presence of the flame during the transient flame–wall interaction process, finally resulting in a strong feedback mechanism between the membrane hydrogen flux and the flame that greatly increases boundary layer flashback speeds at fuel lean conditions.

Copyright © 2014, Hydrogen Energy Publications, LLC. Published by Elsevier Ltd. All rights reserved.

Introduction

Large scale implementation of CO₂ Capture and Storage (CCS) technologies is largely unrealized presently due to its high cost, e.g. two to four times the present European trading cost on CO₂ emissions [2]. Considering the pre-combustion CCS option from stationary gas turbine power generation, a significant part of the energy and efficiency penalty, i.e. the added cost, is related to the reforming and separation of

hydrogen from fossil fuels [3]. Presently proposed technology concepts use Auto-Thermal Reforming (ATR) or Steam Methane Reforming (SMR) with Water Gas Shift (WGS) reactors to produce the H₂-rich syngas from natural gas, while CO₂ is separated from the syngas by adsorption [4]. One potentially more efficient alternative is to introduce a hydrogen transport membrane (HTM) where the reforming, the water gas shift and the hydrogen separation from the carbon dioxide are combined in the same unit [5]. For stationary power generation from coal using Integrated

* Corresponding author. Tel.: +47 73593699; fax: +47 73592889.

E-mail address: andrea.gruber@sintef.no (A. Gruber).

0360-3199/\$ – see front matter Copyright © 2014, Hydrogen Energy Publications, LLC. Published by Elsevier Ltd. All rights reserved.
<http://dx.doi.org/10.1016/j.ijhydene.2014.01.148>

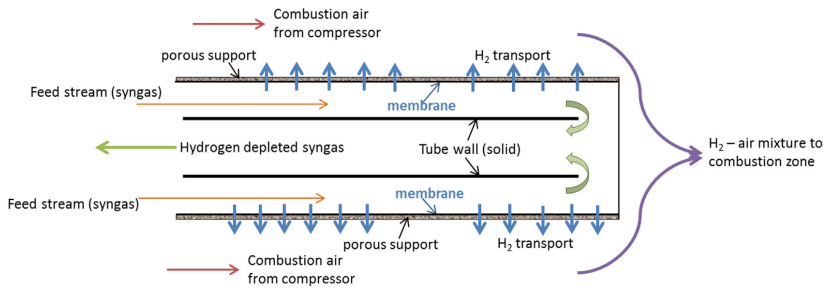


Fig. 1 – Sketch of the fuel injector with in-situ hydrogen separation (from syngas).

Gasification Combined Cycle (IGCC), HTMs may replace the WGS and the CO₂ separation unit [6,7]. Once the hydrogen fuel has been obtained and it is ready for the gas turbine, an additional efficiency penalty cost is due to the preparation (separation and compression) of the inert diluent, i.e. nitrogen, that is needed to lower the reactivity of hydrogen as it flows out of the injection nozzles and mixes with the relatively hot compressor air. The diluent is required to contain NO_x formation in the case of a non-premixed burner or to ensure intrinsic flashback safety in the case of a premixed burner (see below).

Optimal fuel injection in lean pre-mixed (LPM) burners for state-of-the-art gas turbines is achieved when the following conditions are simultaneously satisfied:

1. The fuel species are uniformly mixed with the oxidant species to the target equivalence ratio and no fuel-rich fluid pockets are present.
2. Point 1 above is achieved very quickly and within a short distance downstream of the fuel injector nozzle.
3. Little or no fuel is allowed (to remain) in the wall boundary layer implying that the newly prepared burnable mixture must be carried away from the burner walls.
4. The pressure loss related to fuel injection is minimized.
5. The fuel injection configuration does not create flow regions, in the fuel nozzle near field, that are simultaneously characterized by low fluid velocity and fuel-rich stoichiometry.

Conventional gaseous fuel injection nozzles, often designed for injection of natural gas, commonly operate in transverse jets configurations (jet-in-cross-flow) in which the fuel stream exits a circular nozzle and enters the approaching oxidant stream at an angle that is approximately normal to its direction. This fuel injection strategy rarely has difficulties complying with points 1), 2), 3) and, to some extent, also point 4) above, ensuring good fuel penetration into the oxidant stream and fast mixing. However, it fails with respect to point 5) due to the intrinsic characteristics of the transverse-jet flow field [8].

Many of the technical challenges that emerge when attempting to utilize highly reactive fuels, such as hydrogen, in LPM gas turbine burners originally designed to operate using less reactive fuels, as natural gas, are often related to

- Avoiding flashback of the flame from its design stabilization position into the premixer section of the burner either along the wall boundary layer or through the duct centerline due to aerodynamic effects [9].
- Avoiding stable flame anchoring, once flashback has actually occurred, in the immediate vicinity of fuel injection nozzles due to the presence of concentrated point sources of the highly reactive fuel and, locally, of fuel-rich conditions, co-located with fluid velocity fields that facilitates flame anchoring [10,11].

The long-term, ultimate goal of the present work is to aid the development of a novel burner concept for stationary, multi-fueled gas-turbine engines that operate in LPM mode. In this new burner concept a porous fuel diffuser, possibly coated with a H₂-selective membrane, would replace traditional fuel nozzle-holes as for the hydrogen injection, thereby avoiding the presence of concentrated point sources of this highly reactive fuel, while conventional nozzles would still be used, within the same burner, for traditional or back-up fuels such as natural gas or fuel oil. Describing the constructive details of the actual diffuser is outside the scope of the present paper but it can be mentioned here that a device made of porous ceramic or steel is envisioned, either with or without the presence of the selective membrane layer, depending on the requirement (or lack thereof) for in-situ hydrogen separation. This new burner concept, utilizing opportunely shaped porous steel or ceramic diffusers as “distributed” injectors for the highly reactive hydrogen fuel, would avoid the presence of concentrated fuel point sources and thereby address the latter of the two issues mentioned above. There may be other potential efficiency gains from the point of view of the overall process, most notably making the diluent (nitrogen) unnecessary.

The major limitation of this unconventional fuel injection configuration lies in the relatively low hydrogen fluxes presently allowed by H₂-selective membranes and in the potentially high pressure drop required. While advances in membrane technology may improve the state-of-the-art in the near future, a careful optimization of the flow fields on both the feed and permeate side of the membrane/support pair is needed to achieve high hydrogen fluxes. Maximization of the hydrogen mass flow rate through the membrane

injector device can be achieved by maintaining a large hydrogen partial pressure difference across the membrane and this is usually achieved by introducing a sweep gas that lowers the partial pressure of hydrogen on the permeate side. For the case of hydrogen injection in the premixer section of a gas turbine burner, the sweep gas is the oxidant (primary air), that is a reactant. Therefore, great care must be taken in designing the primary air flow such that its interaction with the permeable wall surface must quickly remove hydrogen fuel from the near-wall region before combustion can occur there. Moreover, it must effectively dilute it in order to rapidly achieve the target (fuel lean) equivalence ratio, see Fig. 1.

In the present paper, as a first preliminary step in the development of this new fuel injector, we investigate laminar flame–wall interaction and quenching for one dimensional and two dimensional configurations where the permeable wall surface consists of a porous support material coated with a H_2 -selective membrane. We compare these results with the more conventional case of flame–wall interaction and quenching on a non-porous impermeable wall. The aim of this study is to provide detailed insight into the flame propagation and quenching behavior in the immediate vicinity of a permeable wall where, unlike the conventional wall–quenching situation, the wall itself provides fuel to the combustion process. We perform direct numerical simulations of head-on quenching (HOQ) and side-on quenching (SOQ) configurations, as described in [12], comparing the flame propagation and quenching behavior at a traditional solid wall versus a notional permeable (H_2 -selective membrane) wall for initially fuel-lean, stoichiometric and fuel-rich equivalence ratios.

Previous work on flame–wall interaction

A number of studies of flame–wall interaction (FWI) configurations exist in the literature [12–18] but none of these have considered a wall permeable to a reactant species. In general, the FWI process can be conveniently described by two quenching parameters, the quenching Peclet number, $Pe_q = x_q/\delta_q$ and the quenching wall heat flux $F_{w,q} = \phi_{w,q}/P_q$. Typically, in these non-dimensional quenching parameters, the dimensional quenching distance x_q and quenching wall heat flux $\phi_{w,q}$ are non-dimensionalized, respectively, by the flame thickness at quenching δ_q , and by the flame power $P_q = \rho_u S_l c_{p,mix}(T_b - T_u)$, where ρ is the fluid density, T its temperature, S_l the laminar flame speed, $c_{p,mix}$ the mixture heat capacity at constant pressure and the subscripts u and b indicate unburnt and burnt conditions. Pe_q is typically reported to be in the range of 3.0 for methane (and similar hydrocarbons) while $F_{w,q} \sim 0.3$. For hydrogen–air flames these figures vary considerably and $Pe_q \sim 1.7$ while $F_{w,q} \sim 0.13$ [18,19]. Most importantly, all of these studies concur that radical recombination at the wall, characterized by low activation energy reactions, plays a very important role in the FWI process [19] and that single-step chemistry, lacking detailed information about radical recombination reactions, fails to predict the FWI process correctly. Multi-dimensional direct simulations of FWI configurations are computationally expensive and therefore only a few of these investigations have been reported in the literature. Moreover, because of their high cost (and in spite of the conclusions reached in the

one dimensional studies mentioned above), most of the reported multi-dimensional direct simulation of FWI configurations have either been restricted to a thermal-diffusive limit in which the effect of thermal expansion on the fluid flow is assumed to be negligible, or to a simple one-step chemical kinetics model and small physical domains. A pioneering paper by [20] reports a two dimensional numerical simulation of laminar flame flashback in a side-wall quenching (SWQ) configuration and suggests that a pressure-based interaction between the premixed flame and the boundary layer flow is the reason behind a larger computed laminar flame speed in the two dimensional configuration compared to the one dimensional case. Subsequent studies by [21–23] on the boundary layer flashback of laminar two dimensional flames added more realistic features to the model, such as effects of the fuel species Lewis number, but are still limited to one-step chemical kinetics. A DNS of HOQ in a two dimensional, pseudo-turbulent reactive boundary layer was conducted by [24] while [25] studied three dimensional HOQ of a back-to-back, premixed flame propagating in constant-density turbulent channel flow. Again, this was performed in the thermal-diffusive limit in which there is no coupling between the flame and the flow field. The SWQ configuration for a three dimensional, v-shaped, premixed flame anchored in weakly turbulent Couette flow was investigated by [26,27] and, while these numerical experiments have provided very useful statistical information, they still lack the detailed chemical kinetics modelling to account for the important effects of radical recombination reactions in the immediate vicinity of the wall. Detailed chemical kinetics was included in [19] for the case of a v-shaped, premixed flame anchored in a fully developed turbulent channel flow revealing interesting insight into the characteristics of the unsteady heat release at the wall and wall heat flux spatial and temporal patterns. While the number of FWI studies for hydrogen or hydrogen-rich fuels is rather limited in the open literature, FWI configurations in which the wall surface is permeable and is supplying fuel to the quenching zone are completely absent.

The remainder of this paper is organized as follows: the governing equations and the problem formulation are presented in Section 2 together with the numerical method of the DNS code, S3D, used to perform the present simulations. Results from DNS are presented in Section 3. Finally, conclusions and recommendations for further work are presented in Section 4.

DNS code, mathematical formulation and case configuration

The S3D code is a massively parallel three dimensional DNS code developed at SANDIA National Laboratories [1] that uses the Message Passing Interface (MPI) for interprocess communication in parallel execution. The code solves the Navier–Stokes equations for a compressible fluid in conservative form on a structured, Cartesian mesh in one, two or three spatial directions. The momentum and continuity equations are solved along with the equations for species and energy transport coupled with a detailed description of the chemical kinetics. The equations solved and the constitutive

Table 1 – The complete 9-species, 19-reactions hydrogen–air chemical kinetics mechanism from [30].

n	Reaction	B	a	E _a
1	O ₂ + H ⇌ OH + O	3.547 × 10 ¹⁵	−0.406	1.6599 × 10 ⁴
2	H ₂ + O ⇌ OH + H	0.508 × 10 ⁵	2.67	0.629 × 10 ⁴
3	OH + H ₂ ⇌ H + H ₂ O	0.216 × 10 ⁹	1.51	0.343 × 10 ⁴
4	H ₂ O + O ⇌ 2OH	2.97 × 10 ⁶	2.02	1.34 × 10 ⁴
5	H ₂ + M ⇌ 2H + M	4.577 × 10 ¹⁹	−1.40	1.0438 × 10 ⁵
6	2O + M ⇌ O ₂ + M	6.165 × 10 ¹⁵	−0.50	0.0
7	H + O + M ⇌ OH + M	4.714 × 10 ¹⁸	−1.00	0.0
8	OH + H + M ⇌ H ₂ O + M	3.800 × 10 ²²	−2.00	0.0
9	O ₂ + H (+M) ⇌ HO ₂ (+M)	1.475 × 10 ¹²	0.60	0.0
10	H + HO ₂ ⇌ O ₂ + H ₂	1.66 × 10 ¹³	0.00	0.823 × 10 ³
11	H + HO ₂ ⇌ 2OH	7.079 × 10 ¹³	0.00	2.95 × 10 ²
12	O + HO ₂ ⇌ OH + O ₂	0.325 × 10 ¹⁴	0.00	0.0
13	OH + HO ₂ ⇌ O ₂ + H ₂ O	2.890 × 10 ¹³	0.00	−4.970 × 10 ²
14	2HO ₂ ⇌ O ₂ + H ₂ O ₂	4.200 × 10 ¹⁴	0.00	1.1982 × 10 ⁴
15	H ₂ O ₂ (+M) ⇌ 2OH (+M)	2.951 × 10 ¹⁴	0.00	4.843 × 10 ⁴
16	H + H ₂ O ₂ ⇌ OH + H ₂ O	0.241 × 10 ¹⁴	0.00	0.397 × 10 ⁴
17	H + H ₂ O ₂ ⇌ H ₂ + HO ₂	0.482 × 10 ¹⁴	0.00	0.795 × 10 ⁴
18	O + H ₂ O ₂ ⇌ HO ₂ + OH	9.550 × 10 ⁶	2.00	3.970 × 10 ³
19	OH + H ₂ O ₂ ⇌ H ₂ O + HO ₂	5.800 × 10 ¹⁴	0.00	9.557 × 10 ³

relationships (the ideal equation of state, models for reaction rates, molecular transport and thermodynamic properties) are described in detailed in Chen et al. [1] and will not be presented here. S3D uses a high-order, non-dissipative numerical scheme, which is an eighth-order central differencing scheme in space (third-order at the boundaries) and a six-stage fourth-order Runge-Kutta method in time. A tenth-order purely dissipative spatial filter is employed in order to remove any spurious high-frequency noise in the simulations [28,29]. The CHEMKIN software distribution and relative libraries are linked to the S3D code to enable detailed evaluation of thermodynamic properties, mixture-averaged transport properties and reaction rates. The homogeneous chemical reactions in the gaseous phase are described by a detailed chemical kinetics mechanism for hydrogen combustion in air [30] that is reported in Table 1 while heterogeneous reactions that may take place in the solid material are not considered here. Thermal diffusion effects, i.e. the Soret effect, have been included in the simulations. Characteristic boundary conditions (NSCBC) are used to describe non-reflective (in terms of pressure waves) open boundaries [31] and the boundary conditions treatment for wall boundaries is described below. No attempt is made to incorporate the effects of radiative heat transfer into this discussion. The S3D code has been used for a range of studies including premixed flames [19,32–35], non-premixed flames [10,11,8,36], and autoignition [37,38].

Wall boundary conditions

Following [39–41] Table 2 lists the correct number of boundary conditions which must be specified to ensure well-posedness for the Euler and Navier–Stokes equations of a reacting gas mixture.

In this table, N_{dim} is the number of dimensions and N_g is the total number of species Y_i included in the model. Note that only $(N_g - 1)$ species equations need be considered because one species equation is redundant in the presence of the continuity equation. Euler slip-walls placed within a Navier–Stokes solver are not considered in this paper.

Boundary conditions for the Navier–Stokes equations applied to a compressible gas mixture at an inert, isothermal, non-porous (impermeable), no-slip wall involve $N_{\text{dim}} + 1 + (N_g - 1)$ equations. One may write these as:

$$\mathbf{u} = 0, \quad T_w = T_u, \quad \left(\frac{\partial Y_i}{\partial x} \right)_w = 0, \quad i = 1, 2, \dots, N_g \quad (1)$$

where \mathbf{u} is the velocity vector and the wall temperature, T_w , is set to be equal to the unburnt reactants temperature, T_u . The immediate consequences of the above equations are that:

$$\frac{\partial \mathbf{u}}{\partial t} = \frac{D\mathbf{u}}{Dt} = 0, \quad \left(\frac{\partial p}{\partial x} \right)_w = \frac{\partial \tau}{\partial x}, \quad (2)$$

where p is the pressure, τ is the stress tensor and x is the wall-normal direction. Note that these equations are not independent boundary conditions but mere consequences of Eq. (1) when applied to the momentum equation (in the absence of body forces). The expression for the pressure gradient at the wall can be inverted (numerically) to extract the value of pressure at the wall, p_w . In the same manner, the impermeability conditions in Eq. (1) give the species mass fractions at the wall and these, together with the temperature, T_w , and pressure, p_w , can be used to compute the fluid density at the wall node, ρ_w , from the equation of state. The formulation summarized here for the wall boundary conditions has been widely used in the past to perform three dimensional DNS

Table 2 – Number of boundary conditions required for well-posedness for the Euler and Navier–Stokes equations.

	Euler	Navier–Stokes
Supersonic inflow	$N_{\text{dim}} + 2 + (N_g - 1)$	$N_{\text{dim}} + 2 + (N_g - 1)$
Sonic inflow	$N_{\text{dim}} + 1 + (N_g - 1)$	$N_{\text{dim}} + 2 + (N_g - 1)$
Subsonic inflow	$N_{\text{dim}} + 1 + (N_g - 1)$	$N_{\text{dim}} + 2 + (N_g - 1)$
No flow	1	$N_{\text{dim}} + 1 + (N_g - 1)$
Subsonic outflow	1	$N_{\text{dim}} + 1 + (N_g - 1)$
Sonic outflow	0	$N_{\text{dim}} + 1 + (N_g - 1)$
Supersonic outflow	0	$N_{\text{dim}} + 1 + (N_g - 1)$

with the S3D code for the case of wall-bounded domains [19,32,8,10,11].

In the present work, 1-D and 2-D direct numerical simulations are also performed to investigate premixed laminar hydrogen–air flame propagation and quenching on porous (permeable) walls that are coated with a H_2 -selective membrane. These permeable walls are still assumed to be isothermal and characterized by the temperature of the unburnt reactants but they allow a flux of hydrogen molecules to pass through them and the boundary conditions formulation described above is changed accordingly. The hydrogen flux through the membrane, indicated here as F_{H_2} ($kg\ m^{-2}\ s^{-1}$), is modelled by the following expression:

$$F_{H_2} = W_{H_2} \frac{Q}{\Delta_m} \left((p_{H_2}^f)^n - (p_{H_2}^p)^n \right) \quad (3)$$

where Q/Δ_m is the membrane permeance and is set to $7.0 \cdot 10^{-6} (kmol\ m^{-2}\ s^{-1}\ Pa^{-0.5})$ in all simulations, W_{H_2} is the molecular weight of hydrogen, and $p_{H_2}^f$ (Pa) is the hydrogen partial pressure where the superscripts f and p indicate the feed and permeate sides respectively (see e.g. [42]). The permeance and pressure exponent used here are typical for Pd-based membranes of 2–3 μm thickness [43,44]. The hydrogen flow rate is controlled by its partial pressure difference across the membrane and the hydrogen partial pressure on the feed side is assumed to have a constant value of $p_{H_2}^f = 10^6$ (Pa) in all simulations. Therefore, the hydrogen flow rate from the feed to the permeate side will vary with the mole fraction of hydrogen in the immediate vicinity of the wall on the permeate side. The mass fraction gradient at the wall is given by the re-arranged Fick's law in the present formulation:

$$\left(\frac{\partial Y_i}{\partial x} \right)_w = - \frac{F_i}{\rho_w D_{mix,w}}, \quad (4)$$

where F_i is the wall flux of species i , $D_{mix,w}$ is the mixture-averaged mass diffusivity and ρ_w is the density of the near-wall fluid. Note that the only flux, F_i , that has a nonzero value is the one for the hydrogen species as given by Eq. (3) and that the impermeability conditions in Eq. (1) still apply for all other species. The species mass fractions at the wall node (on the permeate side) may then be extracted by inverting the numerical stencil for the mass fraction gradients as mentioned above. The updated value for the pressure at the wall, p_w , is obtained by re-arranging the momentum equation that now includes some additional terms due to the species flux:

$$\left(\frac{\partial p}{\partial x} \right)_w = - \sum_{i=1}^{N_g} \frac{\partial F_i}{\partial t} - \frac{\partial u_1}{\partial x} \sum_{i=1}^{N_g} F_i + \frac{\partial \tau}{\partial x}, \quad (5)$$

where u_1 is the wall-normal velocity component (estimated as $u_1 \sim F_{H_2}/\rho_{H_2}$), and the sums are taken over all gases N_g participating (again, in this particular case only hydrogen). The first and second terms on the right hand side of Eq. (5) represent the unsteady and the steady contributions to the wall-normal momentum of the membrane hydrogen flux. Finally, once the new values of Y_i and p_w are known, the value of the density at the wall, ρ_w , can be updated using the equation of state.

One dimensional flame–wall interaction setup

In this configuration a planar laminar flame propagates toward the wall at a normal angle with the solid surface (HOQ configuration) as shown in Fig. 2(a). The simulated one dimensional domains are all characterized by the same spatial dimension extending for $L_x = 0.02$ (m) in the wall-normal direction and are discretized on a mesh consisting of 4096 nodes with a spatial resolution of $\Delta x = 4.9$ (μm). Although a sensitivity study conducted for the fuel-rich case has shown that a resolution of $\Delta x = 9.8$ (μm) would have been sufficient to fully resolve the flame (no noticeable differences were observed in the results when only 2048 nodes were used), we have chosen to perform all 1-D calculations using 4096 nodes in view of future work on similar flames at pressurized conditions. CHEMKIN PREMIX solutions for a freely propagating H_2 –air flame are used to initialize the initial field by placing the flame in the middle of the DNS one dimensional domain. The initial flow field is quiescent. The initial temperature and mixture conditions for the unburnt reactants are $T_u = 750$ (K) and characterized by fuel-lean, stoichiometric or fuel-rich equivalence ratios, $\phi = 0.5, 1.0, 1.5$, respectively. An open, acoustically non-reflecting boundary is placed on the right end of the domain at $x = 0.02$ (m) while an acoustically perfectly reflecting wall boundary, that can either allow a hydrogen flux or not, is placed on the left end of it.

Two dimensional flame–wall interaction setup

In the two dimensional configuration considered here an initially planar, laminar flame propagates in a notional

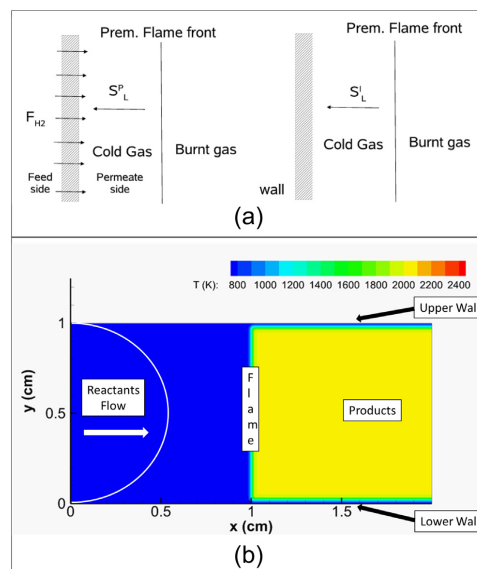


Fig. 2 – Sketch of the 1-D (top) and 2-D (bottom) configurations for the DNS.

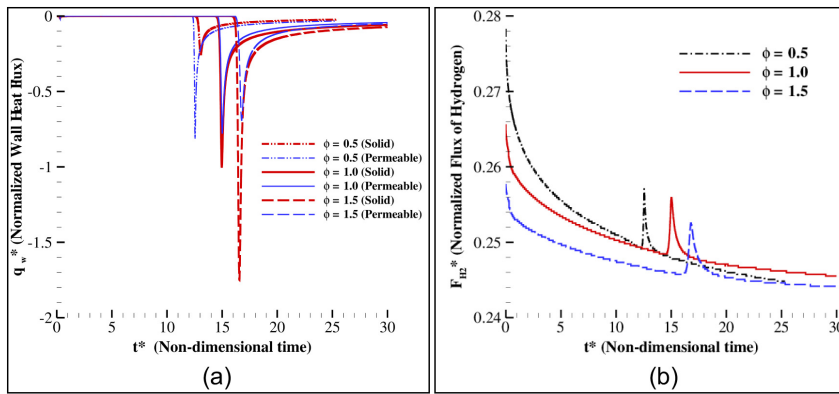


Fig. 3 – Time evolution of the normalized wall heat flux (a) and of the normalized hydrogen mass flux through the membrane (b).

constant-width channel against the laminar flow of the approaching reactants as illustrated in Fig. 2(b). Note that the flame is free to propagate, either upstream or downstream (depending on the value of its own speed relative to the approaching flow), in a direction that is parallel to the walls (SWQ configuration). The two dimensional domains considered here are all characterized by the same spatial dimensions and extend for $L_x = 0.02(\text{m})$ in the main flow direction and $L_y = 0.01(\text{m})$ in the wall-normal direction. The domain is discretized on a mesh consisting of 2048×1024 nodes resulting in a spatial resolution of $\Delta x = 9.8(\mu\text{m})$ that is sufficient to resolve the flame structure with more than 10 grid points for all the conditions investigated. As in the one dimensional cases, CHEMKIN PREMIX solutions for a freely propagating H_2 –air flame are used to construct the initial field by placing a planar flame mid-way between the fresh reactants inlet on the left-hand side of the channel and the burnt products outlet on the right-hand side as shown in Fig. 2(b). The initial streamwise velocity field is set to an analytic parabolic profile with a centerline velocity $U_c = 25(\text{m/s})$ while the wall-normal velocity is set to zero everywhere. Again, the reactants' temperature and composition are assumed to be $T_u = 750(\text{K})$ and characterized by fuel-lean, stoichiometric or fuel-rich equivalence ratios, $\phi = 0.5, 1.0, 1.5$, respectively. Open, acoustically non-reflecting inlet and outlet boundaries are placed on the left and right end of the domain, respectively. Perfectly reflecting (acoustically) wall boundaries, that can either allow a hydrogen flux or not, are placed on the upper and lower boundaries of the domain.

Results and discussion

In the present section results from DNS of one-dimensional and two-dimensional laminar FWI configurations are presented. The laminar one dimensional FWI configuration is reported here as a reference case for comparison with existing

literature about head-on quenching of premixed laminar flames impinging on solid walls; the laminar two-dimensional FWI configuration represents a first attempt to investigate the flashback velocities that can be achieved in side-on quenching of a laminar premixed flame propagating in a duct whose walls are providing fuel to the near-wall fluid. Even if laminar channel flow, in the absence of turbulent convection and mixing, represents a limiting worst-case scenario with respect to efficient fuel-oxidant mixture preparation, such flashback speed estimates are nevertheless very valuable in the design of gas turbine burners.

The instantaneous convective wall heat flux, Φ_w , is defined as

$$\Phi_w = -\lambda \left(\frac{\partial T}{\partial x} \right)_w \quad (6)$$

where x is the wall-normal direction, T is the gas mixture temperature and λ is the local thermal conductivity of the gaseous mixture. Quenching is defined as taking place at a time t_q when the wall heat flux reaches its maximum value [16]. When quenching occurs, the flame is at a location x_q and its thickness is reduced to a minimum, δ_q . The quenching Peclet number is given as the ratio of quenching distance to the quenching flame thickness $Pe_q = x_q/\delta_q$. In the discussion that follows, in order to facilitate comparison between the different cases, the quenching wall heat flux is normalized by a reference value, arbitrarily chosen to be the quenching wall heat flux in the case of an impermeable wall and $\phi = 1.0$, that is equal to $\Phi_{ref} = 4.172(\text{MW/m}^2)$, accordingly $q_w^* = \Phi_{w,q}/\Phi_{ref}$. Moreover, the hydrogen flux F_{H_2} is normalized by the nominal flux value that would be achieved for a hydrogen partial pressure on the permeate side equal to zero $F_{H_2}^{\text{max}} = 0.014(\text{kg} \cdot \text{m}^{-2} \cdot \text{s}^{-1})$. The flame heat release rate is subject to a sharp increase during the flame–wall interaction due to radical recombination reactions occurring in the fluid adjacent to the wall [19], and in the figures below it is normalized by its freely propagating value.

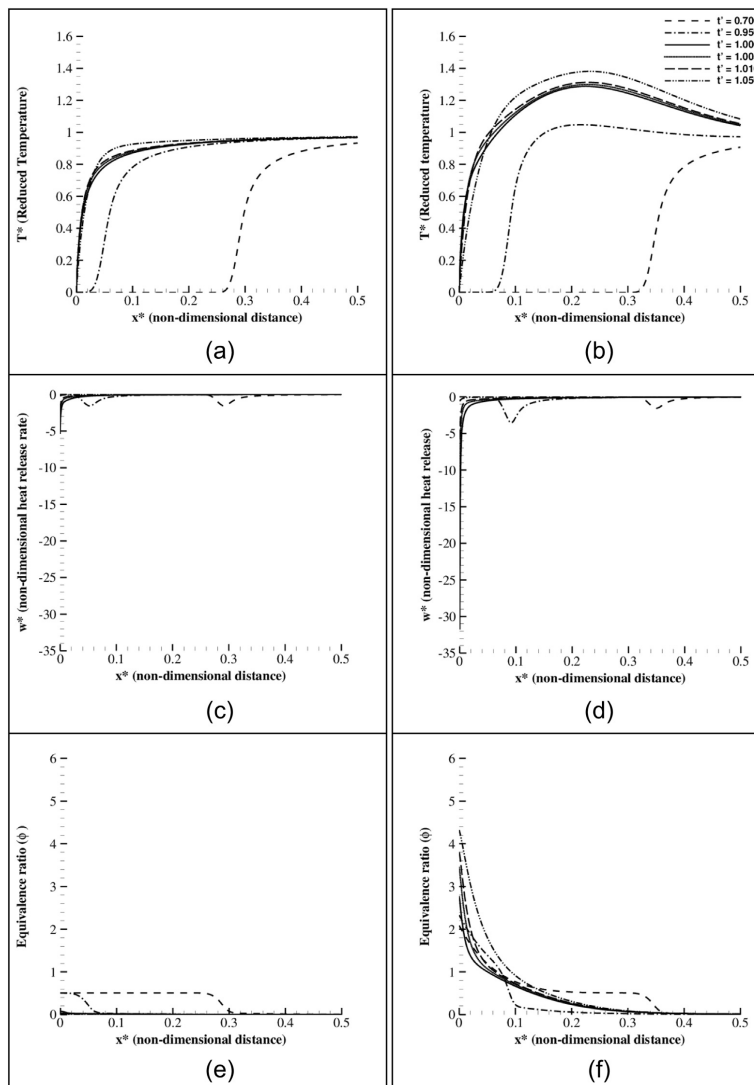


Fig. 4 – Fuel lean case ($\phi = 0.5$): time evolution of the wall-normal profiles of normalized temperature, normalized heat release rate and equivalence ratio for head-on quenching on a solid, impermeable wall (left) and on a membrane wall (right).

The non-dimensional distance to the wall is given by $x^* = x/L_x$. The non-dimensional time is normalized following two different approaches. In the first approach the quantity $t^* = t/t_1$ is defined, where t_1 is the characteristic flame time given as $t_1 = \delta_l/S_l$, where S_l is the freely propagating laminar flame speed and δ_l is the undisturbed, freely propagating, laminar flame thickness given by $\delta_l = (T_b - T_u)/(|\partial T/\partial x|)_{max}$. The quantity t^* is used to compare the time history of the

mass and heat fluxes through the wall for all the simulated cases. For a more meaningful comparison of the time evolution for the spatial profiles of temperature, species, reaction rates etc., the non-dimensional time, $t' = t/t_q$, is used instead of t^* . Accordingly, by definition, quenching takes places always at $t' = 1.0$ in the plots shown below. The non-dimensional temperature is given as $T^* = (T - T_u)/(T_b - T_u)$ in the figures below.

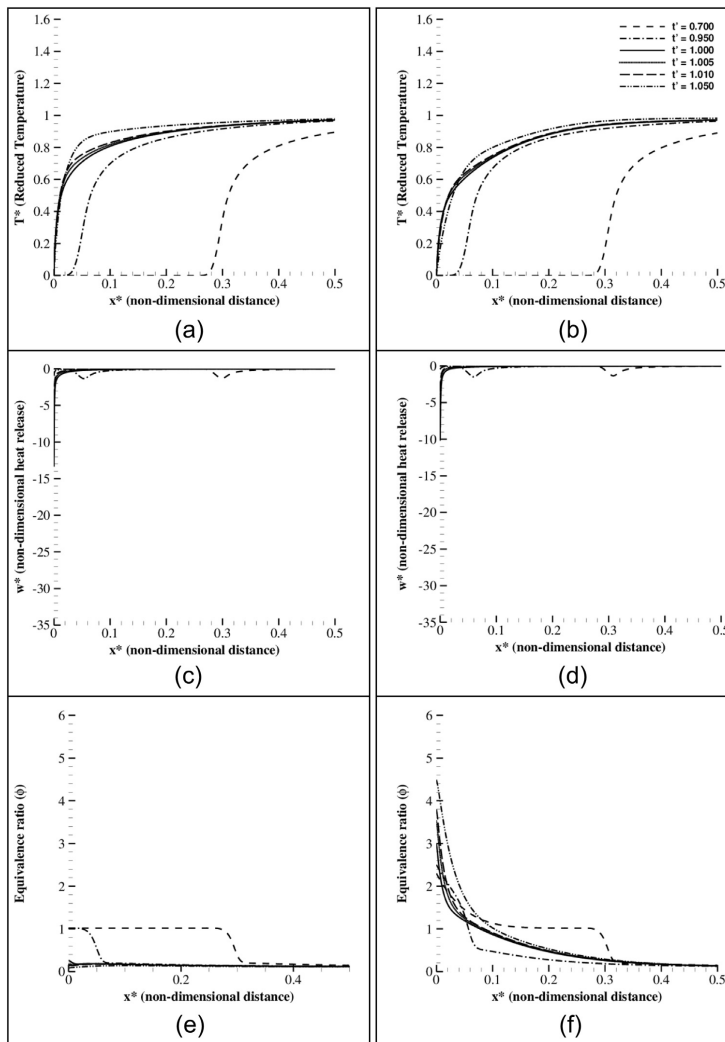


Fig. 5 – Stoichiometric case ($\phi = 1.0$): time evolution of the wall-normal profiles of normalized temperature, normalized heat release rate and equivalence ratio for head-on quenching on a solid, impermeable wall (left) and on a membrane wall (right).

One dimensional flame–wall interaction

Fig. 3 shows the time history of the normalized wall heat flux (for both the solid and permeable wall cases) and the hydrogen mass flux through the H_2 -selective membrane (permeable wall cases only), illustrating the temporal evolution of a typical quenching process for the different mixture stoichiometries simulated. Likewise, Figs. 4–6 present the wall-normal spatial profiles of temperature, heat release rate

and equivalence ratio shown at six different times before, during and after quenching, illustrating the impact of the membrane hydrogen flux on the quenching process (on the right) compared to the impermeable wall case (on the left).

In the standard solid impermeable wall cases, the flames starts propagating freely in the undisturbed fluid away from the wall, and when the flame–wall distance becomes smaller than approximately ten times the flame thickness (for $x^* \leq 0.5$ in the figures), the flames are affected by the

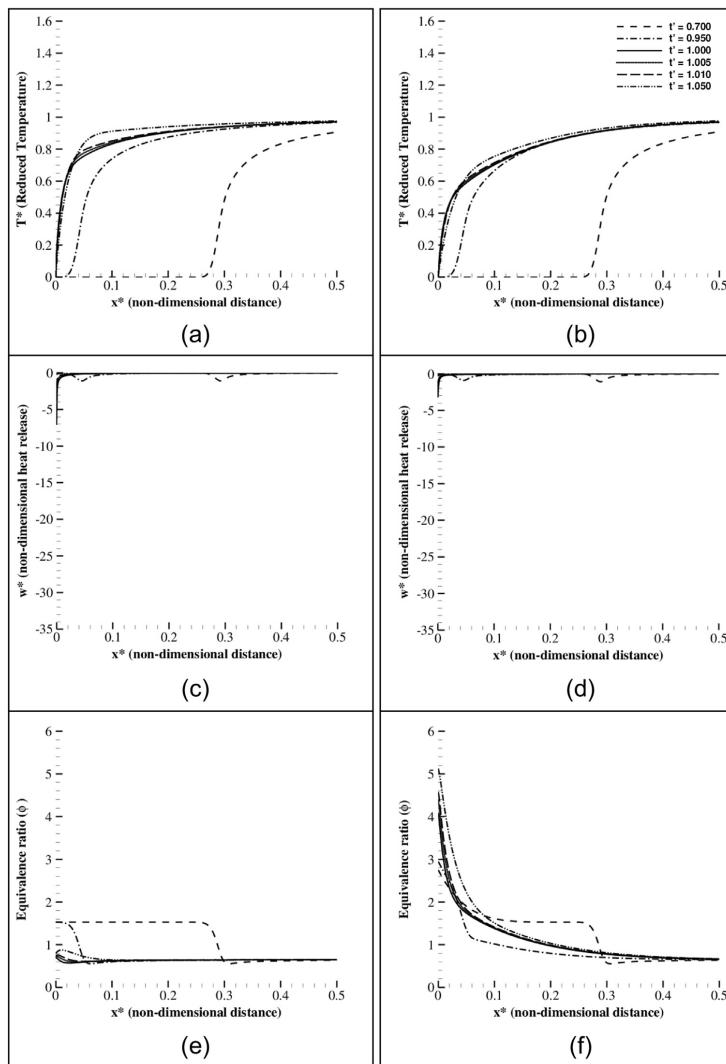


Fig. 6 – Fuel rich case ($\phi = 1.5$): time evolution of the wall-normal profiles of normalized temperature, normalized heat release rate and equivalence ratio for head-on quenching on a solid, impermeable wall (left) and on a membrane wall (right).

presence of the wall, slow down, and become increasingly thinner until quenching occurs at a flame–wall distance of approximately two flame thicknesses (for a typical hydrogen flame). The quenching process involves a considerable increase in the overall flame heat release rate as zero-activation-energy, exothermic, radical recombination reactions occur on the ‘cold’ wall surfaces and deplete the reaction zone of the necessary radical species as discussed previously in [19].

In the case of the initially fuel-lean mixture ($\phi = 0.5$), the wall heat flux at quenching is increased significantly by the presence of the membrane hydrogen flux (approximately by a factor of three), compared to the homologous solid impermeable wall case. In fact, not only does the flame temperature increase as the flame approaches the wall in an increasingly fuel-rich stratified mixture, see Fig. 4(b), but additionally, following the consumption of the fuel that is immediately in contact with the wall, the hydrogen flux through the

membrane spikes due to the sudden reduction in the hydrogen partial pressure on the permeate side, see Fig. 3(b). Hence, the additional membrane hydrogen flux provides abundant fuel for continued combustion in the immediate vicinity of the wall (as a secondary non-premixed flame) with the excess oxygen from the initial (primary) premixed flame. This process ultimately results in a six-fold increase of the quenching heat release rate at the wall compared to the reference impermeable wall case, see Fig. 4(c) and (d). In the case of the initially stoichiometric ($\phi = 1.0$) and fuel-rich ($\phi = 1.5$) flames a radically different trend is observed. Here the presence of the membrane hydrogen flux actually reduces the wall heat flux as the additional fuel does not contribute to an increase in flame temperature but, on the contrary, causes its decrease. There is also no oxygen left to facilitate combustion in a secondary non-premixed flame very close to the wall.

Two dimensional flame–wall interaction

While the one-dimensional direct simulations provide detailed insight into the flame–wall interaction and quenching process, the two-dimensional cases illustrated in Figs. 7 and 8 highlight the impact of the membrane hydrogen flux on the flashback velocities that can be achieved in a duct

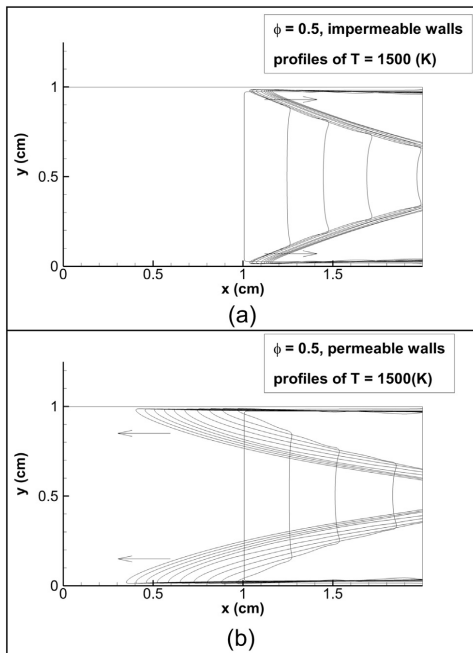


Fig. 7 – Time evolution of the flame position between $t = 0.0(\text{ms})$ and $t = 1.0(\text{ms})$ for the impermeable solid wall case (a) and for the H_2 -selective membrane wall case (b) at fuel-lean conditions ($\phi = 0.5$).

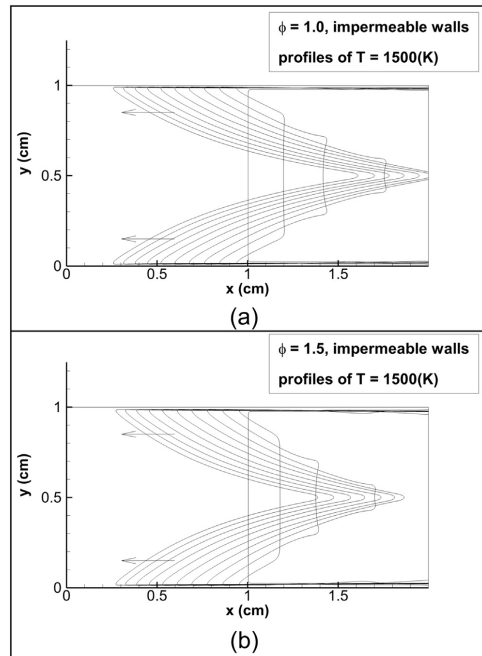


Fig. 8 – Time evolution of the flame position between $t = 0.0(\text{ms})$ and $t = 1.0(\text{ms})$ for the impermeable solid wall cases at stoichiometric (a) and fuel-rich conditions (b), respectively $\phi = 1.0$ and $\phi = 1.5$.

compared to the conventional case with impermeable solid walls. As mentioned in Section 1, in a scenario involving the use of H_2 -selective membranes as fuel injectors, fast removal of highly reactive hydrogen from the near-wall region of the membrane injector and its effective mixing with the oxidant stream to quickly achieve the target equivalence ratio are both major constraints of modern burner design. As an initial step, we investigate flashback in a simple laminar channel flow configuration in order to avoid the complications due to boundary layer turbulence and its impact on flame propagation and flashback velocities [32].

The impact of the membrane hydrogen flux on the flashback behavior is large for the laminar channel flow case. In Figs. 7 and 8 the black lines demarcate the temperature contour of $T(\text{K}) = 1500$ at eleven equally spaced time instants between $t = 0.0(\text{ms})$ and $t = 1.0(\text{ms})$ and allow tracking of the temporally evolving flame front position. In Fig. 7(a) at fuel-lean conditions for the impermeable solid wall configuration, i.e. when no fuel is injected into the near-wall region of the boundary layer, the premixed flame does not propagate upstream in the channel. On the contrary, it is convected downstream towards the right outflow boundary of the computational domain, being blown-off by the approaching reactants flow characterized by a high centerline velocity of

Table 3 – Flashback velocities S_f from the two dimensional cases A, B, C, D.

Case	Approaching flow U_c	ϕ	Walls	Flashback S_f
A	25 (m/s)	0.5	Solid	–1.2 (m/s)
B	25 (m/s)	0.5	Membrane	5.44 (m/s)
C	25 (m/s)	1.0	Solid	6.79 (m/s)
D	25 (m/s)	1.5	Solid	6.75 (m/s)

25(m/s). As soon as the membrane hydrogen flux increases the local equivalence ratio in the near-wall region, the same premixed (but now stratified!) flame propagates quickly upstream towards the reactants inlet on the left boundary of the domain, as shown in Fig. 7(b). Table 3 indicates the flashback velocities, relative to a fixed “laboratory” reference frame, extracted from the numerical simulations by tracking the position of the most upstream portion of the flame front as a function of time. The flashback speed increases from $S_f \sim -1.2$ (m/s), indicative of no flashback but rather flame blow-off, to $S_f \sim 5.44$ (m/s) for the stratified flame, a value that is nearly as high as the flashback velocities observed at the richer equivalence ratios and for impermeable walls.

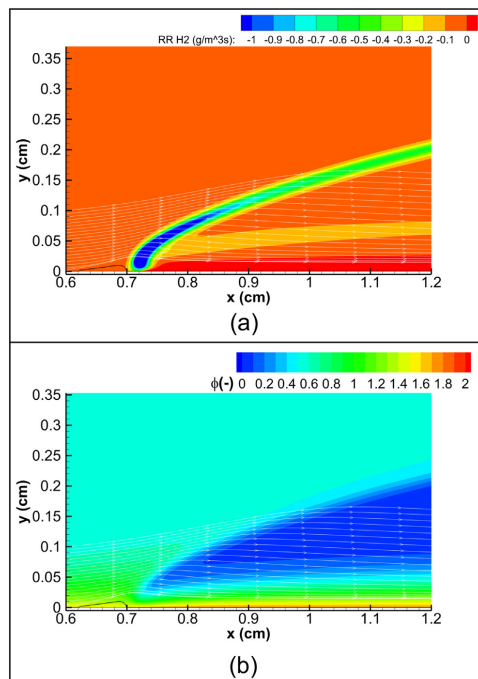


Fig. 9 – Detail of the side-wall quenching region for case B: H_2 fuel reaction rate (a) and local equivalence ratio (b). The white streamlines indicate the flow pattern near the flame quenching region while the black line marks a back-flow pocket located immediately above the wall and upstream of the flame.

Also, clearly visible in Fig. 9 for the $\phi = 0.5$ case is a secondary weaker non-premixed flame branch that combusts the fuel provided through the membrane with the excess oxygen from the primary premixed flame. This double-flame arrangement, consisting of a primary premixed flame and of a secondary non-premixed flame, is only observed in the fuel-lean configuration due to the excess oxygen available. Note also the formation of a back-flow pocket immediately upstream of the flame in the near-wall region. This is a hallmark (present under certain conditions) of premixed flames propagating upstream in laminar or turbulent channel flows leading to accelerated propagation near the wall [45,32]. For the $\phi = 1.0$ and $\phi = 1.5$ cases shown in Fig. 8 the primary premixed flame consumes all available oxygen in its side-on quenching sweep of the boundary layer and eventual additional fuel provided by the membrane remains unburnt and accumulates immediately above the wall.

Conclusions

The present paper investigates flame–wall interaction and quenching of hydrogen–air premixed flames in the case of a permeable wall that is able to supply H_2 fuel to the near-wall region of the flow through a H_2 -selective membrane and compares the results against the standard impermeable wall case. The ultimate aim of this research is the eventual future utilization of porous metal surfaces as a distributed source for injection of highly-reactive hydrogen-rich fuels (thereby replacing traditional fuel nozzles) into the oxidant stream of a gas turbine burner. The present findings show that quenching wall heat flux is increased by a factor of three for the (initially) fuel-lean premixed flame at $\phi = 0.5$ in the presence of a membrane hydrogen flux compared to the standard impermeable wall case. This is due to the higher flame temperature attained in the near-wall region immediately before quenching and to the presence, in the initial mixture, of excess oxygen that continues to burn in a secondary non-premixed flame after quenching of the primary premixed flame. Conversely, the quenching wall heat flux is reduced, compared to the standard impermeable wall cases, for the (initially) stoichiometric and fuel-rich flames in the presence of the membrane. The latter also has a large impact on boundary layer flashback in laminar channel flow configurations, causing the opposite behavior, flashback versus blow-off, for the $\phi = 0.5$ case. Accordingly, it can be concluded that the successful implementation of the novel hydrogen injection strategy suggested here will have to rely on a carefully designed turbulent sweep flow that rapidly removes hydrogen from the near-wall region on the permeate side of the membrane and efficiently mixes it with the combustion air to achieve the target equivalence ratio.

Acknowledgement

This publication has been produced with support from the BIGCCS Centre, performed under the Norwegian research program Centres for Environment-friendly Energy Research

(FME). The authors acknowledge the following partners for their contributions: Aker Solutions, ConocoPhillips, Det Norske Veritas, Gassco, Hydro, Shell, Statoil, TOTAL, GDF SUEZ and the Research Council of Norway (193816/S60). The authors acknowledge Dr. Christopher A. Kennedy for the fruitful collaboration and useful insight provided in respect to the numerical implementation of the wall boundary conditions. The authors also acknowledge the kind assistance by Rune Bredeesen and Thijs Peters from SINTEF Material and Chemistry with valuable contributions within the field of membrane technology. This research was sponsored by the US Department of Energy, Office of Basic Energy Sciences, Division of Chemical Sciences, Geosciences, and Biosciences. Sandia National Laboratories is a multi program laboratory operated by Sandia Corporation, a Lockheed Martin Company, for the US Department of Energy under contract DE-AC04-94-AL85000.

REFERENCES

- Chen JH, Choudhary A, de Supinski B, DeVries M, Hawkes ER, Klasky S, et al. Terascale direct numerical simulations of turbulent combustion using S3D. *CSD* 2009;2:1–31.
- A policy strategy for carbon capture and storage. IEA-Information Paper; 2012. https://www.iea.org/publications/freepublications/publication/policy_strategy_for_ccs.pdf.
- Jordal K. Benchmarking of power cycles with CO₂ capture – the impact of the selected framework. *Int J Greenh Gas Con* 2008;2(4,S1):468–77.
- Foster-Wheeler. Preliminary definition of plants configurations and specifications of membrane operating conditions. Project report in the DEMOYS project, <http://demoys.rse-web.it/Publications/Public-reports.asp>; 2010.
- Johannessen E, Jordal K. Study of a H₂ separating membrane reactor for methane steam reforming at conditions relevant for power processes with CO₂ capture. *Energ Convers Manage* 2005;46:1059–71.
- Bredesen R, Jordal K, Bolland O. High-temperature membranes in power generation with CO₂ capture. *Chem Eng Process* 2004;43(9):1129–58.
- Aasen K, Vigeland B, Nordby T, Larring Y, Mejdell T. Development of a hydrogen membrane reformer based on CO₂ emission free gas power plant. In: *Proceedings of GHGT-7*. <http://uregina.ca/ghgt7/PDF/papers/peer/136.pdf>; 2004.
- Grout R, Gruber A, Yoo C, Chen J. Direct numerical simulation of flame stabilization downstream of a transverse fuel jet in cross-flow. *P Combust Inst* 2011;33(1):1629–37.
- Fritz J, Kröner M, Sattelmayer T. Flashback in a swirl burner with cylindrical premixing zone. *J Eng Gas Turb Power* 2004;126:276–83.
- Grout RW, Gruber A, Kolla H, Bremer PT, Bennet JC, Gyulassy A, et al. A direct numerical simulation study of turbulence and flame structure in transverse jets analysed in jet-trajectory based coordinates. *J Fluid Mech* 2012;706:351–83.
- Kolla H, Grout R, Gruber A, Chen J. Mechanisms of flame stabilization and blowout in a reacting turbulent hydrogen jet in cross-flow. *Combust Flame* 2012;159(8):2755–66.
- Westbrook CK, Adamczyk AA, Lavoie GA. A numerical study of laminar flame wall quenching. *Combust Flame* 1981;40:81–99.
- Hocks W, Peters N, Adomeit G. Flame quenching in front of a cold wall under two-step kinetics. *Combust Flame* 1981;41:157–70.
- Ezekoye O, Greif R, Sawyer RF. Increased surface temperature effects on wall heat transfer during unsteady flame quenching. *P Combust Inst* 1992;24:1465–72.
- Popp P, Smooke M, Baum M. Heterogeneous/homogeneous reaction and transport coupling during flame-wall interaction. *P Combust Inst* 1996;26:2693–700.
- Popp P, Baum M. Analysis of wall heat fluxes, reaction mechanisms, and unburnt hydrocarbons during the head-on quenching of a laminar methane flame. *Combust Flame* 1997;108:327–48.
- Egolfopoulos FN, Zhang H, Zhang Z. Wall effects on the propagation and extinction of steady, strained, laminar premixed flames. *Combust Flame* 1997;109:237–52.
- Dabireau F, Cuenot B, Vermorel O, Poinot T. Interaction of flames of H₂ + O₂ with inert walls. *Combust Flame* 2003;135:123–33.
- Gruber A, Sankaran R, Hawkes ER, Chen JH. Turbulent flame-wall interaction: a direct numerical simulation study. *J Fluid Mech* 2010;658:5–32.
- Lee ST, T'ien JS. A numerical analysis of flame flashback in a premixed laminar system. *Combust Flame* 1982;48:273–85.
- Kurdyumov VN, Fernandez E, Linan A. Flame flashback and propagation of premixed flames near a wall. *P Combust Inst* 2000;28(1):1883–9.
- Kurdyumov VN, Fernandez-Tarrazo E. Lewis number effect on the propagation of premixed laminar flames in narrow open ducts. *Combust Flame* 2002;128:382–94.
- Kurdyumov VN, Fernandez-Tarrazo E, Truffaut JM, Quinard J, Wangher A, Searby G. Experimental and numerical study of premixed flame flashback. *P Combust Inst* 2007;31(1):1275–82.
- Poinot T, Haworth DC, Bruneaux G. Direct simulation and modeling of flame-wall interaction for premixed turbulent combustion. *Combust Flame* 1993;95:118–32.
- Bruneaux G, Akselvoll K, Poinot T, Ferziger JH. Flame-wall interaction simulation in a turbulent channel flow. *Combust Flame* 1996;107:27–44.
- Alshaalan TM, Rutland CJ. Turbulence, scalar transport, and reaction rates in flame-wall interaction. *P Combust Inst* 1998;27:793–9.
- Alshaalan TM, Rutland CJ. Wall heat flux in turbulent premixed reacting flow. *Combust Sci Technol* 2002;174:135–65.
- Kennedy CA, Carpenter MH. Several new numerical methods for compressible shear-layer simulations. *Appl Numer Math* 1994;14(0):397–433.
- Kennedy CA, Carpenter MH, Lewis RM. Low-storage, explicit runge-kutta schemes for the compressible navier-stokes equations. *Appl Numer Math* 2000;35(0):177–219.
- Li J, Zhao Z, Kazarov A, Dryer FL. An updated comprehensive kinetic model of hydrogen combustion. *Int J Chem Kinet* 2004;36:566–75.
- Yoo CS, Im HG. Characteristic boundary conditions for simulations of compressible reacting flows with multi-dimensional, viscous and reaction effects. *Combust Theor Model* 2007;11(2):259–86.
- Gruber A, Valiev D, Chen JH, Law CK. Direct numerical simulation of premixed flame boundary layer flashback in turbulent channel flow. *J Fluid Mech* 2012;709:516–42.
- Sankaran R, Hawkes ER, Chen JH, Lu T, Law CK. Structure of a spatially developing turbulent lean methane-air bunsen flame. *P Combust Inst* 2007;31:1291–8.
- Hawkes ER, Chen JH. Evaluation of models for flame stretch due to curvature in the thin reaction zones regime. *P Combust Inst* 2005;30:647–55.

-
- [35] Hawkes ER, Chen JH. Direct numerical simulation of hydrogen-enriched lean premixed methane-air flames. *Combust Flame* 2004;138:242–58.
- [36] Hawkes ER, Sankaran R, Sutherland JC, Chen JH. Scalar mixing in direct numerical simulations of temporally evolving plane jet flames with skeletal CO/H_2 kinetics. *P Combust Inst* 2007;31:1633–40.
- [37] Echekki T, Chen JH. Direct numerical simulation of autoignition in non-homogeneous hydrogen-air mixtures. *Combust Flame* 2003;134:169–91.
- [38] Sankaran R, Im HG, Hawkes ER, Chen JH. The effects of non-uniform temperature distribution on the ignition of a lean homogeneous hydrogen-air mixture. *P Combust Inst* 2005;30:875–82.
- [39] Strikwerda JC. Initial boundary value problems for incompletely parabolic systems. *Commun Pur Appl Math* 1977;30:797–822.
- [40] Gustafsson B, Sundstrom A. Incompletely parabolic problems in fluid dynamics. *J Appl Math* 1978;35(2):343–57.
- [41] Nordstrom J, Svard M. Well posed boundary conditions for the navier-stokes equations. *J Numer Anal* 2005;43(3):1231–55.
- [42] Peters TA, Kaleta T, Stange M, Bredesen R. Development of thin binary and ternary Pd-based alloy membranes for use in hydrogen production. *J Membr Sci* 2011;383(1–2):124–34.
- [43] Peters TA, Stange M, Bredesen R. On the high pressure performance of thin supported Pd-23%Ag membranes – evidence of ultrahigh hydrogen flux after air treatment. *J Membr Sci* 2011;378(1–2):28–34.
- [44] Ward TL, Dao T. Model of hydrogen permeation behavior in palladium membranes. *J Membr Sci* 1999;153(2):211–31.
- [45] Eichler C, Sattelmayer T. Premixed flame flashback in wall boundary layers studied by long-distance micro-piv. *Exp Fluids* 2012;52(2):347–60.

Article 2

Premixed hydrogen-air flames interacting with a hydrogen porous wall

Prashant S. Salimath, Ivar S. Ertesvåg, Andrea Gruber

Published in International Journal of Hydrogen Energy

Available online at www.sciencedirect.com

ScienceDirect

journal homepage: www.elsevier.com/locate/he

Premixed hydrogen-air flames interacting with a hydrogen porous wall

Prashant S. Salimath^a, Ivar S. Ertesvåg^{a,*}, Andrea Gruber^b^a Department of Energy and Process Engineering, NTNU Norwegian University of Science and Technology, Kolbjørn Hejes vei 1b, NO-7491 Trondheim, Norway^b SINTEF Energy Research, Trondheim, Norway

ARTICLE INFO

Article history:

Received 7 September 2017

Received in revised form

22 December 2017

Accepted 27 December 2017

Available online 1 February 2018

Keywords:

Permeable wall

S3D

Head on quenching

Flame-wall interaction

Wall heat flux

Detailed chemical mechanism

ABSTRACT

A laminar one-dimensional hydrogen-air flame travelling and quenching towards a chemically inert permeable wall (PW) is studied. Hydrogen flows through the wall into the premixed H₂-air. The S3D numerical code with detailed chemistry is used. PW results are compared against results of an impermeable wall (IW), including effects of varying wall mass flux, stoichiometry, inert dilution and unburned-gas and wall temperatures. The maximum reaction heat release rate occurs at the wall in all cases. For rich and stoichiometric mixtures, PW with fuel influx gave a moderate reduction of the quenching (i.e. maximum) wall heat flux compared to IW, whereas for a lean mixture, the increase is considerable. Effects of the fuel influx on the importance of individual elementary reactions and radicals and intermediate species are investigated. The lean PW cases have similarities to much richer IW cases. Both a lower wall temperature and dilution reduce the burned-mixture temperature and, consequently, the wall heat flux.

© 2018 Hydrogen Energy Publications LLC. Published by Elsevier Ltd. All rights reserved.

Introduction

Thermal degradation of hardware parts that are subjected to large wall heat fluxes during flame-wall interactions (FWI) is a critical issue in many energy conversion devices, such as internal combustion engines, gas turbine combustors and furnaces. The premixed FWI can be described as coupled thermochemical processes involving high temperature, propagating premixed flames impinging on colder walls, where flame quenching occurs at a normal distance from the wall known as quenching distance [1–9]. Dreizler and Böhm [10] reviewed numerical and experimental FWI studies. They discussed the

role of laser diagnostics development and validation of collected data through numerical simulations.

Flame quenching occurs with a large heat release near the wall, and the resulting wall heat flux reaches its maximum value. Accurate determination of the quenching distance and the corresponding wall heat flux is significant, as strong thermal gradients occur near the wall, affecting hardware durability, pollutants formation and engine performance. The different stages of FWI mechanisms are understood through high-fidelity numerics in simple laminar premixed flame configurations in one-dimensional (1-D) head-on quenching and 2-D side-wall quenching configurations.

* Corresponding author.

E-mail addresses: Prashant.Salimath@ntnu.no (P.S. Salimath), Ivar.S.Ertesvag@ntnu.no (I.S. Ertesvåg), Andrea.Gruber@sintef.no (A. Gruber).<https://doi.org/10.1016/j.ijhydene.2017.12.166>

0360-3199/© 2018 Hydrogen Energy Publications LLC. Published by Elsevier Ltd. All rights reserved.

Studies of transient quenching processes of flames have employed single-step and multi-steps chemical mechanisms. For low wall temperatures (around 300 K), the wall heat fluxes predicted by single-step chemical mechanisms have been seen to compare reasonably well to experimental observations. However, for higher wall temperatures these simple mechanisms have appeared to fail [4,11,12]. At high wall temperatures (above 400 K), it has been shown [6] that chemical processes play a significant role near the wall, involving exothermic radical recombination reactions. The detailed multi-step mechanisms employed in numerical codes have predicted well for wall heat fluxes and provided better understanding of radical recombination reactions involving radicals near the wall. Gruber et al. [3] showed that the role of exothermic radical recombination reactions was significant and contributed to 70% of the overall heat release at the wall for a laminar premixed hydrogen-air flame. Dabireau et al. [5] demonstrated that in a premixed $H_2 - O_2$ flame, the recombination reactions and reactions of intermediate species (HO_2, H_2O_2) together contributed 30% of the predicted wall heat flux.

Experimental study of FWI processes with quenching distances less than 1 mm near a wall is difficult due to strong thermal gradients [12,13]. Therefore, we tend to rely on numerical simulations. FWI processes of impermeable wall configurations are described by a normalized wall heat flux and the quenching Peclet number, defined as the position of maximum fuel consumption rate and normalized by the flame thickness. For hydrocarbon fuels, it has been observed that the wall heat flux is inversely proportional to the flame quenching distance with an assumption that no thermal boundary layer exists between the wall and the near-wall unburnt mixture [9,12,14,15]. Studies of hydrogen flames showed that their FWI behaviour differs from that of hydrocarbon flames for wall temperature maintained at 750 K, when quenching of the flame occurred much closer to the wall [5,7,16]. Owston et al. [7] extended the physical problem of [5] to a range between 298 and 1200 K and concluded that radical recombination reactions play a significant role in the evaluation of wall heat flux at higher wall temperatures.

The paper by Gruber et al. [17] (with two of the present authors) appears to be the first on numerical investigations on a fuel flux through a permeable wall into a flame. This potentially new design approach for combustion devices as a porous fuel diffuser possibly coated with H_2 selective permeable wall can replace conventional fuel nozzles and provide

in-situ CO_2 – separation from the hydrogen fuel that is injected on the permeate side for mixing with the oxidant and combustion further downstream [18]. The hydrogen gas wall-permeation rate can influence the wall heat flux and avoid a flame coming very close to the wall. Hence, thermal degradation of hardware parts can potentially be reduced in comparison to an impermeable wall. Gruber et al. [17] discussed the transient nature of laminar FWI processes in 1-D and 2-D configurations and indicated a strong feedback mechanism between the permeating hydrogen flux and the flame on the permeate side.

A planar flame front propagates through a premixed fuel/air mixture towards a solid wall facing the flame. When reaching the wall, the flame quenches. The process can be analyzed as a 1-dimensional case, and is illustrated schematically in Fig. 1 for an impermeable wall (IW) and a fuel-permeable wall (PW) configuration. Both walls have chemical inert properties, that is, no adsorption or catalytic effects. In the PW case, the flame is partly premixed, as pure fuel (here H_2) flows into the domain and mixes with premixed fuel-air mixture on the permeate side.

Some aspects of the problem were considered by Gruber et al. [17] as part of a larger study. Numerical simulations with a detailed chemical mechanism and diffusion mechanisms were conducted for laminar hydrogen-air flames at atmospheric pressure on a planar and permeable (hydrogen selective) wall at constant wall temperature of 750 K and different H_2 /air mixtures. It was found that for IW, the wall heat flux ($-\phi_w$) was slightly reduced and the quenching delayed in time as the undisturbed-mixture equivalence ratio (ϕ_u) was increased from 0.5 (fuel lean) to 1.5 (fuel rich). The net reaction heat release had its maximum point at the wall and it was larger for a stoichiometric mixture than for rich or lean mixtures. The temperature of the reacted mixture close to the wall around quenching approached, but was less than, the burned temperature of the freely propagating flame. The local equivalence ratio decreased towards the burned-mixture value as the flame front reached the wall and quenched. The PW cases of 17 were all conducted with a single permeate feed pressure (10 bar).

In the present paper, the physical problem is extended to operate the porous fuel diffuser configuration with different feed pressures at the porous wall. The resulting variation in hydrogen flow through the membrane influences the local chemistry near the wall and the heat transfer. We will also investigate FWI characteristics of the PW configuration,

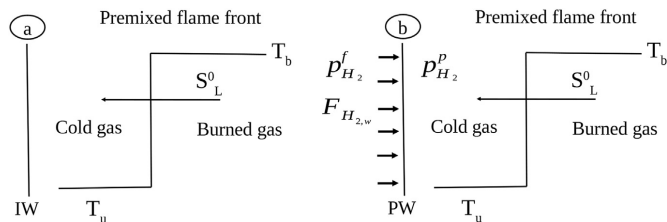


Fig. 1 – Head-on quenching configurations of (a) Impermeable wall (IW) and (b) Permeable wall (PW) with hydrogen flux in accordance with Eq. 5.

influence of hydrogen mass flux on heat release rates near the wall and of varying feed pressure and equivalence ratio. Contributions of the individual elementary reactions will be studied more in detail. Furthermore, effects of dilution with N_2 (inert) and H_2O (participating) will be studied.

These studies can aid in better understanding of flame chemistry near the permeable wall. They can also provide novel concepts for hardware components referred to as impermeable walls with some degree of permeability of fuel such that large wall thermal fluxes are avoided. Some permeation of fuel through a basically impermeable wall can alter the local chemistry for a given stoichiometry during operation.

The following section will describe the choice of models and the numerical setup, including hydrogen flow across the wall through a membrane, numerical methods used for DNS studies, computational setup for performing 1-D transient runs, permeable wall boundary condition formulation and definitions related to FWI as well as some of the basic characteristics of the laminar, undisturbed flame in so far as it is important for the understanding of the flame-wall interaction results in the present paper. Sections 3 and 4 show results and following discussion. Finally, conclusions are presented.

Numerical setup and choice of models

Governing equations

The following equations represent governing reacting flows and are written in conservative form as [19].

$$\frac{\partial \rho}{\partial t} = \frac{\partial}{\partial x_\alpha} (-\rho u_\alpha), \quad (1)$$

$$\frac{\partial}{\partial t} (\rho u_\alpha) = \frac{\partial}{\partial x_\beta} (-\rho u_\alpha \cdot u_\beta) + \frac{\partial}{\partial x_\beta} (\tau_{\beta\alpha}) - \frac{\partial p}{\partial x_\alpha}, \quad (2)$$

$$\frac{\partial}{\partial t} (\rho e_0) = \frac{\partial}{\partial x_\beta} [-(\rho e_0 + p) u_\beta] + \frac{\partial}{\partial x_\beta} (\tau_{\beta\alpha} \cdot u_\alpha) - \frac{\partial \Phi_\beta}{\partial x_\beta}, \quad (3)$$

$$\frac{\partial (\rho Y_k)}{\partial t} = \frac{\partial}{\partial x_\beta} (-\rho Y_k u_\beta) + \frac{\partial}{\partial x_\beta} (-\rho Y_k V_{\beta k}) + \dot{\omega}_k \quad (4)$$

Mass flux through permeable wall

The hydrogen permeation through permeable wall (also referred as membrane wall) is based on Sieverts' law of hydrogen diffusion in thin Pd-Ag based membranes. The hydrogen flux formulation is based on palladium or palladium alloy membranes that proceeds via a solution-diffusion mechanism and generally expressed for species H_2 as [17,20,21].

$$F_{H_2,w} = Q^* \cdot W_{H_2} \left((p_{H_2}^f)^n - (p_{H_2}^p)^n \right), \quad (5)$$

where Q^* and n are the membrane permanence factor and the pressure exponent, respectively, of Pd-based membranes. For typical 2–3 μm Pd-based membrane thickness, these values were set to $Q^* = 7.0 \cdot 10^{-6} \text{ kmol}/(\text{m}^2 \text{sPa}^{0.5})$ and $n = 0.5$ [17,20].

Table 1 – Elementary reactions in the $H_2 - O_2$ chemical mechanism, Li et al. [22].

No.	Reactions
R1	$O_2 + H \rightleftharpoons OH + O$
R2	$H_2 + O \rightleftharpoons OH + H$
R3	$OH + H_2 \rightleftharpoons H + H_2O$
R4	$H_2O + O \rightleftharpoons 2OH$
R5	$H_2 + M \rightleftharpoons 2H + M$
R6	$2O + M \rightleftharpoons O_2 + M$
R7	$H + O + M \rightleftharpoons OH + M$
R8	$OH + H + M \rightleftharpoons H_2O + M$
R9	$O_2 + H + M \rightleftharpoons HO_2 + M$
R10	$H + HO_2 \rightleftharpoons O_2 + H_2$
R11	$H + HO_2 \rightleftharpoons 2OH$
R12	$O + HO_2 \rightleftharpoons OH + O_2$
R13	$OH + HO_2 \rightleftharpoons O_2 + H_2O$
R14	$2HO_2 \rightleftharpoons O_2 + H_2O_2$
R15	$H_2O_2 + M \rightleftharpoons 2OH + M$
R16	$H + H_2O_2 \rightleftharpoons OH + H_2O$
R17	$H + H_2O_2 \rightleftharpoons H_2 + HO_2$
R18	$O + H_2O_2 \rightleftharpoons HO_2 + OH$
R19	$OH + H_2O_2 \rightleftharpoons H_2O + HO_2$

Chemical mechanism

The hydrogen-oxygen chemistry was described by the mechanism of Li et al. [22], with 8 species (H_2 , O_2 , H_2O , OH , H , O , HO_2 and H_2O_2) and 19 steps, supplemented with N_2 as an inert gas. This approach enabled identifying the most important species, radicals and reaction rates during the flame quenching process. Table 1 lists the 19 two-way elementary reactions, which will be denoted as R1 to R19 with the enumeration in accordance with [22] (also in Ref. [17]) and f and r denoting forward and reverse reactions.

Numerical method

The 3-D code S3D, developed at Sandia National Laboratories, was modified for the one-dimensional configuration to perform FWI simulations. The compressible Navier-Stokes equations were solved in conservative form on a structured mesh. The code used the Message Passing Interface (MPI) for inter-process communication in parallel execution [23] and can easily be ported in different architectures [24] for different high end performance studies [3,24–29].

The solver had a non-dissipative numerical scheme with an eight-order explicit central differential scheme in space (third order, one-sided stencils at the domain boundaries) and a fourth-order explicit Runge-Kutta method in time [30]. High-frequency spurious fluctuations and aliasing errors in solutions were removed using a tenth-order purely dissipative spatial filter.

The constitutive relationships, such as ideal gas equation of state, models for reaction rates, molecular transport and thermodynamic properties details, were described in Ref. [19]. The code could handle multi-step chemistry. The thermodynamic properties and mixture-averaged transport properties were evaluated through linking of Chemkin and Transport software libraries [31,32] to the S3D solver.

Boundary conditions

The permeable wall boundary formulation was based on no-slip, isothermal and species zero-gradient conditions, except for H_2 . The hydrogen mass fraction gradient at the wall was set by the expression for permeability, $F_{H_2,w}$ (Eq. (5)). The well-posed solution [33–35] for the permeable wall can be expressed as

$$u_n = 0, \quad (6)$$

$$T_w = T_u, \quad (7)$$

$$\left(\frac{\partial Y_{H_2}}{\partial x_n} \right)_w = \frac{F_{H_2,w}}{\rho_w D_{mix,w}} \quad (8)$$

and

$$\left(\frac{\partial Y_k}{\partial x_n} \right)_w = 0 \text{ for } k \neq H_2 \quad (9)$$

In the wall-normal direction, the non-zero velocity component was estimated as $u_1 = F_{H_2,w}/\rho_{H_2}$. The wall pressure gradient was expressed by inserting the species mass fluxes $F_k = \rho_k u_n$ into the momentum equation (Eq. (2)), with the assumption of wall-normal gradients of these fluxes set to zero. The pressure gradient at the wall was then obtained as

$$\left(\frac{\partial P}{\partial x_n} \right)_w = - \left(\sum_{k=1}^{N_g} \frac{\partial F_{k,w}}{\partial t} \right) - \left(\frac{\partial u_n}{\partial x_n} \sum_{k=1}^{N_g} F_k \right)_w + \left(\frac{\partial \tau_{nn}}{\partial x_n} \right)_w \quad (10)$$

Here, only hydrogen contributed to the sum taken over all gases. The first and second terms on the right hand side of Eq. (10) represent the unsteady and steady terms as consequences to wall-normal momentum of the permeable wall due to hydrogen flux. At the wall, the mass fractions of species ($Y_{k,w}$) and the pressure (P_w) were extracted by inverting the numerical stencil. The density at the wall, ρ_w , could then be updated using these values and the wall temperature in the ideal-gas equation of state.

The impermeable wall boundary condition was similar to the above, with the simplification that no mass penetrated the wall. That is, Eq. (9) was used for H_2 as well, and the RHS of Eq. (10) was reduced to the viscous term.

For the outflow boundary at the right-hand side of the domain, the Navies-Stokes characteristic boundary conditions (NSCBC) [36,37] were used for both IW and PW cases.

Definitions, non-dimensional quantities

The incident wall heat flux was calculated as $\phi_w = \lambda(\partial T/\partial x)_w$. The maximum value that occurred at quenching was denoted as $\phi_{w,Q}$. The quenching instance was taken as the time when the wall heat flux had its maximum value [6]. During the quenching process, we tracked the flame position through the locations of the maximum reaction heat release rate ($y_{o_{F,max}}$) and the maximum fuel consumption rate ($y_{o_{F,max}}$) in the flame. The corresponding wall-to-flame distances were normalized by the characteristic flame thickness $\delta_L = \lambda_u/(\rho_u C_{p,u} S_L^0)$ [5] to yield the respective Peclet numbers, $Pe = y_{o_{F,max}}/\delta_L$ and $Pe_F = y_{o_{F,max}}/\delta_L$.

The flame speed S_L^0 , the flame thickness δ_L and the laminar flame power $q_L^0 = \rho_u C_{p,u} S_L^0 (T_b - T_u)$ were calculated for the flame propagating through the undisturbed gas mixture before reaching the wall. The burnt temperature T_b was evaluated as the equilibrium adiabatic flame temperature of this freely propagating flame. The thermal flame thickness was defined as $\delta_L^0 = (T_b - T_u)/(\partial T/\partial x)_{\max}$ [14] and the non-dimensional flame thickness as $\delta_L^* = \delta_L^0/\delta_L$.

Non-dimensional variables were introduced, such as the heat release rate $\dot{\omega}^* = \dot{\omega} \delta_L/q_L^0$ and fuel consumption rate $-\dot{\omega}_F^* = \int_0^L (-\dot{\omega}_F) dx / (\rho_u S_L^0 Y_{F,u})$. The non-dimensional wall heat flux was given as $\phi_w^* = \phi_w/q_L^0$.

All time instants were normalized by the laminar flame timescale as $t^* = t \cdot S_L^0/\delta_L$. In the cases of PW, the normalized mass flux was defined as $F_{H_2,w}^* = F_{H_2,w}/F_{H_2,w}^{\max}$, where $F_{H_2,w}^{\max}$ was the maximum wall mass flux evaluated (Eq. (5)) for a zero hydrogen partial pressure on the permeate side.

The timescale of flame-wall interaction for head-on quenching, t_{FWI} , was defined [13] as the time required for ϕ_w to reach the maximum wall flux from one-half of this maximum. It was normalized as $t_{FWI}^* = t_{FWI} \cdot S_L^0/\delta_L$.

Specifications of the present investigations

The initial flow field of each H_2 -air flame was placed in the center of the one-dimensional domain. The quiescent initial field solutions were computed based on Chemkin Premix [32]. A progress variable function was used in the initialization to map all points in the one-dimensional domain taken from Chemkin Premix.

The computational domain had a length of $L = 0.02$ m and was characterized by a uniform mesh in the wall-normal direction. The number of nodes, $N = 4096$, was chosen from a grid sensitivity study for PW cases (see Sect. 3.1). The time step was fixed at $1.0 \cdot 10^{-9}$ s for all simulations.

The species mass balance, Eq. (4), was solved for all species but N_2 , which was determined from continuity of mass. The species reaction rates and all thermal properties were calculated at every step of the iteration.

The Soret effect (thermo-diffusion) and pressure diffusion were taken into account, whereas the Dufour effect was not implemented in S3D [19]. Radiation heat transfer and body-force effects (gravity) were neglected.

Air was assumed as a mixture of 79% N_2 and 21% O_2 , molar based. The pressure of the gas mixture was maintained at 1 atm. The temperature of the unburned gas and the wall was specified at $T_u = T_w = 750$ K, except when the effects of this temperature was studied (then, 300 K and 500 K). The initial velocities were set to zero for all cases.

Four PW cases of constant $p_{H_2}^f = 10.0, 5.0, 2.0$ and 1.0 atm and the IW case were investigated for each of four fuel-air conditions, $\phi_u = 0.5, 0.8, 1.0$ and 1.5 . These equivalence ratios pertained to the undisturbed mixture, unaffected by the fuel influx from the wall. Accordingly, for PW the permeation commenced at $t = 0$. Due to lack of experimental results on PW configurations, the results were compared against the impermeable wall configuration for validation purposes. This can also give comparison to previous flame quenching results for hydrogen flames [5,7].

In the previous study [17] was seen that for PW, the local equivalence ratio at the wall was in the range 3–5. Therefore, an IW case was run here with $\phi_u = 4.0$ ($T_u = T_w = 750$ K) for comparison with the leaner PW. Furthermore, cases with dilution by N_2 and H_2O were investigated, and also cases with lower unburnt-gas and wall temperature, as specified in Sections 3.4 and 3.5 below.

Results

Initial investigations for validation

In order to ensure quasi-steady conditions, the flame profile was initiated sufficiently far from the wall (i.e. $x = L/2$) before the flame propagated towards the wall. The initialization method described in Sect. 2.7 yielded marginally incorrect initial fields during flame set-up. Initial spurious oscillation was observed in the transient term at $t^* = 58.5$. This indicated discontinuities, however, which could be ignored as the behaviour was short and far from the flame quenching time. The propagating flame readjusted within the unburnt mixture and reached a nearly constant flame speed until it sensed the presence of the wall or enriched hydrogen fuel concentration due to permeation. Therefore, the period before $t^* = 60$ was ignored in the analyses of the results.

The quenching times were quite similar for both cases, $t_Q^* = 501.8$ for IW and $t_Q^* = 503.97$ for PW. The actual values depend on the initial location of the flame and are not directly comparable to other studies. A difference was seen as for PW, the wall influence commenced much earlier, at approximately 0.80 times t_Q^* compared to 0.98 for IW. The first influence was weak, but an increased depletion (outflow) of mass was clearly seen in the results, although the permeation added mass to the system.

The total depletion of mass of the system for the time interval from $t^* = 60$ to 1640 was $1.48 \cdot 10^{-3}$ kg/m² (22% of the original mass) and $1.69 \cdot 10^{-3}$ kg/m² (25%), respectively, for IW and PW.

A sensitivity study was performed to find the sufficient resolution required to capture the wall thermal flux and the flame thickness during quenching. Table 2 presents this examination performed for PW cases at stoichiometric conditions with a varying number of grid points (N) for a feed pressure of $p_{H_2}^f = 10$ atm. It shows that for $N = 4096$, the quenching thermal flame thickness was then captured by a number of gridpoints, $M = 24$. Table 3 presents computations for varying ϕ_u at $N = 4096$. The results showed that this resolution captured the quenching flame thickness by 22–27

nodes for the PW cases and by 12–20 nodes for the IW cases. It was assumed that a resolution of 10 is sufficient [3]. Accordingly, $N = 4096$ was used for all cases.

Flame wall interaction (FWI) characteristics

Graphs showing the time evolution of wall-normal profiles of the normalized temperature, the normalized reaction heat release rate and the local equivalence ratio was shown by Gruber et al. [17] for undisturbed equivalence ratios ϕ_u of 0.5, 1.0 and 1.5, a wall temperature of 750 K and a feed pressure of $p_{H_2}^f = 10$ bar. These graphs are not repeated here.

Figs. 2 and 3 display FWI characteristics (δ_L^* , $-\dot{\omega}_F^*$, $\dot{\omega}^*$, Pe , Pe_F) plotted against non-dimensional time (t^*) for the case of $\phi_u = 1.0$, $T_u = T_w = 750$ K, $p_{H_2}^f = 10$ atm and $N = 4096$. These figures present the premixed head-on-quenching process split into three stages [5]: Stage I is the undisturbed propagation. In Stage II, the wall influences the flame, while in Stage III, the overall reaction rate and wall heat flux decreases after quenching. Due to the hydrogen inflow, the ranges of these stages differs for PW compared to IW. In the undisturbed flow, the mass consumption rate and heat release rate were $-\dot{\omega}_F^* = 0.3015$ and $\dot{\omega}^* = 0.0414$. For IW, the former just declined towards zero after quenching, while the heat release rate came to a peak value of $\dot{\omega}^* = 0.4085$ at $t^* = 503.0$ and then declined. For PW, both rates peaked: $-\dot{\omega}_F^* = 0.3538$ at $t^* = 478.0$ and $\dot{\omega}^* = 0.3434$ at $t^* = 503.3$. The maximum heat release rate reached the wall ($Pe = 0$) at $t^* = 496.5$ for IW and at $t^* = 497.8$ for PW. The flame thickness came to a minimum of $\delta_L^* = 3.775$ for IW at $t^* = 501.8$, that is, after quenching. For PW, it first had a minor increase and then fell to its minimum value just before quenching; $\delta_L^* = 5.874$ at $t^* = 503.8$.

During the flame quenching process, the transient wall heat flux peaked due to a large overall heat release rate at the wall for both IW and PW. The heat release rates of the individual elementary reactions are shown in Fig. 4 and compared to the overall heat release. The heat release rates shown here and in Fig. 2 were calculated for the location of maximum net heat release rate. The cases of Figs. 4 and 5 were the same as in Figs. 2 and 3.

The transient wall H_2 mass flux of the PW configuration will be shown below. At stoichiometric conditions it spiked to a non-dimensional value of 0.81 at quenching from the value 0.79 just before.

Fig. 5 displays transient mass fraction of all species (except N_2) at the wall (i.e. $x = 0$) for both IW and PW configurations.

Effects of varying feed pressure and equivalence ratio on PW configurations

In the following simulations the feed pressure ($p_{H_2}^f$) was varied, while the undisturbed gas mixture on the permeate side had stoichiometric conditions.

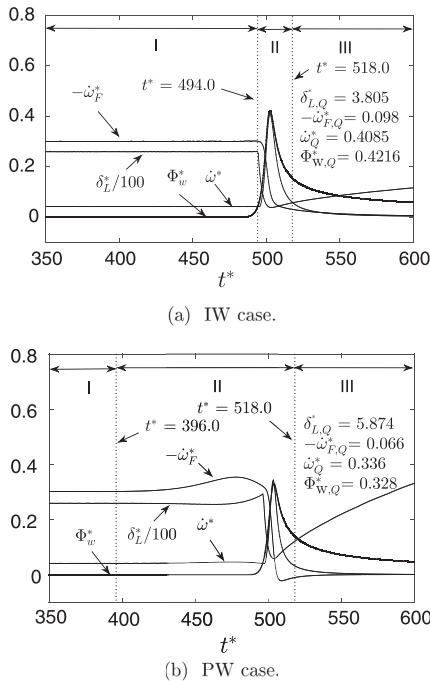
Fig. 6 shows the transient wall heat fluxes and wall H_2 mass fluxes of four PW cases and the corresponding IW case at stoichiometric conditions. It was seen that increasing the feed pressure at the wall reduced the wall heat flux and delayed the quenching. Increasing feed pressure at the wall provided a higher hydrogen flux, influencing exothermic recombination reactions, mainly R8f, R9f and R11f, to reduce significantly the

Table 2 – Flame properties with varying grid points (N), obtained for PW cases at $\phi_u = 1.0$ and $p_{H_2}^f = 10$ atm.

N	δ_L^*	$\delta_{L,Q}^*$	$\Phi_{w,Q}$	M
[–]	[–]	[–]	[MW/m ²]	[–]
1024	26.60	8.56	2.752	9
2048	26.01	7.23	3.130	15
4096	25.90	5.87	3.295	24
8192	25.88	5.86	3.300	48

Table 3 – Flame properties obtained for varying ϕ_u with given $N = 4096$ and $p_{H_2}^f = 10$ atm.

Wall type	ϕ_u [–]	S_L^0 [m/s]	δ_L [10^{-6} m]	q_l^0 [MW/m ²]	T_b [K]	δ_L^* [–]	$\delta_{L,Q}^*$ [–]	$\Phi_{w,Q}$ [MW/m ²]	M [–]
IW	0.5	6.40	26.11	4.12	2017.5	19.78	3.84	1.092	20
IW	1.0	10.8	19.73	10.05	2597.3	25.90	2.93	4.230	12
IW	1.5	12.5	19.88	11.22	2539.4	24.90	3.39	7.698	14
PW	0.5	6.40	26.11	4.12	2017.5	19.78	4.11	3.462	22
PW	1.0	10.8	19.73	10.05	2597.3	25.90	5.87	3.295	24
PW	1.5	12.5	19.88	11.22	2539.4	24.06	6.41	2.957	27

**Fig. 2 – Non-dimensional characteristic parameters versus non-dimensional time of premix FWI cases: Impermeable (top) and Permeable (bottom) wall boundaries. The unstretched laminar flame thickness and quenching values are included.**

overall heat release rate. Increasing the H_2 wall flux promoted Reaction R5r such that exothermic recombination reactions at the wall were reduced in magnitude. The lower feed pressures ($p_{H_2}^f$ at 1.0 and 2.0 atm) gave quenching earlier than IW and at larger wall heat fluxes. The increased normalized hydrogen fluxes had lesser peaks at quenching for higher feed pressures.

For the rich and lean mixtures, FWI characteristics behaved qualitatively similar to the stoichiometric mixture described by Figs. 2–6. Among the few deviations were the wall heat transfer (reported in Fig. 3 of Gruber et al. [17]); that

is, higher values with lower equivalence ratio for PW and vice versa for IW. Another observation here was that for the stoichiometric case (cf. Fig. 6a) and (more notable for) the rich case, increased feed pressure (increased wall influx) gave a delayed and reduced peak wall heat flux. For the lean case, the tendency was not as clear. Furthermore, for the rich flame Pe_F went to zero just before quenching and remained so for a while, whereas it for the stoichiometric and lean cases rose to a high value (cf. Fig. 3b). For the lean PW case, contrary to the stoichiometric case, Pe_F declined quite fast after the spike.

Fig. 7 shows the normalized values for the wall H_2 mass flux, wall-to-flame distance (i.e., Peclet number) and the wall heat flux at quenching for varied feed pressure and equivalence ratio. The results obtained for the investigated cases are shown as points in the graphs. The lines between the points do not show more results but were supplemented to ease reading.

Since the local partial H_2 pressure just inside the wall ($p_{H_2}^p$) is directly related to $p_{H_2}^f$ and $F_{H_2,w}$ through Eq. (5), Figs. 6b and 7a also indicate on that quantity.

It should be noted that the denominator of the dimensionless flux shown in Fig. 7a increases with the feed pressure, while it is independent of the equivalence ratio. This means that the absolute values increase more with feed pressure than those shown. The denominator of the Peclet number (laminar flame thickness) increases with increasing deviation from stoichiometry, while the denominator of the dimensionless heat flux (flame power) decreases. Both these denominators are independent of the feed pressure. Accordingly, the dimensional counterparts of Fig. 7b and c showed curves that were more assembled for PW. In particular, the lean cases were close to the stoichiometric cases. In other words, the dimensional wall heat flux at quenching (i.e. the maximum wall heat flux) was minorly affected by the initial equivalence ratio (ϕ_u) of the mixture. Increasing the feed pressure from 1 to 10 atm reduced the wall heat flux by about one-fourth, while the corresponding wall fuel flux increased 4–5 times. In comparison, the rich ($\phi_u = 1.5$) IW case had a dimensional maximum wall heat flux about twice those of the stoichiometric IW case and all the PW cases, while the leaner IW case ($\phi_u = 0.5$) gave a value one-fourth of the stoichiometric.

Non-dimensional FWI timescales are shown in Fig. 8 for IW and for PW at varying feed pressures. For PW they increased monotonically for increasing ϕ_u , while decreasing for IW. At rich conditions, the timescale increased with more permeation. For lean conditions, there was first a reduction to a feed pressure to 2 atm, and then an increase with further increase of permeation.

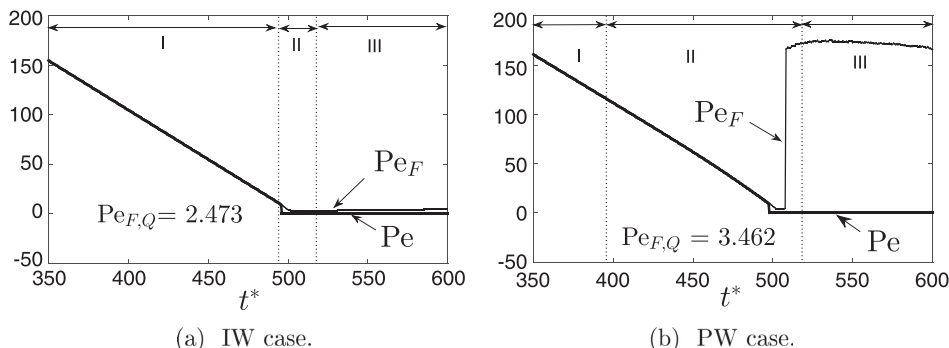


Fig. 3 – Peclet numbers versus non-dimensional time for Impermeable (a) and Permeable (b) wall configurations. The quenching values are included.

Fig. 9 displays the development of the dimensional heat release rates of PW configurations during quenching. All cases shown were for a feed pressure of 10 atm. For a short while before quenching, a two-peak behaviour of the total heat release was observed for the stoichiometric (Fig. 9a–d) and lean (Fig. 9e) cases, although not clearly in the rich case (Fig. 9f). To make the development visible in the graphs, the vertical axes were chosen such that the peaks exceeded the graphs. Therefore, the value of the peak was written into each graph. The maximum value of the overall heat release rate (which defined the quenching instance) was found at the wall ($x = 0$) in all cases.

Dilution with nitrogen and water vapour

In the following section, we investigate the influence of dilution by N_2 and H_2O of the stoichiometric premixed flame for both impermeable and permeable wall configuration. The PW cases were conducted at $p_{H_2}^f = 10$ atm.

Table 4 specifies the cases where the stoichiometric hydrogen-air mixture presented above (here denoted as Case D0) was compared to cases where more nitrogen (Cases D1 and D2) or more water vapour (Cases D3 and D4) were added. For all these cases the stoichiometric H_2 – O_2 ratio, the unburned and wall temperatures $T_u = T_w = 750$ K and (for PW)

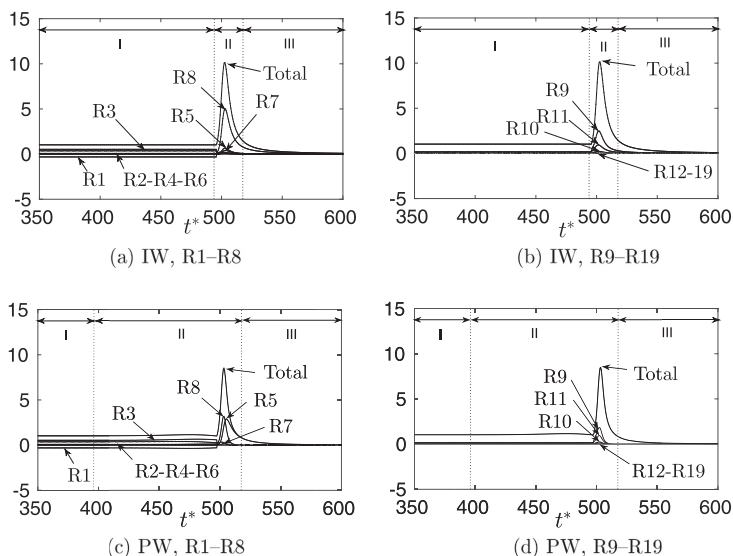


Fig. 4 – Normalized heat release rates for overall (total) and elementary reactions are shown for IW and PW configurations. The overall heat release rate of the freely propagating flame is used for normalization.

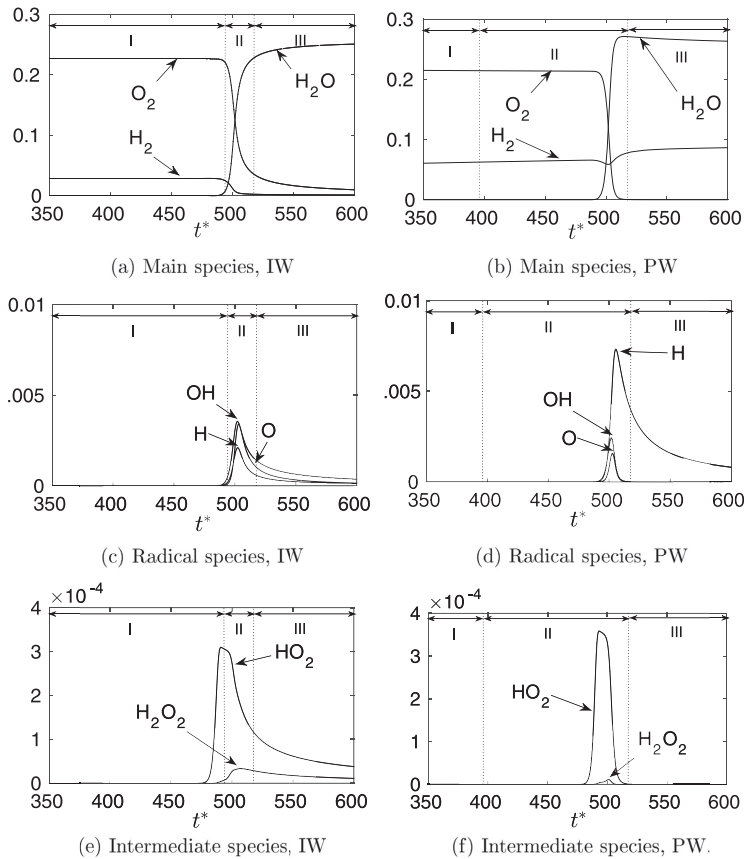


Fig. 5 – Transient profiles of species mass fractions at the wall ($x = 0$), stoichiometric conditions.

the feed pressure $p_{H_2}^f$ at 10 atm were maintained. Each case was run for both IW and PW.

The resulting non-dimensional wall heat fluxes are shown in Fig. 10. When viewing these quantities, it is worth noting that the flame properties, Table 4, also changed. For both wall configurations, the (dimensional) wall heat fluxes decreased for increasing N_2 dilution due to the lower total reaction heat release rate, $\dot{\omega}$. Reduction by 30% and 54.2% in $\dot{\omega}$ were observed for Cases D1 and D2, respectively, in comparison to Case D0. When adding H_2O , the heat release rate was reduced by 8% and 57%, respectively, for Cases D3 and D4 compared to Case D0. In these simulations, any reaction with N_2 was neglected, while H_2O participated in the reactions according to the chemical mechanism. Dilution with N_2 and H_2O delayed the flame quenching.

Effects of varying wall and unburnt mixture temperature

Simulations with reduced wall and unburnt mixture temperature are presented in this section. The isothermal boundary

condition $T_w = T_u$ (Eq. (7)) was maintained. Cases with temperatures of 300 K and 500 K, and equivalence ratios of 0.5, 1.0 and 1.5, were computed for comparison with the 750 K cases studied in Sect. 3.2. Here, $p_{H_2}^f$ was 10 atm for PW.

Non-dimensional values of wall heat and mass fluxes are shown in Fig. 11 for the IW and PW configurations at stoichiometric conditions. The quenching wall heat fluxes decreased with decreasing temperature at the wall. As for dilution, Sect. 3.4, it is worth noting the stronger reduction of the dimensional quantities compared to the non-dimensional. For PW at the lower temperature (300 K), the quenching wall heat flux was marginally higher (0.05%) compared to IW, whereas at the higher temperatures it was lower than for IW.

Results for rich and lean mixtures are shown in Fig. 12. As seen above for 750 K, the quenching wall heat fluxes of lean PW cases were significantly higher than for IW and lower for a rich mixture. In all cases, the quenching was delayed, and the wall heat flux reduced, with lower temperature.

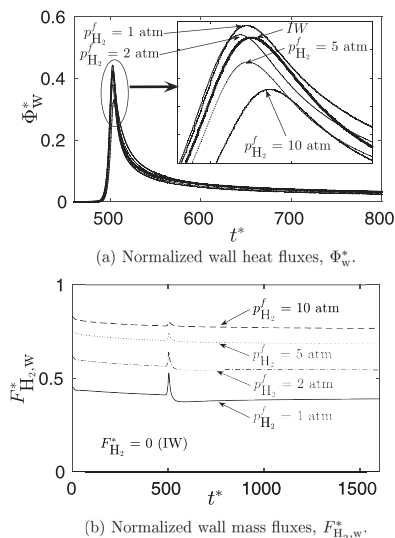


Fig. 6 – Transient wall heat fluxes (a) and mass fluxes (b) for different feed pressure ($p_{H_2}^f$) in FWI configurations at stoichiometric conditions. The IW configuration is also shown as a reference case for wall heat flux.

Discussion

Thermal radiation

Following previous work [5,7,8], thermal radiation was neglected as it was not implemented in the code used. This was based on an assumption that the influence was small and negligible due to the optically thin hydrogen flame.

As a simplified evaluation of the assumption, we did a postprocessing calculation to estimate the radiation emission, using the “optically thin flame model” [38,39]. The emitted radiation at the highest temperature was 6 orders of magnitude less than the reaction heat release. That is, for the undisturbed propagating flame. Close to the wall, the reaction heat release increased by more than one order of magnitude. For the time instances at quenching and one FWI time (cf. Fig. 8) before quenching, the reaction heat release within the flame was 5–7 orders of magnitude larger than the radiation emission. We also estimated the radiation heat transfer from the flame to the wall and found that it was 5–8 orders of magnitude less than the evaluated heat transfer to the wall (conduction, convection). Furthermore, at an emissivity approximately 0.1, the radiation from the wall would balance the radiation to the wall.

Accordingly, it could be concluded that neglecting radiation heat transfer was justified for this configuration.

Stages of head-on quenching

Results for the impermeable wall (IW) can be compared to earlier flame-wall interaction (FWI) studies performed

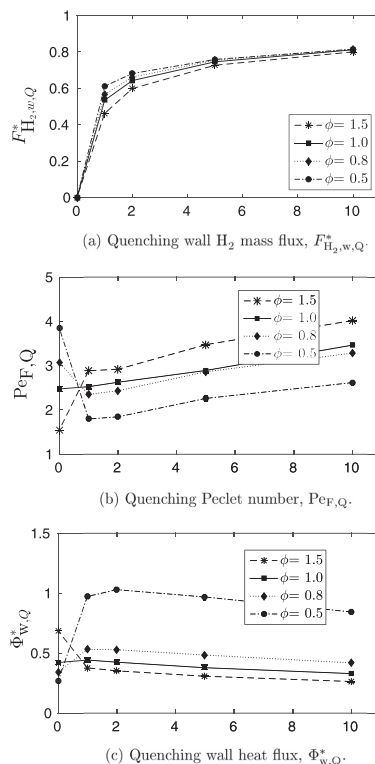


Fig. 7 – Normalized quenching mass flux, wall-flame distance and wall heat flux for varying equivalence ratio and PW feed pressures. Zero feed pressure represents the IW case.

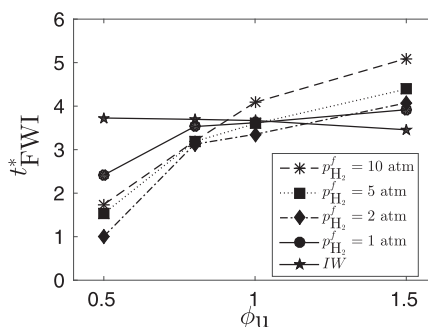


Fig. 8 – Normalized time of flame-wall interaction for varying equivalence ratio of IW and PW at different feed pressures.

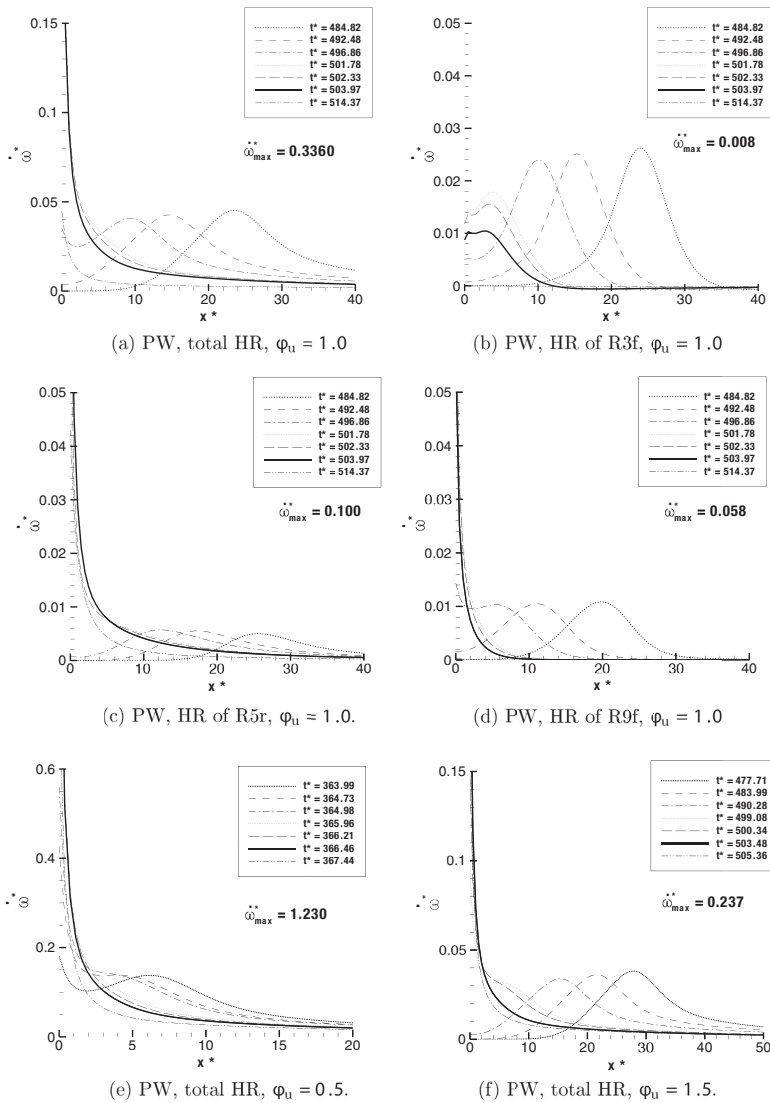


Fig. 9 – Non-dimensional heat release rates (HR), $\dot{\omega}^*$, of PW configuration, overall (total) HR and of selected individual elementary reactions. The solid lines represent the quenching instance.

for comparable conditions of hydrogen flames [5,7,14]. The main quantitative deviations can be explained by the difference between air and oxygen used as oxidizer. Some lesser differences can be attributed to differences in models (chemical mechanism, transport and thermodynamic properties) and numerical methods.

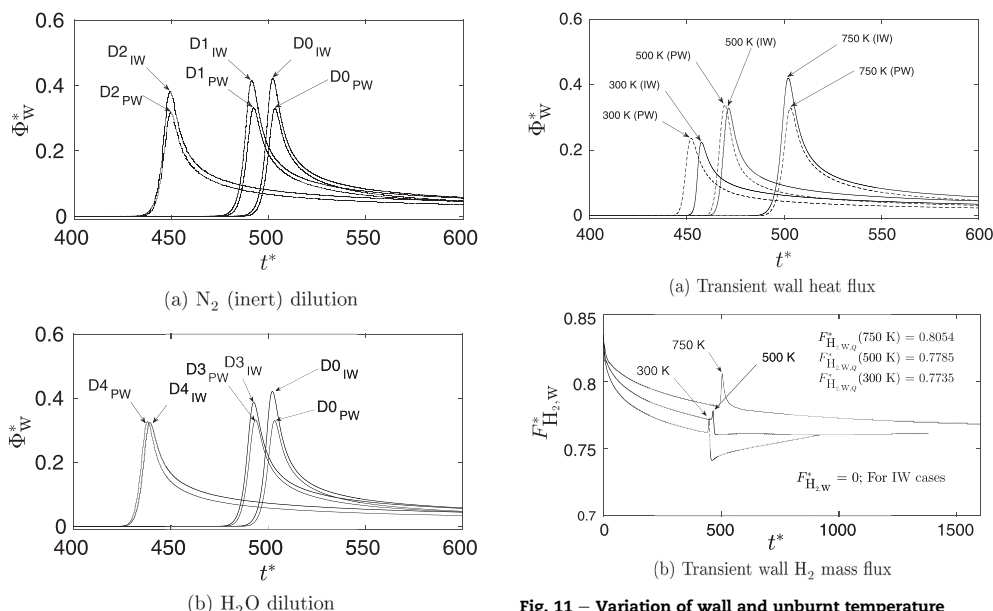
Following [5], head-on quenching can be described as a sequence of three stages to explain FWI characteristics, as

indicated in Fig. 2. The first stage is the freely propagating flame under no influence of wall effects such as wall heat flux and (for PW) wall mass flux of fuel. The transient heat release occurred within the travelling reaction zone, and the major heat release reactions were (in decreasing order) R3f, R8f, R9f, R11f and R7f, together with one major endothermic reaction, R1f.

Stage II of the IW case started at $t^* = 494.0$ with corresponding $Pe \approx Pe_F = 10.9$. Shortly after, the heat release rate $\dot{\omega}^*$

Table 4 – Inert gas and water addition to hydrogen-air mixture with wall maintained at 750 K. Case D0 is the undiluted case described above.

Case	$(N_2/O_2)_u$ [–]	$(H_2O/O_2)_u$ [–]	$(H_2O/H_2)_u$ [–]	S_L^0 [m/s]	q_i^0 [MW/m ²]	T_b [K]	(δ_L/S_L^0) [10 ^{−6} s]
D0	3.762	0.0	0.0	10.8	10.05	2597.5	1.83
D1	4.0	0.0	0.0	10.4	9.20	2511.5	11.6
D2	4.762	0.0	0.0	9.05	7.43	2383.8	60.4
D3	3.762	0.238	0.12	10.4	9.24	2499.8	10.2
D4	3.762	0.5	3.417	8.75	7.36	2343.8	73.0

**Fig. 10 – Transient wall heat fluxes for varying dilution by N_2 and H_2O in IW and PW configurations. Here $p_{H_2}^f$ is maintained at 10 atm for PW, and $T_w = T_u = 750$ K.**

began increasing and its peak reached the wall ($Pe = 0$), Fig. 3. The heat release peak reaching the wall is regarded [5] a characteristic of a “hot wall”. This instance was at $t_Q^* - t^* = 5.3$, which, independent of the initial time, can be compared to the values 6 of [5] and 3.4 of [7], both for H_2 – O_2 flames. The IW results here were in agreement with the previous studies. Towards quenching, the overall heat release rate increased tenfold due to the radical recombination reactions R8f and R9f and the chain branching R11f at the wall. Said reactions contributed 82% of the overall heat release rate at the wall.

In the PW case, the second stage started earlier than in the IW case. The initial rise of $-\dot{\omega}_F^*$ was observed at $t^* = 396.0$, with corresponding $Pe \approx Pe_F = 116$. Fuel accumulated near the wall while the flame propagated in the first stage. The flame thickness δ_L^* gradually decreased from $t^* = 403.5$, followed by an increase due to the increased ratio of fuel to O_2 . Like IW, the

Fig. 11 – Variation of wall and unburnt temperature ($T_w = T_u$) at stoichiometric conditions for IW and PW. Here, $p_{H_2}^f = 10$ atm for PW. The arrows point at the peak values.

PW flame reached the wall ($Pe = 0$) before quenching. It was noted that δ_L^* during flame quenching was approximately 1.5 times that of the IW case. Moreover, the wall heat flux was reduced to 78% of the IW case.

Fig. 4c and d presents transient heat release rates of the PW case. The maximum overall heat release rate during quenching was reduced to 82% of the IW case. This reduction can be explained by the increasingly off-stoichiometric fuel-air mixture. Furthermore, the exothermic Reaction R5r was considerably more important in PW than IW, while consuming H radicals and thereby damping the (more exothermic) H radical consuming Reaction R8f.

In the third stage the heat release and fuel consumption rates of both wall configurations decreased slowly to zero with incomplete combustion. For IW, the widening reaction zone (increasing Pe_F) after flame quenching indicated that remaining H_2 diffused towards the pool of O and OH radicals in the hot burned gas mixture to achieve post-flame

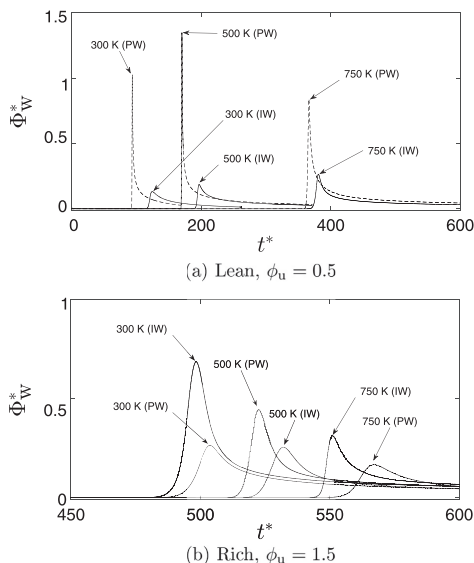


Fig. 12 – Transient wall heat fluxes for lean and rich mixtures at different wall temperatures.

oxidization. For PW, the maintained fuel influx gave rapid transport of H_2 towards the hot burned gas.

All three stages remained similar over varying permeate feed pressure of the PW and varying equivalence ratio.

Fig. 6b presents the transient non-dimensional wall mass flux ($F_{H_2,w}^*$) at stoichiometric conditions. It was observed that initially, the fuel mass flux decreased in the free propagation state. This can be explained from the accumulation of H_2 , reducing the driving force. As the flame approached the wall, from $t^* = 419$, the accumulated fuel was consumed gradually through R5f (H_2 dissociation into H) and decreasing the permeate-side partial pressure of H_2 . At quenching, the wall mass flux reached its maximum value.

Fig. 5 displays transient profiles of all species mass fractions at the wall ($x = 0$) for both IW and PW. For Stage I of IW, the composition was unaltered because the wall temperature of 750 K was insufficient to promote chain-branching reactions. The onset of changes occurred at $t^* = 494.0$ as the near-wall mixture came under influence of the flame, and the preheat zone of the flame began to lose heat to the colder wall. H_2 and O_2 were consumed at the wall in Reactions R1f, R2f, R3f and R9f with gradual accumulation of radicals. The intermediate species H_2O_2 was produced through R15r. After quenching, radicals were consumed due to recombination reactions with zero activation energy; R8f and R9f, with influence of R11f (low activation energy, chain branching).

HO_2 accumulated at the wall earlier than other species because of the radical recombination Reaction R9f (zero activation energy), which occurred in the lower-temperature region near the wall in front of the flame. It gradually reached a peak mass fraction value of $3.0 \cdot 10^{-4}$ at $t^* = 490.7$. Just after

quenching, the H_2O_2 peak mass fraction value of $3.12 \cdot 10^{-5}$ was observed at $t^* \approx 502.7$ due to the HO_2 consuming Reaction R14f. The H_2O_2 profile showed a behaviour similar to that of the overall heat release, cf [5]. The H_2O formation at the wall is due to R8f, R16f and R13f involving H and OH radicals. After $t^* = 518$, all species except H_2O declined towards zero because leftover radicals diffused from the colder wall to the hot burned gas region with production of H_2O .

In the PW case, the H_2 and O_2 mass fractions gradually changed by permeation from the beginning. As the mixture at the wall came under influence of the propagating flame, accumulated H_2 dissociated in Reaction R5f to H radicals. The HO_2 accumulation showed similarity to IW and gradually reached an early peak value of mass fraction $3.60 \cdot 10^{-4}$ at $t^* = 493.0$, while H_2O_2 reached its peak value of $1.08 \cdot 10^{-5}$ just before quenching ($t^* = 501.6$). Different from IW, these intermediates and O_2 decreased much faster for PW as permeation of hydrogen interferes with excess production of H and consumption of other radicals near the wall during flame quenching. The consumption of radicals H and OH resulting to zero was more rapid than for IW due to Reactions R2f, R4f, R12f for H and R3f for OH radicals. Furthermore, the behaviour of H_2O_2 was not similar to the overall heat release. The peak of HO_2 for PW was higher than IW due to consumption of H_2O_2 through radical recombination reactions, R17f and R18f. A peak mass fraction value of 0.271 for H_2O was observed at $t^* = 518.0$ due to R3f with consumption of OH radicals at the wall. After $t^* = 518.0$, H_2O was observed to be reduced due to absence of OH radicals at the wall.

At the wall, HO_2 was to a large extent produced through reaction R9f (as observed by Ref. [5] for IW), which is exothermic and have zero activation energy. This was also the case for PW. H_2O_2 was consumed by R15f and R19f until the flame reached the wall for IW. For PW, R15f remained the main consumer, while R19f was of low importance close to the wall.

Influence of varying feed pressure ($p_{H_2}^f$) and equivalence ratio (ϕ_u) on wall heat flux

The primary effect of fuel permeation through the wall (membrane) is to increase the local fuel-to-oxidizer ratio (local equivalence ratio) on the permeate side. The increasing feed pressure increases the fuel wall flux. Indeed, the associated increase in the permeate fuel partial pressure, will tend to reduce the mass flux according to Eq. (5). However, as seen in Fig. 7a (and more so from the corresponding graph of the dimensional quantity, not shown), this was a minor effect. The realization of the increased local equivalence ratio showed a modest dependency on that of the initial, undisturbed mixture. All the PW cases gave a locally very rich mixture close to the wall (as seen in graph of Figs. 4–6 of [17]). This can explain why the maximum wall heat flux of the PW cases had a weak sensitivity to the initial equivalence ratio (ϕ_u) compared to IW. Moreover, at a location not far from the wall, the mixture approached stoichiometric conditions. Hence, the fuel conversion rates were still large close to the wall.

The very rich IW case ($\phi_u = 4.0$) behaved in many aspects similar to the lean PW case ($\phi_u = 0.5$, 10 atm feed pressure). The (dimensional) wall heat flux at quenching for these two cases were close to each other. Also the reactions of importance for heat release were also the same, except that

Reactions R5f and R9f changed place as the 2nd and 3rd most important (after R8f).

Heat release rate trend on varying equivalence ratio (ϕ_u) in PW configurations

In both the stoichiometric (Fig. 9a) and fuel-lean (Fig. 9e) cases, a two-peak behaviour of the total heat release rate was observed near the wall. The main contributor to the peak moving towards the wall appeared to be Reaction R3f (Fig. 9b), and to some extent R9f (Fig. 9d). The peak at the wall was made by Reactions R8f, R5r (Fig. 9c), R9f and R11f until the peaks merged. On the other hand, the fuel-rich case (Fig. 9f) barely had a two-peak behaviour, as the moving peak reached the wall in about the same instance as the wall-peak was rising. For none of the cases, the described behaviour led to any two-peak temperature profile.

Influence of dilution

Increased dilution reduced the temperature of the burnt gases and, consequently, reduced the wall heat fluxes (Fig. 10). The thermal gradient alone influenced the wall heat fluxes. Additional N_2 (inert) did not influence major heat releasing reactions, however, it did reduce the total reaction heat release rate due to its increased mole fraction. Similarly, a non-diluted H_2 – O_2 premixed flame gave higher wall heat fluxes [7].

Close to the wall near quenching, dilution did not alter the relative importance of reactions. However, in the freely propagating flame, H_2O dilution caused reaction R8f to become more important for heat release than R3f.

Effects of changing wall temperature on wall heat flux

For both IW and PW configurations, the quenching wall heat fluxes (Figs. 11 and 12) increased approximately linearly with increasing wall temperature. In Fig. 11b is seen that at 300 K, after quenching, the PW wall H_2 flux dropped after quenching and then, gradually increased. This increase was caused by diffusion of H_2 away from the wall and hence, increased the pressure difference over the permeable wall (cf. Eq. (5)). Apparently, this effect has lesser impact at higher temperatures.

The radical recombination reactions R8f and R9f played the most important roles for heat release rate at the wall for all cases. Next to these, Reactions R11f and R13f were important for IW at 750 K. At lower temperatures, R11f became much less important. For PW at 750 K, Reactions R5r and R11f were the important reactions next to R8f and R9f. At 300 K, R5r had lost its role and R13f became more important than R11f in the near-wall heat release.

The accumulation of intermediate species (HO_2 and H_2O_2) was higher for both IW and PW at lower temperatures as compared to 750 K.

Conclusions

The interactions of a 1-D head-on flame with an impermeable wall (IW) and a permeable wall (PW) was investigated for

premixed hydrogen–air mixtures. Additional fuel was released through the permeable wall.

For rich and stoichiometric mixtures, PW with fuel influx gives a moderate reduction of the quenching (i.e. maximum) wall heat flux compared to IW (22% reduction was seen for stoichiometric), whereas for a lean mixture, there was a considerable increase. The maximum reaction heat release rate occurred at the wall in all cases studied. Influence of the wall on flame is felt much earlier, that is, more distant from the wall, for PW than for IW. Permeation of fuel through the wall gives a locally richer flame at the wall for PW. With a detailed chemical mechanism (Li et al. [22]) it can be seen more H radicals and less O radicals are present close to the wall for PW. The exothermic reaction recombining 2H to H_2 is considerably more important for PW. This consumption of H inhibit the more exothermic reaction of OH and H to H_2O .

Both a lower initial temperature and dilution with N_2 (inert) or H_2O (participating) reduce the burned-mixture temperature and, consequently, the wall heat flux. Also the flame propagation and quenching is delayed.

Acknowledgements

The work of the 1st author (Salimath) was partly funded by the Research Council of Norway through the project CCERT-CO₂ Capture with Enabling Research and Technology, while the work at SINTEF (Gruber) has been conducted with support from the BIGCCS Center, performed under the Norwegian research program Centres for Environmental Friendly Energy Research (FME). The authors acknowledge the following partners for their contributions: ConocoPhillips, Gassco, Shell, Statoil, Total, GDF Suez and the Research Council of Norway (193816/S60). We are grateful to the Norwegian Metacenter for Computational Science (NOTUR) for providing the HPC computational resources and useful technical support.

Appendix A. Comparison with Chemkin calculations

The flame properties above were obtained from a freely propagating flame by S3D [19]. Since the Chemkin code is widely used to produce such properties, a comparison was made by using the Chemkin library [31,32]. The chemical mechanism and specific heats were identical. For the variation of ϕ_u from 0.5 to 1.5, the Chemkin results gave a 4–2% lower ($T_b - T_u$), a 9–5% higher S^0_{298} and a 7–4% lower δ_L compared to S3D. There are some differences in the algorithms and numerical setups used in these two options, which can explain the deviations.

Fig. A13 shows the mass-fraction profiles for the stoichiometric flame for both codes. The abscissa x' is the distance from the point of the maximum temperature gradient, non-dimensionalized by the thermal flame thickness δ^0_L . The S3D results were taken at a the instance of 0.65 times the quenching time.

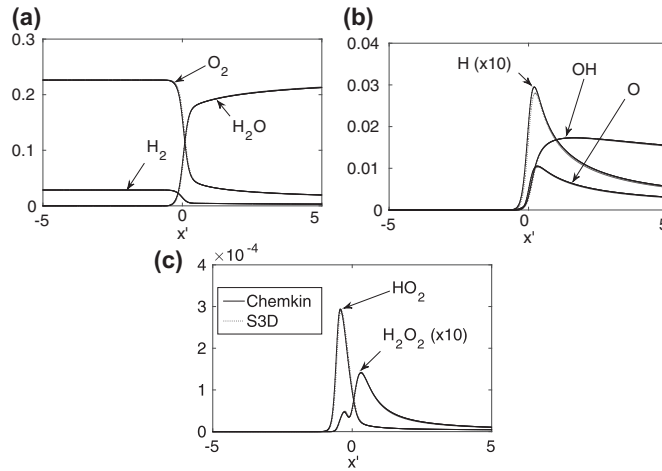


Fig. A13 – Species mass fractions of the freely propagating flame. Comparison of results of the Chemkin library and of S3D.

Nomenclature

Abbreviations

IW	Impermeable wall
PW	Permeable wall

Greek symbols

δ_L^0	Flame thickness m
δ_L	Characteristic flame thickness m
$\dot{\omega}$	Overall reaction heat release rate W/m ³
$\dot{\omega}_k$	Molar production rate of species k kg/(m ³ s)
λ	Thermal conductivity of the gaseous mixture W/(mK)
Φ	Heat flux W/m ²
ϕ	Equivalence ratio
ρ	Density kg/m ³
T	Viscous stress tensor N/m ²

Latin symbols

Pe	Peclet number based on location of $\dot{\omega}_{\max}$
Pe _F	Peclet number based on location of $-\dot{\omega}_F, \max$
C_p	Specific heat at constant pressure J/(kgK)
D	Mass diffusivity m ² /s
e_0	Specific total energy J/kg ⁻¹
F_k	Mass flux of species k kg/(m ² s)
L	Length of domain m
m	Parameter (exponent) for heat flux estimation
n	Pressure exponent of membrane
N_g	Number of species
N_r	Number of reactions
p	Pressure Pa
q_L^0	Flame power W/m ²
S_L^0	Laminar flame speed m/s ⁻¹
T	Temperature K
t	Time s
u	Velocity ms ⁻¹

V_k	Mass diffusion velocity of species k ms ⁻¹
W_k	Molecular weight of species k kg/kmol
x	Spatial coordinate m
X_k	Mole fraction of species k
y	Wall-flame distance m
Y_k	Mass fraction of species k

Superscripts

o	Free propagating state
f	Feed side
p	Permeate side

Subscripts

'	Non-dimensional values
*	Non-dimensional values
α, β	Directional indices
b	Burnt mixture
FWI	Flame wall interaction
F	Fuel
max	Maximum value
mix	Mixture average
Q	Quenching
u	Unburnt mixture
w	Wall
k	Species index

REFERENCES

- [1] Westbrook CK, Adamczyk AA, Lavoie GA. A numerical study of laminar flame wall quenching. *Combust Flame* 1981;40:81–99.
- [2] Wichman IS, Bruneaux G. Head-on quenching of a premixed flame by a cold wall. *Combust Flame* 1995;103(4):296–310.

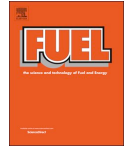
- [3] Gruber A, Sankaran R, Hawkes ER, Chen JH. Turbulent flame wall interaction: a direct numerical simulation study. *J Fluid Mech* 2010;658:5–32.
- [4] Ezekoye OA, Greif R, Sawyer RF. Increased surface temperature effects on wall heat transfer during unsteady flame quenching. *Symp Combust* 1992;24(1):1465–72.
- [5] Dabireau F, Cuenot B, Vermorel O, Poinso TJ. Interaction of flames of $H_2 + O_2$ with inert walls. *Combust Flame* 2003;135(1–2):123–33.
- [6] Popp P, Baum M. Analysis of wall heat fluxes, reaction mechanisms, and unburnt hydrocarbons during the head-on quenching of a laminar methane flame. *Combust Flame* 1997;108(3):327–48.
- [7] Owston R, Magi V, Abraham J. Interactions of hydrogen flames with walls: influence of wall temperature, pressure, equivalence ratio, and diluents. *Int J Hydrogen Energy* 2007;32(12):2094–104.
- [8] Mari R, Cuenot B, Rocchi J-P, Selle L, Duchaine F. Effect of pressure on hydrogen/oxygen coupled flame wall interaction. *Combust Flame* 2016;168:409–19.
- [9] Boust B, Sotton J, Labuda SA, Bellenoue M. A thermal formulation for single-wall quenching of transient laminar flames. *Combust Flame* 2007;149(3):286–94.
- [10] Dreizler A, Böhm B. Advanced laser diagnostics for an improved understanding of premixed flame-wall interactions. *Proc Combust Inst* 2015;35(1):37–64.
- [11] Lu JH, Ezekoye OA, Greif R, Sawyer RF. Unsteady heat transfer during side wall quenching of a laminar flame. *Symp Combust* 1991;23(1):441–6.
- [12] Vosen S, Greif R, Westbrook C. Unsteady heat transfer during laminar flame quenching. *Symp Combust* 1985;20(1):75–83.
- [13] Sotton J, Boust B, Labuda SA, Bellenoue M. Head-on quenching of transient laminar flame: heat flux and quenching distance measurements. *Combust Sci Technol* 2005;177(7):1305–22.
- [14] Poinso T, Veynante D. Theoretical and numerical combustion. R.T. Edwards, Inc; 2005.
- [15] Huang WM, Vosen SR, Greif R. Heat transfer during laminar flame quenching: effect of fuels. *Symp. Combust* 1988;21(1):1853–60.
- [16] Gruber A, Chen JH, Valiev D, Law CK. Direct numerical simulation of premixed flame boundary layer flashback in turbulent channel flow. *J Fluid Mech* 2012;709:516–42.
- [17] Gruber A, Salimath PS, Chen JH. Direct numerical simulation of laminar flame-wall interaction for a novel H_2 -selective membrane/injector configuration. *Int J Hydrogen Energy* 2014;39(11):5906–18.
- [18] Jordal K, Anantharaman R, Gruber A, Peters T, Henriksen PP, Berstad D, et al. Performance of the IGCC with distributed feeding of H_2 in the gas turbine burner. *Energy Procedia* 2014;63:2037–44.
- [19] Chen JH, Choudhary A, de Supinski B, DeVries M, Hawkes ER, Klasky S, et al. Terascale direct numerical simulations of turbulent combustion using S3D. *Comput Sci Discov* 2009;2(1):15001.
- [20] Bredesen R, Jordal K, Bolland O. High-temperature membranes in power generation with CO_2 capture. *Chem Eng Process Process Intensif* 2004;43(9):1129–58.
- [21] Vadrucci M, Borgognoni F, Moriani A, Santucci A, Tosti S. Hydrogen permeation through Pd-Ag membranes: surface effects and Sieverts' law. *Int J Hydrogen Energy* 2013;38(10):4144–52.
- [22] Li J, Zhao Z, Kazakov A, Dryer FL. An updated comprehensive kinetic model of hydrogen combustion. *Int J Chem Kinet* 2004;36(10):566–75.
- [23] Chen JH. Peta-scale direct numerical simulation of turbulent combustion - fundamental insights towards predictive models. *Proc Combust Inst* 2011;33(1):99–123.
- [24] Sankaran R, Hawkes ER, Chen JH, Lu TF, Law CK. Direct numerical simulations of turbulent lean premixed combustion. *J Phys Conf Series* 2006;46(1):38–42.
- [25] Grout RW, Gruber A, Yoo CS, Chen JH. Direct numerical simulation of flame stabilization downstream of a transverse fuel jet in cross-flow. *Proc Combust Inst* 2011;33(1):1629–37.
- [26] Hawkes ER, Sankaran R, Sutherland JC, Chen JH. Scalar mixing in DNS of temporally-evolving plane jet flames with detailed CO/H_2 kinetics. *Proc Combust Inst* 2007;31(1):1633–40.
- [27] Lignell DO, Chen JH, Smith PJ, Lu T, Law CK. The effect of flame structure on soot formation and transport in turbulent nonpremixed flames using direct numerical simulation. *Combust Flame* 2007;151(1–2):2–28.
- [28] Sankaran R, Im HG, Hawkes ER, Chen JH. The effects of non-uniform temperature distribution on the ignition of a lean homogeneous hydrogen-air mixture. *Proc Combust Inst* 2005;30(1):875–82.
- [29] Echehki T, Chen JH. Direct numerical simulation of auto-ignition in non-homogeneous hydrogen-air mixtures. *Combust Flame* 2003;134(3):169–91.
- [30] Kennedy CA, Carpenter MH. Several new numerical methods for compressible shear layer simulations. *Appl Numer Math* 1994;14(804):397.
- [31] Kee RJ, Rupley FM, Miller JA. CHEMKIN-II: a FORTRAN chemical kinetics package for the analysis of gas phase chemical kinetics. SANDIA Rep. No. SAND89-8009B 1989:3–164.
- [32] Kee RJ, Dixon LG, Warnatz J, Coltrin ME, Miller JA, Moffat HK. A fortran chemical kinetics package for the analysis of gas-phase chemical kinetics., Tech. Rep., Release 3.5. San Diego, CA: Reaction Design Inc.; 1999.
- [33] Gustafsson B, Sundström A. Incompletely parabolic problems in fluid dynamics. *SIAM J Appl Math* 1978;35(2):343–57.
- [34] Nordström J, Svård M. Well-posed boundary conditions for the Navier–Stokes equations. *SIAM J Numer Anal* 2005;43(3):1231–55.
- [35] Strikwerda JC. Initial boundary value problems for incompletely parabolic systems. *Commun Pure Appl Math* 1977;30(6):797–822.
- [36] Yoo C, Wang Y, Troune A, Im H. Characteristic boundary conditions for direct simulations of reacting counterflow. *Combust Theory Model* 2005;9(1):617–46.
- [37] Yoo CS, Im HG. Characteristic boundary conditions for simulations of compressible reacting flows with multi-dimensional, viscous and reaction effects. *Combust Theory Model* 2007;11(2):259–86.
- [38] Radiation Models. URL, <http://www.sandia.gov/TNF/radiation.html>. [Accessed 25 November 2017].
- [39] Barlow R, Smith NSA, Chen J-Y, Bilger RW. Nitric oxide formation in dilute hydrogen jet flames: isolation of the effects of radiation and turbulence-chemistry submodels. *Combust Flame* 1999;117:4–31.

Article 3

**Computational analysis of premixed methane-air flame interacting
with a solid wall or a hydrogen porous wall**

Prashant S. Salimath, Ivar S. Ertesvåg, Andrea Gruber

Published in Fuel



Computational analysis of premixed methane-air flame interacting with a solid wall or a hydrogen porous wall

Prashant S. Salimath^{a,*}, Ivar S. Ertesvåg^{a,*}, Andrea Gruber^{a,b}

^a Department of Energy and Process Engineering, NTNU Norwegian University of Science and Technology, Kolbjørn Hejes vei 1b, NO-7491 Trondheim, Norway

^b SINTEF Energy Research, Trondheim, Norway

ARTICLE INFO

Keywords:

Impermeable wall
Permeable wall
S3D code
Head on quenching
Smooke and Giovangigli mechanism
DRM22 mechanism

ABSTRACT

The process of flame-wall interaction for premixed methane-air flames is investigated by direct numerical simulation. The flames propagate towards an isothermal, chemically inert surface, consisting of either a solid impermeable wall (IW) material or a hydrogen-permeable wall (PW) material. With the PW, hydrogen seeps into the domain and participate as a secondary, non-premixed fuel. The skeletal methane-air chemical reaction kinetics mechanisms of Smooke and Giovangigli and DRM22 are used with the S3D code to study the major reactions controlling the flame-wall interactions (FWI). Initially, results of said mechanisms are compared to the complete GRI 3.0 scheme. The configurations are investigated for two temperatures, 600 K and 750 K, of the wall and the unburnt gas, and for initial equivalence ratios of 0.5, 1.0 and 1.5. Results for IW are similar to previous FWI studies. The flame quenches at the wall, with maximum heat release and wall heat flux occurring close to the quenching instance. For the PW cases, the flame quenches before reaching the wall. This is explained by the mutual effects of convective heat transfer away from the wall and flame due to permeation, a high concentration of hydrogen and high local fuel-to-oxidizer ratio, reduced temperature and reduced reaction heat release. The quenching definition and flame position are based on OH radicals concentration. The observed maximum wall heat flux is much lower than for IW, and occurs some time after quenching. A discussion about the quenching process indicates that a definition based on maximum wall heat flux is inappropriate.

1. Introduction

Recent efforts towards low-emission and sustainable solutions for power and transport, paired with increasingly high power densities, necessarily imply that industrial combustion devices will be subject to more restrictive emissions and efficiency standards and, simultaneously, to intense reaction taking place closer to the combustion chamber walls. Large efficiency losses and pollutants formation in combustion devices take place in flame-wall interactions (FWI) that occur when the flame is quenched in the immediate vicinity of a solid surface [1,2]. However, in spite of their practical relevance, detailed physical insights about FWI processes have been difficult to extract from laboratory experiments, due to important challenges in performing accurate near-wall measurements. In this context, accurate state-of-the-art direct numerical simulation (DNS) remains an important tool in fundamental investigations of FWI processes [3–5].

The premixed FWI process is described as a freely propagating flame moving towards a (relatively) cold wall such that the flame quenches in the near-wall region due to thermal loss from the reaction zone to the

wall. Accurate estimation of the quenching distance is important as it determines the unburnt layer subject to strong near-wall thermal gradients in energy conversion devices such as gas turbines and reciprocating engines. The present trend in engine downsizing increases the surface to volume ratio, with profound effects on near-wall combustion and pollutants formation. Previous numerical and experimental work on premixed FWI have investigated different parameters such as wall temperature, equivalence ratio, constant volume/pressure chambers and surface reactivity for hydrocarbon fuels [6–16] and for hydrogen [17–19,3,20]. In a comprehensive review, Dreizler and Böhm [2] summarized recent advancement and gave a detailed discussion on FWI, including methods for accurate quenching distance determination based on laser diagnostics and direct numerical simulations.

Typical numerical investigations of FWI phenomena are performed in canonical configuration setups of 1-dimensional head-on quenching (HOQ) and 2-d side-wall quenching. Transient 1-d HOQ is considered as an extreme case of FWI, with zero flame stretch and large thermal losses to the wall. Quenching distance, wall thermal transfer and exhaust composition are key parameters of 1-d FWI. These parameters depend

* Corresponding author.

E-mail addresses: Prashant.Salimath@ntnu.no (P.S. Salimath), Ivar.S.Ertesvag@ntnu.no (I.S. Ertesvåg), Andrea.Gruber@sintef.no (A. Gruber).

<https://doi.org/10.1016/j.fuel.2020.117658>

Received 8 December 2019; Received in revised form 12 March 2020; Accepted 17 March 2020

0016-2361/ © 2020 The Authors. Published by Elsevier Ltd. This is an open access article under the CC BY license (<http://creativecommons.org/licenses/by/4.0/>).

Nomenclature		p	Pressure, Pa
Abbreviations		q_f^0	Flame power, W/m ²
IW Impermeable wall		S_L^0	Laminar flame speed, m s ⁻¹
PW Permeable wall		T	Temperature, K
Greek symbols		t	Time, s
δ_L^0	Flame thickness, m	u	Velocity, m s ⁻¹
δ_L	Characteristic flame thickness, m	W_k	Molar mass of species k , kg/kmol
$\dot{\omega}$	Overall reaction heat release rate, W/m ³	x	Spatial coordinate, m
$\dot{\omega}_k$	Molar production rate of species k , kg/(m ³ s)	y	Wall-flame distance, m
λ	Thermal conductivity of the gaseous mixture, W/(mK)	Y_k	Mass fraction of species k , –
Φ	Heat flux, W/m ²	Superscripts	
ϕ	Equivalence ratio, –	f	Feed side
ρ	Density, kg/m ³	p	Permeate side
Latin symbols		Subscripts	
Pe	Peclet number based on location of $\dot{\omega}_{\max}$, –	'	Non-dimensional values
Pe _F	Peclet number based on location of $-\dot{\omega}_{F,\max}$, –	*	Non-dimensional values
Pe _{OH*}	Peclet number based on location of maximum OH gradient, –	b	Burnt mixture
C_p	Specific heat at constant pressure, J/(kgK)	F	Fuel
D	Mass diffusivity, m ² /s	max	Maximum value
F_k	Mass flux of species k , kg/(m ² s)	mix	Mixture average
L	Length of domain, m	Q	Quenching
M	Number of nodes within flame thickness at quenching, –	u	Unburnt mixture
n	Pressure exponent of membrane, –	w	Wall
		k	Species index

on stoichiometry, wall and unburnt-gas temperatures and pressure. A higher pressure leads to decrease of quenching distance, while the FWI time remains unchanged [21]. In simulations using detailed chemical mechanisms for 1-d HOQ of laminar flames at constant pressure and stoichiometric conditions, increased wall temperature led to a significant increase of the wall thermal flux for methane [15,10], n-heptane [12] and iso-octane [7] mixtures with air.

State-of-the-art numerical simulations of FWI have typically employed detailed chemical mechanisms. Single-step and simplified chemical models showed good results of wall heat flux compared to experimental results for lower wall temperatures, around 300 K, for different equivalence ratios [22,14,16]. However, they failed for higher wall temperatures due to presence of low-activation radical recombination reactions near the wall [14]. When detailed chemical mechanisms were included, good FWI results in comparison to experimental data were achieved for wall temperatures above 400 K [10]. For 1-d HOQ configurations for both methane and hydrogen flames at elevated wall temperatures, exothermic radical recombination reactions and intermediate species contributed to large heat release at the

wall during quenching [10,3,17]. Recently, complex chemistry models were used for acoustics due to flame annihilation in FWI. In the case of noise generation in 1-d HOQ at a wall of temperature 300 K, simple chemistry led to a faster extinction process and overestimating of pressure peaks during quenching compared to the detailed chemistry [23].

FWI involving hydrocarbon fuels for impermeable, inert-wall configurations showed inverse proportional relationships of normalized wall heat flux and flame quenching distance (i.e. quenching Peclet number). Boust et al. [11] developed modelling relationships between quenching distance and wall heat flux in 1-d HOQ for methane flames. These relationships do not hold true for hydrogen flames, as higher wall fluxes are observed with flame diffusing faster and reaching closer to the wall [17].

Recently, renewed interest in hydrogen selective membranes, in the context of carbon capture and storage (CCS) applications, has raised the issue of flame-wall interactions in the presence of a porous, permeable wall that can act as a source of hydrogen fuel. In two previous studies the present authors presented numerical investigations on the effects of

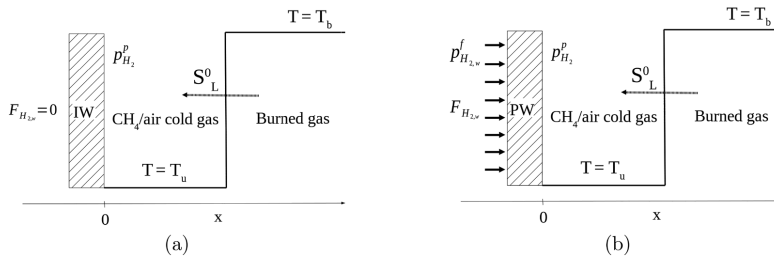


Fig. 1. Head-on quenching configurations of (a) Impermeable wall (IW) and (b) Permeable wall (PW) with hydrogen flux.

Table 1

Chemical mechanism by Smooke and Giovangigli [35] with rate coefficients $k_f = AT^b \exp(-E_0/RT)$.

No.	Reaction	A	β	E_0
R1	$H + O_2 \rightarrow OH + O$	2.00E+14	0.0	16800.0
R2	$O + H_2 \rightarrow OH + H$	1.80E+10	1.0	8826.0
R3	$H_2 + OH \rightarrow H_2O + H$	1.17E+09	1.30	3626.0
R4	$OH + OH \rightarrow O + H_2O$	6.00E+08	1.300	0.0
R5	$H + O_2 + M \rightarrow HO_2 + M$	2.30E+18	-0.80	0.0
R6	$H + HO_2 \rightarrow OH + OH$	1.50E+14	0.000	1900.0
R7	$H + HO_2 \rightarrow H_2 + O_2$	2.50E+13	0.0	700.0
R8	$OH + HO_2 \rightarrow H_2O + O_2$	2.00E+13	0.0	1000.0
R9	$CO + OH \rightarrow CO_2 + H$	1.51E+07	1.30	-758.0
R10	$CH_4 + (M) \rightarrow CH_3 + H + (M)$	2.30E+38	-7.0	114363.0
R11	$CH_4 + H \rightarrow CH_3 + H_2$	2.20E+04	3.0	8750.0
R12	$CH_4 + OH \rightarrow CH_3 + H_2O$	1.60E+06	2.10	2460.0
R13	$CH_3 + O \rightarrow CH_3O + H$	6.80E+13	0.0	0.0
R14	$CH_2O + H \rightarrow HCO + H_2$	2.50E+14	0.0	10500.0
R15	$CH_2O + OH \rightarrow HCO + H_2O$	3.00E+13	0.0	167.0
R16	$HCO + H \rightarrow CO + H_2$	4.00E+13	0.0	0.0
R17	$HCO + M \rightarrow CO + H + M$	1.60E+14	0.0	14700.0
R18	$CH_3 + O_2 \rightarrow CH_3O + O$	7.00E+12	0.0	25652.0
R19	$CH_3O + H \rightarrow CH_3OH + H_2$	2.00E+13	0.0	0.0
R20	$CH_3O + M \rightarrow CH_3OH + M$	2.40E+13	0.0	28812.0
R21	$HO_2 + HO_2 \rightarrow H_2O_2 + O_2$	2.00E+12	0.0	0.0
R22	$H_2O_2 + M \rightarrow 2OH + M$	1.30E+17	0.0	45500.0
R23	$H_2O_2 + OH \rightarrow H_2O + HO_2$	1.00E+13	0.0	1800.0
R24	$OH + H + M \rightarrow H_2O + M$	2.20E+22	-2.0	0.0
R25	$H + H + M \rightarrow H_2 + M$	1.80E+18	-1.0	0.0

an H_2 flux through a permeable wall into an H_2 -air mixture and influence on the FWI heat fluxes: Gruber et al. [4] presented 1-d and 2-d FWI results for a high pressure of 10 atm at the permeate side and showed that a strong feedback mechanism exists between the permeating hydrogen flux and the flame. Salimath et al. [5] extended the study on the 1-d solid-wall and permeable-wall configurations and presented FWI results for different feed pressures, dilution with N_2 (inert) and H_2O (participating) and different wall temperatures. Furthermore, a recent experimental study has investigated the effects on premixed flame shape and stabilization of a novel approach for spatially distributed hydrogen injection through a porous steel surface integrated in the burner design [24].

Fig. 1 illustrates schematically the 1-d case of a planar flame front propagating through initially premixed methane-air and impinging upon a solid wall. This flame quenching process is shown for an impermeable wall (IW) or solid wall and a fuel-permeable wall (PW). In the PW case, high pressure at the feed side supplies H_2 as a secondary fuel into the domain. Hence, the flame becomes partially premixed on the permeate side.

The present study is an investigation of the configuration with methane-air mixtures and a selective H_2 porous wall at wall temperatures of 600 and 750 K. The hydrogen flux through the membrane influences the near-wall chemistry and wall heat transfer. We will investigate detailed FWI characteristics and influence of hydrogen influx on heat release rates near the wall for lean, stoichiometric and rich methane-air mixtures. The contributions of individual elementary reactions will be studied more in detail. This study aims at gaining understanding of near-wall chemistry and influence of hydrogen permeability in hardware components on quenching wall heat fluxes. The permeating secondary fuel can alter the local chemistry for a given mixture. The practical arrangement and implementation of permeability of H_2 fuel was outside the scope of this study, and no effort was made to show experimental setup of permeability of wall.

In the following, Section 2 describes the code, numerical setup, submodels and boundary conditions, and relevant quantities are defined. The flame-wall interaction results are presented in Section 3 and discussed in Section 4. Finally, conclusions are presented.

2. Numerical setup and submodels

2.1. Code, numerics and thermo-fluid models

The massively parallel DNS code, S3D, developed at Sandia National Laboratories [25], was used here for the 1-d FWI studies. The code handles inter-process communication in parallel execution through Message Passing Interface (MPI) [26]. It has been ported to different architectures for a variety of case studies [27,3,28–32]. It solves the conservative form of Navier-Stokes equations on structured, Cartesian grids in 1–3 spatial directions.

The numerical solver of the code employs a high order, non-dissipative central difference scheme. A spatial tenth-order explicit filter is employed at every 10 iterations to remove any spurious high frequency noise in the simulations resulting from aliasing errors and odd-even decoupling. An eight-order explicit central difference scheme is used within the computational domain, while a third order scheme (one sided stencils) at boundaries. A six-stage fourth-order explicit Runge-Kutta method is used in time [33].

Details of the governing equations and constitutive relationships, such as ideal gas equation of state, models for reaction rates, molecular transport and thermodynamic properties were described by Chen et al. [25] and hence, are only briefly mentioned here. The Soret effect (thermo-diffusion) and pressure diffusion were included, whereas the Dufour effect was not implemented in the code [25]. Body-force effects (gravity) and radiation heat transfer were neglected, following several previous premixed-flame studies of methane [14,16,23,10,34] and hydrogen flames [17,12,18,4]. The walls were assumed as chemically inert, with no adsorption or catalytic effects.

2.2. Chemical mechanisms

Chemistry was modelled by three different mechanisms: Reduced chemistry of methane-air combustion was described by Smooke and Giovangigli [35] (SG in the following). This 25-step mechanism includes 16 species: H_2 , H , O , O_2 , OH , H_2O , HO_2 , CH_4 , CO , CO_2 , H_2O_2 , CH_3 , HCO , CH_2O , CH_3O and N_2 . Table 1 lists the 25 elementary reactions enumerated as R1 to R25, with reaction rate coefficients. This mechanism contains C1 chemistry, however not C2 or higher C compounds. Similar to [34], but deviating from the original source [35], all reverse reactions were included, and their coefficients determined from the equilibrium constants. It should also be noted that the coefficients of Table 1 are as used by [34], which deviated in R6, R14, R15, while R10 was found in the text (not the table) of [35]. Some trials were made with the original version, denoted “SG(orig)”, where all coefficients are taken from “Table II” of [35]. For rich mixtures, the DRM22 mechanism [36] was used. This is a reduced version of GRI 1.2, consisting of 24 species (including inert Ar and N_2) and 104 reversible reactions. DRM22 showed good laminar flame speed predictions in rich flames at 1 atm [36]. Compared to SG, the six additional species are CH_2 , C_2H_2 , C_2H_3 , C_2H_5 , C_2H_6 and Ar.

The full GRI 3.0 mechanism [37] comprised 53 species (including Ar) and 325 reversible reactions of methane oxidation with extensive NO_x chemistry.

The Chemkin and Transport software libraries [38,39] related to chemical mechanism were linked to S3D to provide thermodynamic properties and mixture-averaged transport properties to the solver.

2.3. Hydrogen flux formulation and wall boundary conditions

The membrane hydrogen flux was based Sieverts’ law and expressed as

$$F_{H_2,w} = Q'' \cdot W_{H_2} \left((p_{H_2}^f)^n - (p_{H_2}^b)^n \right), \quad (1)$$

where Q'' is the membrane permeance factor and n is the pressure

exponent. For typical 2–3 μm Pd-based membranes, these were set to $Q^* = 7.0 \cdot 10^{-6} \text{ kmol}/(\text{m}^2 \text{sPa}^{0.5})$ and $n = 0.5$ [40,4]. The wall boundary conditions are well-posed to 1-d domains for IW and PW configurations [41–43]. The temperature and species gradients were set to zero, except for H_2 at the permeable wall, which was determined as

$$\left(\frac{\partial Y_{\text{H}_2}}{\partial x} \right)_w = \frac{F_{\text{H}_2,w}}{\rho_w D_{\text{mix},w}} \quad (2)$$

More details of the wall boundary conditions implementation were given in [4,5].

The outlet was treated as non-reflective boundary based on Navier-Stokes Characteristic Boundary conditions (NSCBC) [44,45].

2.4. Definitions of FWI quantities

Flame quenching was defined as the instance where the normalized maximum OH gradient (here denoted OH^*) falls or reaches below 0.5. For normalization, the value of the free propagating flame was used. This definition was adopted from laser diagnostics [46,47], where the OH molecule is used to detect the flame front.

The premixed flame position was tracked by three different alternative locations, viz. those of the maximum OH gradient (OH^*), the maximum heat release rate ($\dot{\omega}_{\text{max}}^*$) and the maximum fuel consumption rate ($-\dot{\omega}_{\text{F,max}}^*$). The corresponding flame-wall distances yielded three non-dimensional Peclet numbers.

In a freely propagating flame, the laminar flame speed S_L^0 , characteristic flame thickness $\delta_L = \lambda_u/(\rho_u C_{p,u} S_L^0)$, laminar flame power $q_l^0 = \rho_u C_{p,u} S_L^0 (T_b - T_u)$ and thermal flame thickness, $\delta_L^0 = (T_b - T_u)/(\partial T/\partial x)_{\text{max}}$, were computed [17,19,1]. The burnt gas temperature T_b was computed as the adiabatic flame temperature for equilibrium at constant pressure. The properties ρ_u , λ_u and $C_{p,u}$ were evaluated at the unburnt gas temperature and initial gas composition.

In the PW cases, the normalizing term for mass flux was $F_{\text{H}_2\text{max}}$, which is the maximum wall mass flux evaluated (Eq. 1) for a zero hydrogen partial pressure on the permeate side.

Table 2 lists dimensional quantities and defines the corresponding non-dimensional variables.

2.5. Computational setup and description of cases

The 1-d domain of the head-on quenching setup (Fig. 1) had a total length of $L = 0.02 \text{ m}$. The grid with uniform mesh had $N = 9984$ nodes, which gave a spatial resolution of $\Delta x = 2.0 \cdot 10^{-6} \text{ m}$. These values were chosen in order to capture the flame during quenching. The time step was fixed at $0.5 \cdot 10^{-9} \text{ s}$ for all simulations. This short time step was due to small chemical time scales for detailed chemistry and acoustics CFL condition. All numerical simulations were distributed on 32 processors.

The freely propagating CH_4 -air flame profile generated by Chemkin premix [39] provided the initial field for the S3D code. It was placed in the center of the 1-d domain, i.e. at $x = 0.01 \text{ m}$, at initial time $t = 0 \text{ s}$. The initial velocities were set to zero for all cases. The air was assumed as 79% N_2 and 21% O_2 , molar based. The pressure of the gas mixture was maintained at 1 atm. All cases were specified with equal wall and unburnt-gas temperature, $T_w = T_u$. The values were 600 K and 750 K. The equivalence ratio was varied as 0.5 (lean), 1.0 (stoichiometric) and 1.5 (rich). These values applied to the initial mixture, unaffected by H_2 influx in the PW cases.

The PW cases had constant feed-side pressure, $p_{\text{H}_2}^f = 10.0 \text{ atm}$, and H_2 permeation occurred from the start of simulation, $t = 0$.

Flame properties for a freely propagating flame were obtained by S3D. Since the Chemkin code is widely used to produce such properties, a comparison was made by using the Chemkin library [38,39] with identical chemical mechanism and specific heats.

The cases with chosen parameters and mechanisms will be specified below, together with the overview of key results in Section 3.1.

The numerical results for the PW configuration were compared against the IW configurations for validation due to lack of experiments, while the results of IW configurations were compared to previous one-dimensional flame quenching of methane premixed flames [10,23].

3. Results

3.1. Overview of cases

Table 3 presents different numerical cases performed. The lean and stoichiometric cases were obtained with the SG mechanism, while the rich cases with DRM22. The spatial resolution was chosen such that the FWI results were independent of mesh size. The number of nodes was maintained at $N = 9984$ for all computations. The number of nodes falling within the flame thermal thickness at quenching, M , was evaluated. It was made sure that this number was at least 40, while 10 points have been regarded as a minimum requirement [3].

3.2. Validation of flame setup and chemical mechanisms

The initialization method for the 1-d transient process was described in Section 2.5, and it yielded marginally deviating flow fields during the flame set-up. Some initial spurious oscillations were observed due to the incorrect velocity field imposed from Chemkin results. Within a short transitional time, the flame re-adjusted within the unburnt mixture and propagated at a nearly constant laminar flame speed (S_L^0) until sensing the presence of the impermeable wall (IW cases) or enriched hydrogen fuel concentration (PW). The short period of incorrect velocity field was ignored for analysis and should have no influence on the final FWI results.

Fig. 2 presents a comparison of basic flame characteristics profiles for Chemkin and S3D after the initialization period. Fig. 2a compares Chemkin profiles of the SG and GRI mechanisms. The profiles from Chemkin are compared to the initialized profiles from S3D in Fig. 2b (SG) and Fig. 2c (GRI). These runs were made for a stoichiometric mixture at 750 K. The S3D results for IW were extracted at 0.55 and 0.39 times the quenching time for SG and GRI, respectively. In the graphs, the abscissa was non-dimensionalized as $(x - x_0)/\delta_L^0$, where x_0 is the location of maximum thermal gradient. Good agreement were observed for the comparisons. Small deviations were observed between the different chemistries, while Chemkin and S3D profiles were virtually identical.

To validate FWI results from the reduced mechanisms (SG, DRM22), some IW cases were computed with GRI 3.0. These were conducted for a temperature of wall and unburnt gas ($T_w = T_u$) at 750 K and equivalence ratios ϕ_u of 0.5, 1.0 and 1.5. This high temperature was chosen to

Table 2
Non-dimensional variables.

Description, quantity	Non-dimensional quantity
Wall heat flux	$\Phi_w^* = \Phi_w/q_l^0$
Flame-wall distance	$y^* = y/\delta_L$
Axial distance	$x^* = x/\delta_L$
Velocity	$u^* = u/S_L^0$
Thermal flame thickness	$\delta_L^* = \delta_L^0/\delta_L$
Time	$t^* = t/(S_L^0/\delta_L)$ $t' = t/t_Q$
Overall heat release rate	$\dot{\omega}^* = \dot{\omega}/q_l^0$
Fuel (methane) consumption rate	$-\dot{\omega}_F^* = \int_0^L (-\dot{\omega}_F) dx / (\rho_u S_L^0 Y_{F,u})$
Temperature	$T^* = (T - T_u)/(T_b - T_u)$
Wall mass flux	$F_{\text{H}_2,w}^* = F_{\text{H}_2,w}/F_{\text{H}_2\text{max}}$
Wall-to-flame distance (Peclet number)	$\text{Pe} = y/(\dot{\omega}_{\text{max}}/\delta_L)$ $\text{Pe}_F = y/(-\dot{\omega}_F^{\text{max}})/\delta_L$ $\text{Pe}_{\text{OH}^*} = y/(\text{OH}^*)/\delta_L$

Table 3Premixed flame properties obtained for varying ϕ_u with given $N = 9984$ and $p_{\text{H}_2}^f = 10$ atm. SG for $\phi_u = 0.5$ and 1.0, DRM22 for $\phi_u = 1.5$.

Wall type	T_w [K]	ϕ_u [-]	S_u^0 [m/s]	δ_L [10^{-6} m]	q_l^0 [MW/m ²]	T_b [K]	δ_L^* [-]	t_Q^0 [-]	$\delta_L^{*,Q}$ [-]	$\Phi_{w,\text{max}}$ [MW/m ²]	$\Phi_{w,Q}$ [MW/m ²]	M [-]
IW	600	0.5	0.421	156.38	0.300	1716.80	4.224	63.01	2.186	0.152	0.151	110
IW	600	1.0	1.362	48.23	1.583	2367.50	6.537	208.51	2.342	1.111	0.890	56
IW	600	1.5	0.480	135.47	0.495	2117.30	5.017	74.21	2.339	0.305	0.267	158
PW	600	0.5	0.421	156.38	0.300	1716.80	4.224	38.12	2.284	0.224	≈ 0	178
PW	600	1.0	1.362	48.23	1.583	2367.50	6.537	168.49	6.119	0.139	≈ 0	147
PW	600	1.5	0.480	135.47	0.495	2117.30	5.017	45.92	5.758	0.0167	≈ 0	390
IW	750	0.5	0.938	100.89	0.546	1838.10	4.996	99.54	2.398	0.280	0.259	121
IW	750	1.0	2.146	43.815	2.006	2434.50	6.425	229.15	2.903	1.345	0.989	63
IW	750	1.5	0.921	102.282	0.775	2227.40	4.888	98.12	2.086	0.510	0.490	107
PW	750	0.5	0.938	100.89	0.546	1838.10	4.996	68.69	2.904	0.765	≈ 0	146
PW	750	1.0	2.146	43.815	2.006	2434.50	6.425	190.10	6.045	0.357	≈ 0	132
PW	750	1.5	0.921	102.282	0.775	2227.40	4.888	63.34	5.393	0.092	≈ 0	276

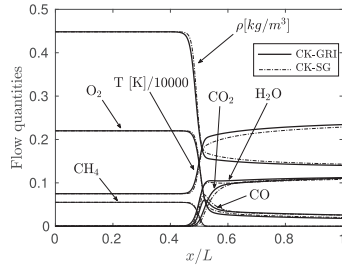
give a higher flame speed and flow velocity, shorter transit time and, accordingly, lower computational cost. Furthermore, one case of stoichiometric mixture at the low temperature of 300 K was carried out for comparison to results of Ganter et al. [34]. The wall heat flux and the time were non-dimensionalized as described in Section 2.4. It can be noted that the quenching times differed between this and previous investigations [34,10,23], since the initial flame locations and lengths of computational domains were not the same. These parameters should not influence on the obtained FWI results.

Table 4 presents the characteristics for the compared cases. The SG chemistry gave somewhat higher flame speeds than GRI during FWI, with corresponding differences for other quantities. Also shown is comparison of SG as used here (from [34]) and “SG(orig)” with the original coefficients of [35] (see Section 2.2). The seemingly small

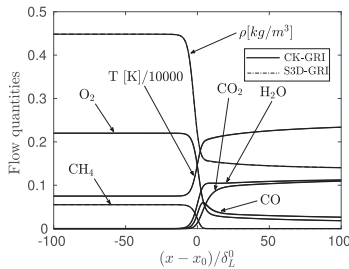
modifications gave notable improvement.

Fig. 3 presents the normalized wall heat fluxes for SG and GRI for wall temperatures of 300 K ($\phi_u = 1.0$) and 750 K ($\phi_u = 0.5, 1.0$ and 1.5). The mechanisms showed good agreement in terms of heat flux profiles, except for the rich mixture. At 750 K, SG gave a moderate under-prediction in comparison to GRI of the wall heat flux for lean and stoichiometric conditions. These deviations occurred primarily during quenching. For the rich mixture, SG failed. The peak of the wall heat flux was 38% lower compared to GRI. On the contrary, DRM22 gave very good agreement with GRI for the rich mixture, indicating that C2 compounds play a notable role.

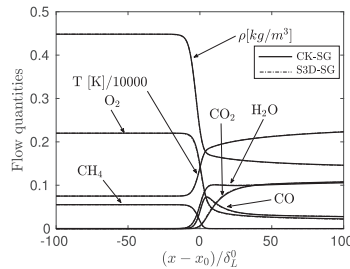
In the following, computations are performed at wall temperatures of 600 K and 750 K for IW and PW configurations with SG for $\phi_u = 0.5$ and 1.0, and with DRM22 for $\phi_u = 1.5$.



(a) GRI 3.0 vs. SG in Chemkin (CK)



(b) Chemkin (CK) vs. S3D, both with GRI 3.0

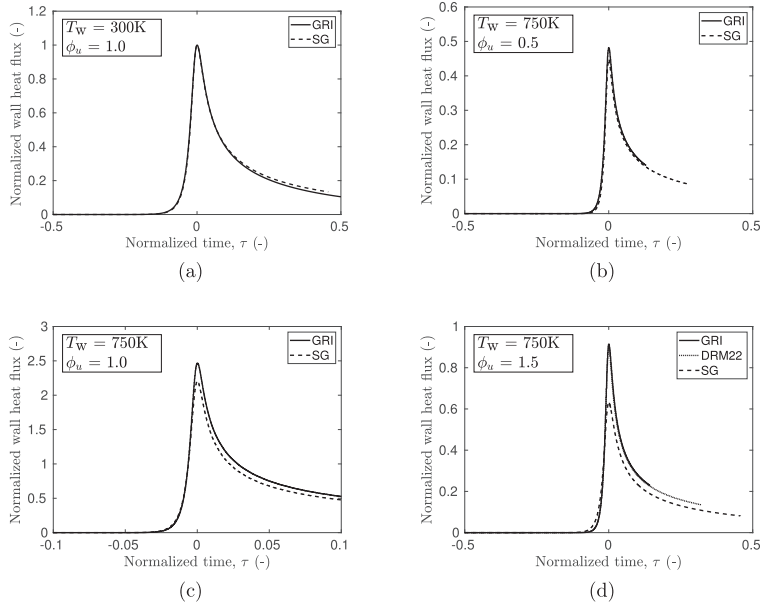
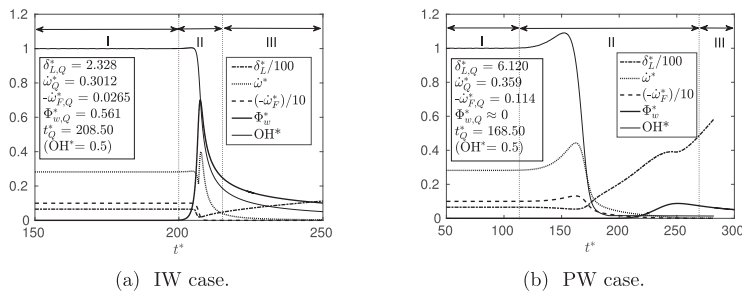


(c) Chemkin (CK) vs. S3D, both with SG

Fig. 2. Temperature, major species mass fractions and density profiles from Chemkin and S3D codes for SG and GRI 3.0 mechanisms. Free propagating laminar premixed methane flame. The unburnt mixture was stoichiometric at 750 K.

Table 4Premixed flame properties for different ϕ_u conditions for IW configurations at $T_w = 300$ K and 750 K.

ϕ_u [–]	N [–]	T_w [K]	Mech [–]	S_L^0 [m/s]	$\dot{\omega}_{\max}$ [10 ⁹ W/m ³]	δ_L [10 ^{−6} m]	δ_L^* [–]	$\delta_{L,Q}^*$ [–]	$\dot{\omega}_{Q,\max}/\dot{\omega}_{\max}$ [–]	q_w^0 [MW/m ²]	$\Phi_{w,\max}^*$ [–]	$\Phi_{w,Q}^*$ [–]
1.0	9984	300	SG(orig)	0.538	6.979	37.420	9.736	2.824	3.919	1.245	0.667	0.662
1.0	9984	300	SG	0.384	4.667	52.111	8.250	1.913	0.974	0.894	0.638	0.634
1.0	9984	300	GRI	0.381	4.393	53.376	8.005	1.901	0.701	0.887	0.643	0.639
0.5	9984	750	SG(orig)	1.072	1.935	88.252	5.352	2.207	0.603	0.624	0.548	0.508
0.5	9984	750	SG	0.938	1.689	100.89	4.996	2.398	0.212	0.546	0.512	0.474
0.5	9984	750	GRI	0.830	1.825	113.91	4.259	2.125	0.213	0.483	0.569	0.544
1.0	9984	750	SG(orig)	2.763	16.047	34.015	7.602	2.400	2.820	2.585	0.712	0.526
1.0	9984	750	SG	2.146	12.133	43.815	6.425	2.903	0.710	2.006	0.670	0.493
1.0	9984	750	GRI	2.007	11.043	46.832	6.027	2.976	0.558	1.877	0.702	0.684
1.5	9984	750	SG(orig)	2.198	11.642	42.881	6.166	2.091	1.621	1.850	0.878	0.856
1.5	9984	750	SG	0.646	1.630	145.873	4.529	1.981	0.315	0.543	0.407	0.329
1.5	9984	750	DRM22	0.921	2.760	102.282	4.888	2.086	0.453	0.775	0.658	0.632
1.5	9984	750	GRI	0.945	2.926	99.678	4.861	2.222	0.508	0.796	0.656	0.636

**Fig. 3.** Development of normalized wall heat fluxes for IW: SG and DRM22 compared to GRI 3.0. The quenching wall heat flux at $T_w = 300$ K, $\phi_u = 1.0$ with GRI was used for normalization. The abscissa is $\tau = (t - t_Q)/t_Q$, where t_Q is the quenching time.**Fig. 4.** Non-dimensional FWI characteristic parameters at $T_w = 600$ K and $\phi_u = 1.0$. The values at quenching are included.

3.3. Flame-wall interaction characteristics

The head-on flame quenching process can be described by FWI global parameters. The global development could be subdivided into three stages [17,5] as seen in Figs. 4 and 5: Undisturbed propagation, Stage I, influence of wall to propagating flame, Stage II, including quenching, and Stage III after quenching with overall decrease of fuel reaction and heat release rates. For IW, the propagating flame sensed the wall influence at $t^* = 200$, while much earlier for PW, at $t^* = 115$.

Figs. 4 and 5 present non-dimensional temporal profiles of FWI characteristics (δ_L^* , $-\dot{\omega}_F^*$, $\dot{\omega}^*$, Φ_w^* , OH^* , Pe , Pe_F , Pe_{OH^*}) of IW and PW configurations for stoichiometric conditions, $T_u = T_w = 600\text{ K}$, $p_{\text{H}_2}^i = 10\text{ atm}$ and $N = 9984$.

In Stage I, the flame propagates as an undisturbed laminar flame. The flame thickness, primary-fuel (methane) consumption rate and heat release rate reached steady values at $\delta_L^* = 6.54$, $-\dot{\omega}_F^* = 9.99$ and $\dot{\omega}^* = 0.282$. For IW Stage II, the fuel consumption rate declined towards zero during quenching and then remained zero. The heat release rate declined before quenching to $\dot{\omega}^* = 0.211$ at $t^* = 206.8$, then rapidly reached a peak value of 0.399 at $t^* = 207.6$, and declined after quenching. The peak wall heat flux was $\Phi_w^* = 0.702$ at $t^* = 207.4$, where the thermal flame thickness reached a minimum value, $\delta_L^* = 1.90$. Thereafter, the flame broadened. Quenching occurred at $t^* = 208.5$, as defined by the OH gradient (cf. Section 2.4). Accordingly, the quenching instance was close to the peak wall heat flux. The wall-to-flame distance based on reaction heat release, Pe , reached zero at $t^* = 206.8$, while Pe_F and Pe_{OH^*} reached minimum values of 1.91 and 2.49, respectively, at quenching.

For PW, the wall hydrogen permeation shortened Stage I, while Stage II was about 10 times longer than for IW. The primary-fuel consumption and the heat release rates peaked in Stage II with $-\dot{\omega}_F^* = 0.132$ and $\dot{\omega}^* = 0.443$, both at $t^* = 162.7$. From its peak, $\dot{\omega}^*$ declined to 0.359 at $t^* = 168.5$ (quenching) and further to a low value. The primary-fuel consumption rate $-\dot{\omega}_F^*$ declined gradually after its peak value, while the flame thickness grew from $t^* = 162.7$ and was $\delta_L^* = 6.12$ at quenching. The wall-flame distance according to the different definitions, Pe , Pe_{OH^*} and Pe_F , was virtually the same and reached 49.4 at quenching (Fig. 5b). That is, contrary to IW, quenching occurred away from the wall for PW.

3.4. Development through quenching

Fig. 6 displays the temporal development of profiles of reduced temperature, velocity and total reaction heat release for IW and PW. The profiles remained virtually unchanged until $t' = t/t_0 = 0.95$ or $t^* = 198.1$ for IW, and until $t' = 0.90$ or $t^* = 151.6$ for PW. Similarly, Figs. 7–10 show profiles of selected species.

The peak temperature gradient of IW reached to 3.45 times the

maximum temperature gradient of the free propagating flame. In comparison, Popp and Baum [10] found a value of 4.0 at quenching. The difference can be attributed to differences in chemical mechanism, numerical method and grid. After quenching, a remaining, much weaker reaction zone expanded for both IW and PW. For IW, the gas velocity decreased gradually and became negative, while PW showed higher (positive) values indicating the hydrogen flow across the wall.

Besides the obvious occurrence of permeated H_2 near the wall for PW, the notable difference from IW was the unreacted major species. Fig. 7 shows considerable amounts of CH_4 and O_2 remaining near the wall after quenching for PW. For IW, these species were nearly consumed, while modest amounts of H_2 and CO (Fig. 9e) were left. Among minor species, it was noted some accumulation of HO_2 in front of the flame for both configurations (Fig. 9c–d), more for PW than for IW. Similarly, and to greater extent, H_2O_2 was accumulated in front of the flame, increased in the flame and, for PW, remained left over after quenching, Fig. 8d.

Behind the propagating flame, the O_2 level was significantly lower for PW than for IW (Figs. 7c–d). On the contrary, the corresponding CO level was higher. It was also noted that the burnt-mixture temperature for PW decreased towards quenching.

Radicals H , O , OH were formed in the flame and partly consumed (Fig. 9) in both configurations. For PW, O and OH declined before quenching. This decline started before the flame reached the maximum heat release rate ($t' = 0.966$) for PW, while for IW their peaks were maintained to this point (at $t' = 0.996$).

For IW, it was seen that the flame front continued almost unchanged from the free propagation state close up to the wall before quenching. This was also consistent with the development of the heat release rate and fuel reaction rate seen in Fig. 4a. The initial reactants CH_4 and O_2 were to a large extent consumed during the process, and the final mixture approached that of the adiabatic equilibrium product.

The IW flame propagated against a flow caused by heating and expansion (Figs. 6c, e). In addition to said effects, the PW flame faced a flow enhanced by permeating gas. This, combined with an increasing heat release (Fig. 6f) and expansion, gave a larger velocity against the flame propagation. Although the heat release increased, the temperature gradient of the flame front showed a moderate increase from $t' = 0.98$. Furthermore, the overall temperature rise, i.e. the burned temperature, had a minor decrease.

The notable difference from IW, was the early, off-wall quenching of the PW flame. High concentrations of the main reactants CH_4 , H_2 and O_2 were left behind in the near-wall zone after quenching (Figs. 7b, d, f). As the flame propagated against the increasingly richer near-wall zone, the reaction heat release increased (Fig. 6f). Similarly, several intermediates from the methane and hydrogen consumption increased. CO had a minor increase in the flame zone, while an increasing amount was left behind the flame (Fig. 9f). On the other hand, the accumulation of

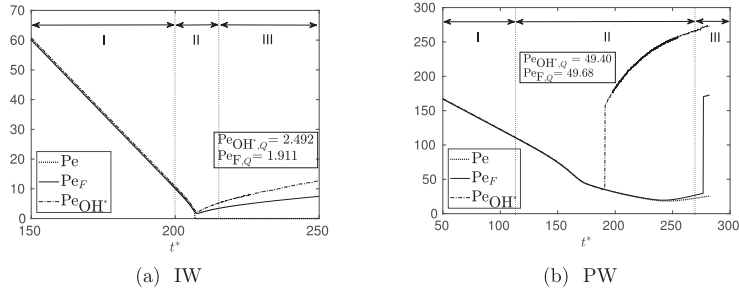


Fig. 5. Peclet numbers versus non-dimensional time for $\phi_u = 1.0$ and $T_w = 600\text{ K}$. The values at quenching are included.

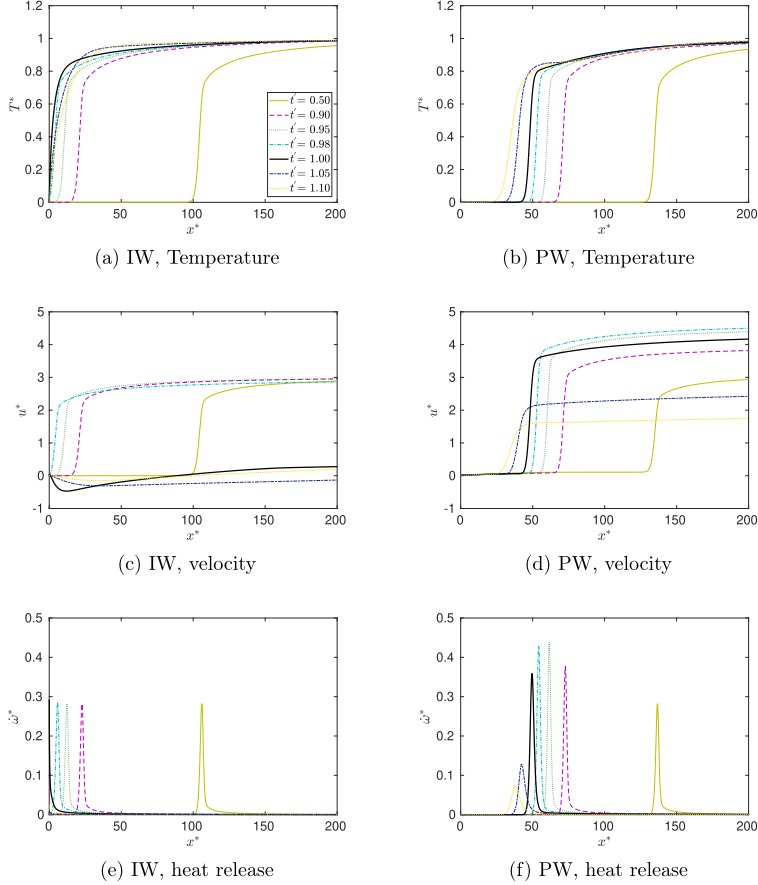


Fig. 6. Non-dimensional temperature, gas-flow velocity and total reaction heat release rate at different times of FWI for $\phi_u = 1.0$ and $T_w = 600$ K. $t' = 1$ represents flame quenching time.

O and O_2 decreased (Figs. 10d,f).

The species balance can be expressed as

$$T_k = \frac{\partial}{\partial t}(\rho Y_k) = C_k + D_k + R_k, \quad (3)$$

where the three right-hand-side terms denote, respectively, the contributions of convection, diffusion and reactions to the transient accumulation of the species (left-hand side). An analysis of the species balances (Convection-Diffusion-Reaction, CDR) showed that the changes of OH and O_2 became visible earlier than for other species, however visible later, from $t' = 0.95$ (most species) or $t' = 0.98$ (H_2O_2 , H, H_2O). The corresponding graphs for the IW case showed only minor changes until after $t' = 0.98$. These were similar (apart from the effects of the deviating unburned temperature) to those of Jiang et al. [9]. It can be noted that the quenching definition applied by said authors corresponded to $t' = 0.976$ of the present work.

3.5. Heat release rate and individual reactions

Fig. 12 presents temporal non-dimensional heat release rates. The total heat release rate is also shown in Fig. 4, together with the wall heat flux and the fuel (methane) reaction rate. At peak wall heat flux, the heat release rate reached 1.37 times that of the undisturbed laminar flame for IW. At quenching, this value was 1.02. For PW, quenching occurred when the heat release was 1.30 times that of free propagation, whereas only 0.016 at the peak wall heat flux. The breakdown of elementary reactions during freely propagating and quenching states for IW and PW are displayed in Table 5. Here, the heat release rate of individual net two-way reactions are evaluated at the location of the maximum total heat release rate.

In front of the propagating flame, H_2 was present (also for IW), together with HO_2 , H_2O_2 and CH_3 . The HO_2 was produced from R5(f), and then converted to H_2O_2 through R21(f), which had a peak ahead of the flame front. Both these reactions had zero activation energy, and occurred at low temperature. The latter reaction had minimal contribution in the flame zone. When approaching the flame, H_2O_2 was

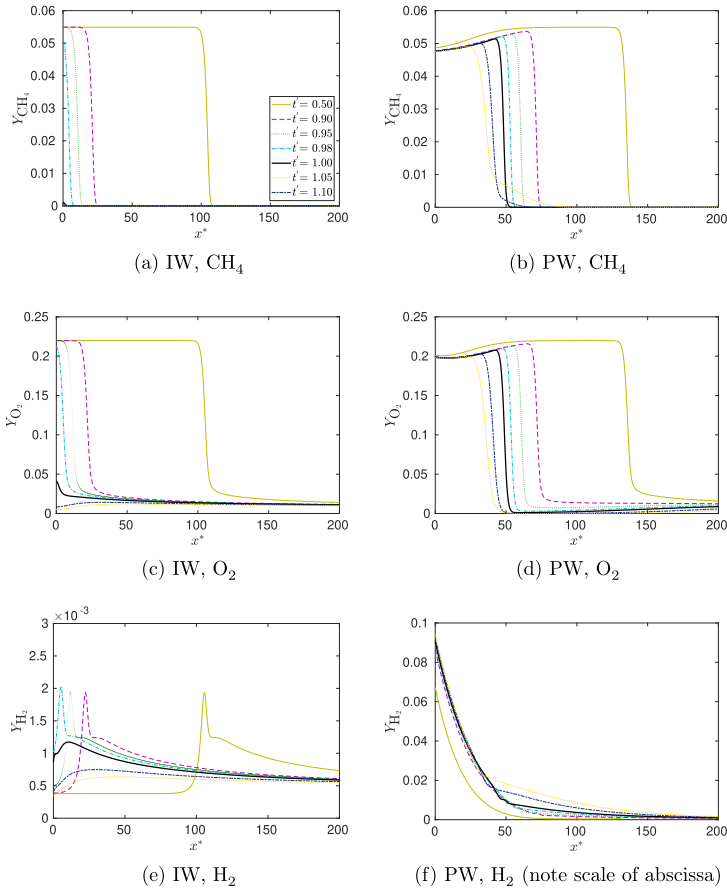


Fig. 7. Species mass fraction profiles of CH_4 , O_2 and H_2 at stoichiometric conditions, 600 K, for IW and PW. t' = 1 represents flame quenching time.

consumed by R22(f) and, to lesser extent, by R23(f). Other radical and intermediate species had a net production primarily in the flame zone, while declining after the flame front.

In the case of IW, R5(f) increased strongly towards quenching at the wall. Also R23(f) and R21(f) increased, consuming H_2O_2 now produced in the reversed R22. From Table 5 it is seen that the 9 most important reaction in the free flame (7 exothermic, 2 endothermic) almost completely lost their contributions at quenching, while others rose to maintain a comparable total heat release.

For PW, the importance of the reactions were maintained into quenching. Subsequently, the decaying reactions still generated some heat, and the wall heat flux reached a peak at $t^* = 250.1$. At this instance, the exothermic R10(r), R3(f), R5(f) and endothermic R1(f) caused about 90% of the total heat release.

3.6. Effects of varying equivalence ratio and temperature

Fig. 13 presents transient wall heat and mass fluxes at ϕ_u of 0.5, 1.0 and 1.5 for $T_w = 600$ K. For PW, the feed pressure $p_{\text{H}_2}^f$ was maintained at

10 atm. The varying equivalence ratios led to different free flame characteristics such as flame thickness and laminar flame speed and had significant influence on wall fluxes during flame quenching.

Table 3 showed that the highest combustion temperature and flame speed are obtained for $\phi_u = 1.0$. These values were lowered with increasing departure from stoichiometric conditions. For IW, the (dimensional) peak and quenching wall heat fluxes also had this tendency. For PW, however, it was an order of magnitude lower compared to IW for $\phi_u = 1.5$ and 1.0, while higher for $\phi_u = 0.5$. For IW with $\phi_u = 1.0$, radicals accumulated in the near-wall region owing to thermal loss from flame to wall. The radicals H, O and OH led to exothermic low-activation reactions with single peaks of heat release rate at the wall during FWI. These peaks resulted in a large wall heat flux at flame quenching. Fig. 13a shows that for IW, $\phi_u = 1.0$ led to the highest non-dimensional peak wall heat flux at the earliest quenching time (dimensional), while $\phi_u = 1.5$ and $\phi_u = 0.5$ had slightly lower peaks. The peak magnitudes of wall heat fluxes were primarily depending on the near-wall reaction heat release. At quenching for stoichiometric conditions, the main reactions R5(f), R24(f), R6(f) and R7(f) in decreasing order contributed 81.47% of the total heat release at the wall. Moreover, HO_2 and H_2O_2

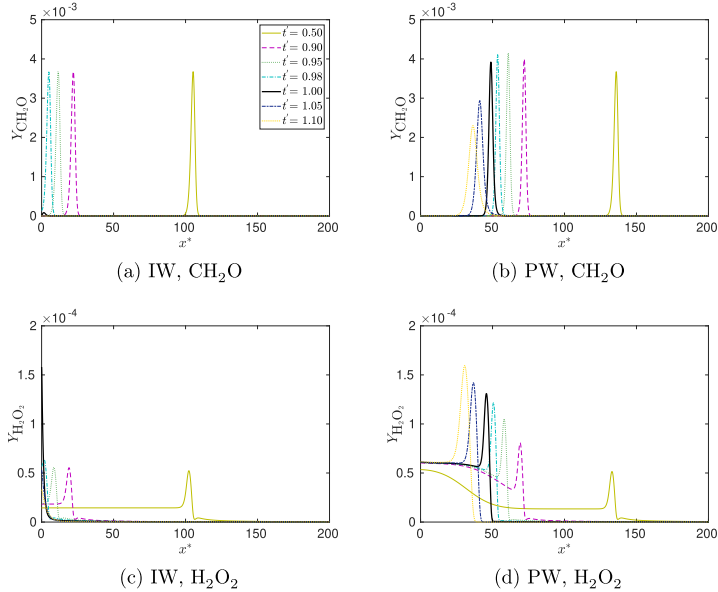


Fig. 8. Species mass fraction profiles of CH_2O and H_2O_2 at stoichiometric conditions, 600 K, for IW and PW.

had accumulated at the quenching instance.

In the rich flame, excess fuel led to main exothermic reactions in decreasing order (DRM22 reactions numbered consecutively from [36]), R34(f) [$\text{H} + \text{CH}_3 + \text{M} \rightarrow \text{CH}_4 + \text{M}$], R6(f) [$\text{O} + \text{CH}_3 \rightarrow \text{H} + \text{CH}_2\text{O}$], R92(f) [$2\text{CH}_3 + \text{M} \rightarrow \text{C}_2\text{H}_6 + \text{M}$] and R49(f) [$\text{OH} + \text{H}_2 \rightarrow \text{H} + \text{H}_2\text{O}$] and endothermic reaction R24(f) [$\text{H} + \text{O}_2 \rightarrow \text{O} + \text{OH}$] contributing 75.41% of the total heat release at wall. The C2 chemistry played a significant role, contributing 21.12% of the total heat release rate at flame quenching, including 16.63% from R92(f). The lowest peak of heat release occurred in the lean mixture, with excess of radicals OH and O in the near-wall region. It was seen that at quenching R13(f) [$\text{O} + \text{C}_2\text{H}_2 \rightarrow \text{CO} + \text{CH}_2$], R5(f) [$\text{O} + \text{CH}_2(\text{s}) \rightarrow \text{H} + \text{HCO}$] and R15(f) [$\text{O} + \text{C}_2\text{H}_5 \rightarrow \text{CH}_3 + \text{CH}_2\text{O}$] in decreasing order contributed 80.26% of the total heat release at the wall.

For the PW configuration, the wall heat flux variation (primarily) depended on the initial mixture composition and the accumulated H_2 wall flux, which promoted a pool of H during the FWI process. This resulted in enhanced heat release at some distance from the wall.

As with IW, PW had the earliest quenching at $\phi_u = 1.0$. For all three stoichiometries, the main reactions were, in decreasing order, R13(f), R10(r), R3(f), R5(f), while R1(f) had a notable endothermic contribution to the large heat release rate (for DRM22, the same reactions, although with other numbers). The combined contributions of said reactions were 90.45%, 85.61% and 45.92% of the total heat release for $\phi_u = 0.5$, 1.0 and 1.5, respectively.

Compared to IW, quenching was delayed for stoichiometric and rich mixtures, with peak wall heat fluxes reduced to 0.125 and 0.055, respectively, for $\phi_u = 1.0$ and 1.5, of the IW values. On the other hand, the lean case ($\phi_u = 0.5$) led to earlier quenching with a peak wall heat flux 1.467 times that of IW.

The transient wall H_2 mass fluxes of PW are shown in Fig. 13b. All conditions showed a decreasing trend of the non-dimensional $F_{\text{H}_2, \text{w}}^*$ until quenching. The flux reflected the changing content of H_2 , Eq. (1), and for the rich case, the flux increased after quenching.

The wall and unburnt-gas temperature was increased from 600 to 750 K, while the feed pressure p_{f}^* of 10 atm was maintained. Fig. 14 presents normalized wall fluxes for the IW and PW configurations for varying equivalence ratios. The normalized wall fluxes showed trends for IW and PW similar to those observed for 600 K. However, the increase in wall heat flux from 600 to 750 K was notably larger for PW than for IW. Yet, the dimensional peak values (Table 3) were less for PW than for IW at $\phi_u = 1.5$ and 1.0. For the lean mixture, PW had notably higher heat flux compared to IW.

The quenching Peclet number $\text{Pe}_{\text{OH}^*, \text{O}}$, i.e. flame-wall distance, is presented in Fig. 15 for IW and PW for the two wall temperatures and three equivalence ratios. It should be noticed here that the lines between data points are included for readability, not necessarily showing the variation between the points. For IW, the dimensional distance was clearly shorter for the stoichiometric case (lesser δ_{L}) than for lean and rich. For PW, the distance increased with the equivalence ratio. At the higher wall temperature, the flame came closer to the wall, except for the rich PW case.

4. Discussion

4.1. Influence of thermal radiation

In the present study, radiation heat transfer was neglected, which is in agreement with previous research in methane [14,16,48,10] and hydrogen flames [17,19,18,5]. A simplified evaluation of heat transfer from the hot gases to the wall can be performed through post processing calculations using the optically thin flame assumption [49,50]. Previous estimates [5] performed for hydrogen flames showed that the radiation heat transfer was 6 orders of magnitude less than the total reaction heat release rate during free propagation and quenching of the flame.

A similar estimate was made for the present stoichiometric methane flame at the highest unburnt temperature (750 K). It showed that the total reaction heat release was 4 orders of magnitude larger than the

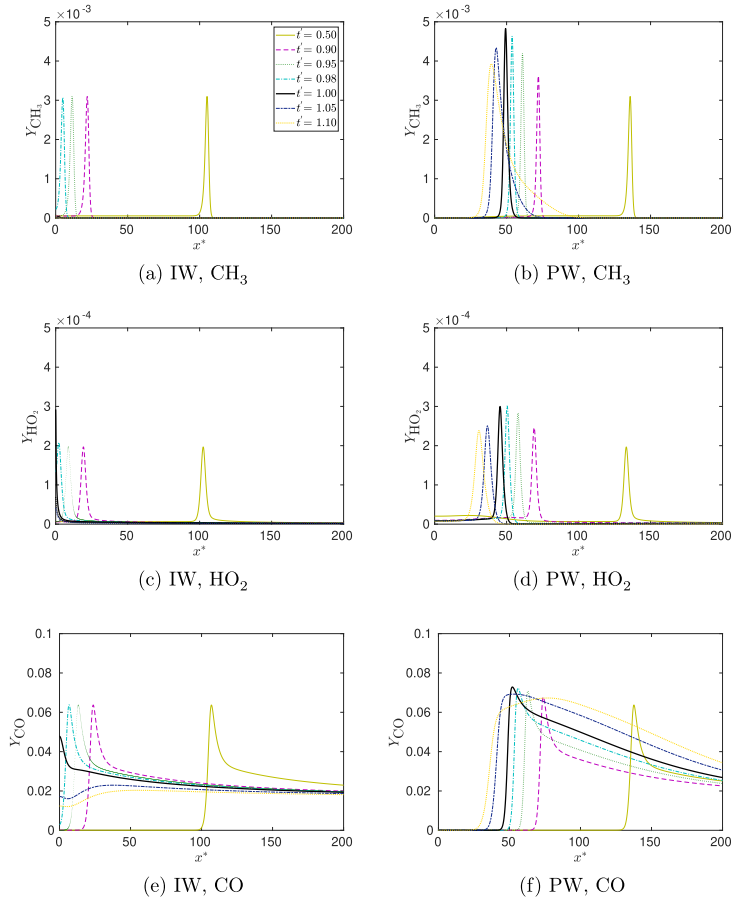


Fig. 9. Species mass fraction profiles of CH_3 , HO_2 and CO at stoichiometric conditions, 600 K, for IW and PW.

emitted radiation heat. Near quenching at the wall, the ratio increased to 5 orders of magnitude. Consequently, neglecting radiation heat transfer appeared to be justified for this configuration.

4.2. Validity of chemical mechanisms

The reduced mechanisms SG and DRM22 were regarded to meet the requirements for lower computational costs, while use of a full mechanism like GRI 3.0 was considered as too demanding. For comparison with SG and DRM22, some IW cases were simulated with GRI 3.0 (Section 3.2 with Table 4). The SG mechanism provided sufficiently good results for lean and stoichiometric conditions. However, it failed for the rich mixture, as could be expected in the absence of C2 chemistry and higher carbon-chain reactions. DRM22 showed good agreement with GRI for rich flames. It was seen (Section 3.6) that the C2 reactions of DRM22 had notable contributions to the total reaction heat release. Therefore, DRM22 was employed for $\phi_u = 1.5$, while the simpler (cheaper) SG for $\phi_u = 0.5$ and 1.0.

4.3. Definitions of flame quenching

Various definitions of the quenching instance and flame position can be found in literature. Westbrook et al. [6] choose the iso-contour at 1500 K (for $T_u = 300$ K) nearest to the wall as the flame position, and defined quenching at the instance where this distance had its minimum value.

Others have used the instance of the maximum wall heat flux as the criterion for quenching. With this definition, the flame position has been chosen as a more or less arbitrary temperature iso-line, such as 1900 K [23] or $T^* = 0.9$ [48], the position of the maximum heat release rate ($\dot{\omega}^*$) [22,10,17] or the position of maximum fuel consumption rate ($-\dot{\omega}_F^*$) [17]. Each of these positions constituted the quenching distance when the quenching occurred.

In the spirit of Westbrook et al. [6], the instance of the minimum thermal flame thickness δ_f^0 could be taken as the quenching instance.

Another potential criterion is the instance of peak maximum reaction heat release. Then, its location at this instance can determine the quenching distance. A further possibility (e.g., [9]) is to define the flame position by the location of maximum fuel (methane)

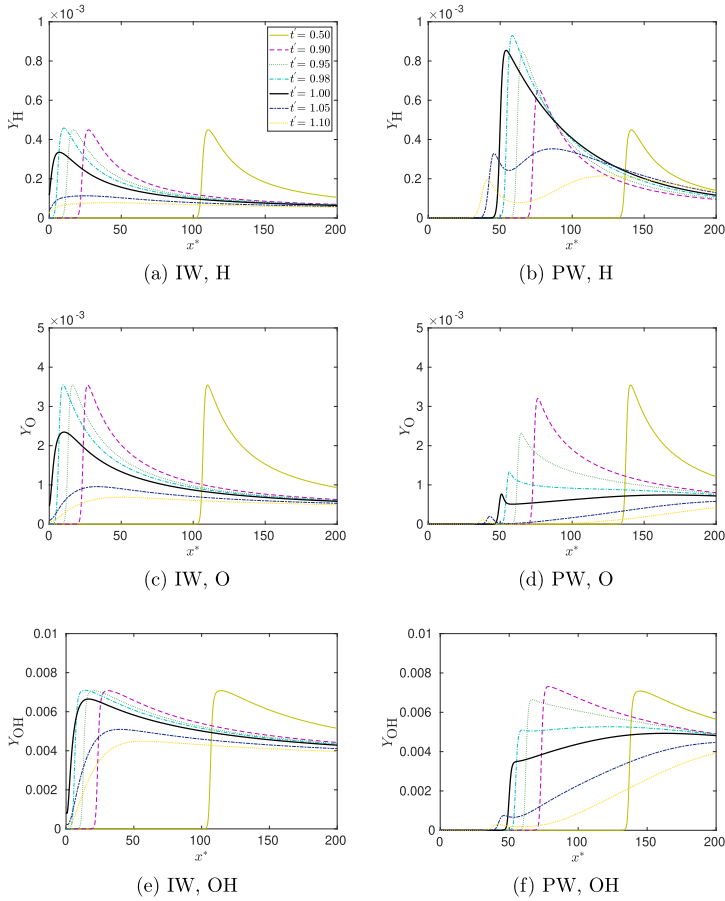


Fig. 10. Species mass fraction profiles of radicals H, O and OH at stoichiometric conditions, 600 K, for IW and PW.

consumption. The quenching instance is the time of the minimum wall-flame distance, and the quenching distance is this distance.

A different approach was chosen by [46], defining quenching to the instance when the spatial OH gradient fell below half its maximum value. The point of maximum instantaneous OH gradient was taken as the flame position and hence, the quenching distance. This definition was explained and used above, Section 2.4.

Table 6 compares the quenching instance according to the different criteria together with the associated flame-wall distances for the case of $\phi_0 = 1.0$ and $T_w = 600$ K. The results illustrated that, for this specific IW case, the choice of quenching-instance criterion would give a minute impact on the result. For the PW case, however, the maximum wall-heat flux criterion appeared unsuitable. This could also be seen from the transient profiles of Fig. 4b.

A related issue is the time-scale for flame-wall interaction. This has been defined [22,13] as the time required for Φ_w to increase to its maximum from half of this value. For the present PW cases, this timescale loses its significance.

4.4. Head-on quenching process

Above, e.g. in Figs. 4–5, the global development was subdivided into three stages following Dabireau et al. [17]. This description was clearly suitable for the IW cases. The study of H_2 /air [5] showed this development, as well, both for IW and PW. The present PW case showed similarities to these, but also deviations. An alternative description could be in four stages, where the present Stage II is split into two: one comprising quenching and one including the later increasing and peaking wall heat flux.

The reasons for the early, away from wall, quenching in the PW cases can be a combination of factors. First, it can be noted that the amount of permeated H_2 was considerable. Up to quenching for the case of $T_w = T_0 = 600$ K and $\phi_0 = 1.0$, the amount of substance of permeated H_2 exceeded the amount of CH_4 initially present in the domain. The molar fraction of H_2 became high near the wall, above 50%. In spite of this, there was still a significant amount of O_2 left at quenching. Hence, lack of oxidizer was not the primary reason for quenching. The high near-wall H_2 concentration can be relevant for the near-wall zone

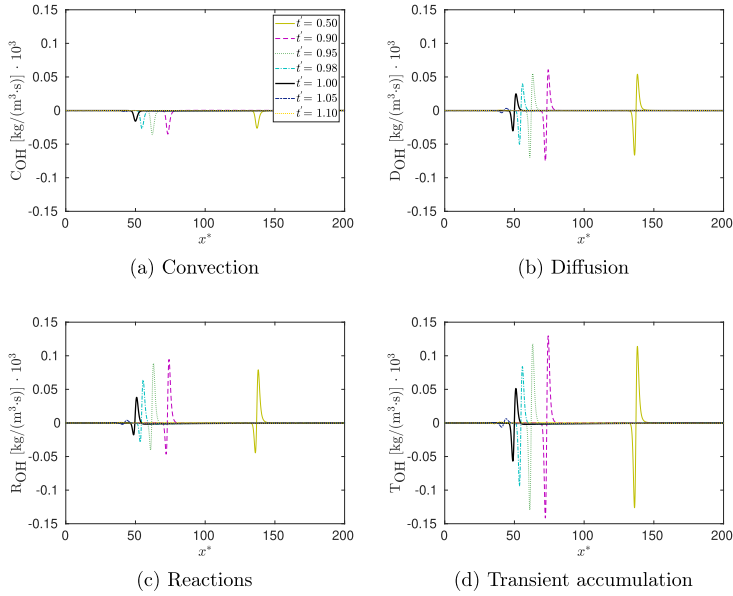


Fig. 11. Convection–Diffusion–Reaction balances of OH at different times near quenching for PW of $\phi_u = 1.0$ and $T_w = 600$ K. C, D and R show contributions to OH accumulation (T) due to, respectively, convection, diffusion and reactions.

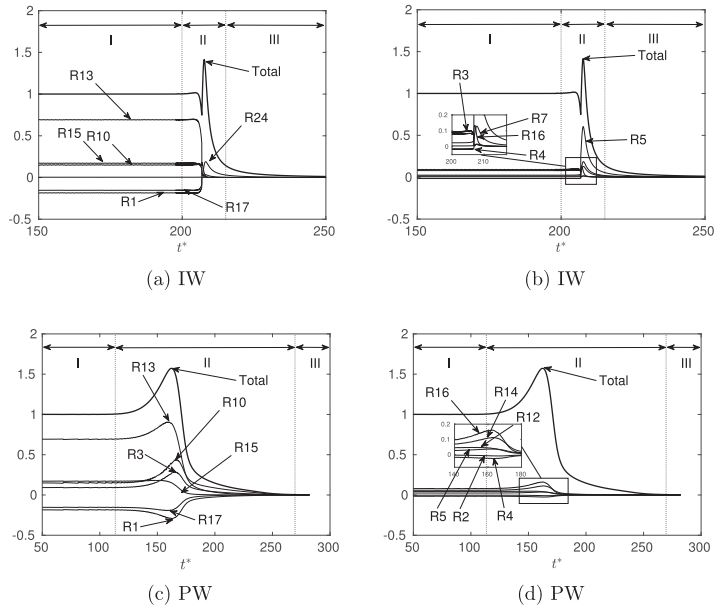


Fig. 12. Non-dimensional heat release profiles for total (overall) heat release rate and individual reactions at $\phi_u = 1.0$ and $T_w = 600$ K. The total heat release rate of the freely propagation flame was used for normalization.

Table 5

Heat release rate of individual reactions (% of the total heat release rate) at $\phi_u = 1.0$ and $T_w = 600$ K for the freely propagating flame, and for quenching at IW and PW. Net reactions are forward (f) or reverse (r).

Free prop.		IW at t_Q^*		PW at t_Q^*	
Reaction	%	Reaction	%	Reaction	%
R13(f)	69.113	R5(f)	41.276	R13(f)	48.922
R15(f)	17.143	R24(f)	16.969	R10(r)	32.222
R10(r)	14.783	R6(f)	13.732	R3(f)	20.579
R3(f)	9.243	R7(f)	9.500	R16(f)	8.495
R16(f)	7.955	R8(f)	3.246	R14(f)	7.109
R14(f)	5.850	R9(f)	2.968	R15(f)	6.637
R12(f)	4.381	R1(r)	2.871	R5(f)	2.363
R9(f)	2.481	R16(f)	1.890	R12(f)	2.130
R5(f)	2.421	R25(f)	1.695	R6(f)	1.375
R6(f)	1.335	R22(r)	1.691	R9(f)	0.847
R7(f)	0.462	R4(f)	1.266	R7(f)	0.472
R24(f)	0.339	R3(f)	0.905	R24(f)	0.239
R8(f)	0.259	R10(r)	0.842	R19(f)	0.161
R19(f)	0.108	R15(f)	0.302	R25(f)	0.152
R25(f)	0.070	R13(f)	0.299	R8(f)	0.087
R23(f)	0.003	R23(f)	0.203	R23(f)	0.001
R21(f)	0.000	R17(r)	0.191	R21(f)	0.000
R20(f)	-0.001	R12(f)	0.083	R20(f)	-0.001
R22(f)	-0.016	R21(f)	0.071	R22(f)	-0.051
R18(f)	-0.039	R14(f)	0.000	R18(f)	-0.062
R11(f)	-0.177	R18(r)	0.000	R11(f)	-0.190
R2(f)	-0.271	R19(f)	0.000	R2(f)	-0.663
R4(r)	-1.609	R20(r)	0.000	R4(r)	-1.792
R17(f)	-15.343	R2(f)	0.000	R17(f)	-10.562
R1(f)	-18.492	R11(f)	0.000	R1(f)	-18.471

of a membrane combustor, although not for the overall combustor volume.

Second, the burnt temperature was to some degree reduced (although the gradient increased in the flame zone). This related to the large additional fuel and increased local equivalence ratio. The reduction in temperature, albeit not very large, affected the temperature-dependent reactions. It was observed that towards quenching the conversion of H, O and OH was reduced, both for the consumption in the front of the flame and the production in the back. Similarly, the conversion of intermediates CH_3 , CH_2O , HCO and HO_2 was reduced (production in front, consumption in the back of the flame). This coincided with less conversion of major species and lesser reaction heat release. Moreover, when observing the individual species balances (CDR budget analysis, Section 3.4), it was seen that the balance of OH was affected earlier than other species. The mass-fraction profiles showed that OH and O (Figs. 9d,f), contrary to other intermediates, were depleted prior to quenching. The large presence of the major reactants CH_4 , H_2 and O_2

clearly indicated that the temperature and dilution led to the reduced conversion.

Third, due to the permeation, the gas velocity increased, Fig. 6d, compared to IW. The enhanced convective heat transfer away from the wall and flame contributed to the reduced temperature in the flame. Moreover, a significant amount of unburnt fuel, primarily CO (Fig. 9f), was carried from the flame.

Although not investigated here, except by the limit of no wall mass flux, it could be anticipated that a lower permeation rate should give later quenching and shorter quenching distance. Correspondingly, the initially lean flames also gave lesser quenching distances (Fig. 15).

5. Conclusions

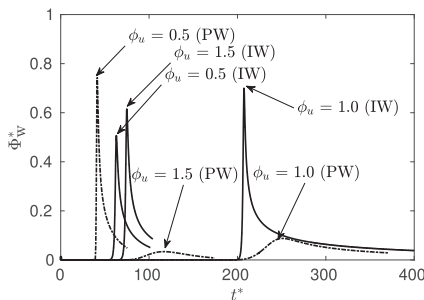
Flame-wall interactions were investigated for a one-dimensional laminar premixed methane-air flame with an isothermal, chemically inert impermeable wall (IW) and a hydrogen-permeable wall (PW). Two temperatures (600 and 750 K) of wall and unburnt gas were selected. Hydrogen released through the permeable wall participated in the methane-air combustion as a secondary fuel.

Initially, it was verified by comparison with GRI 3.0 [37] that for lean and stoichiometric mixtures, the reduced mechanisms of Smooke and Giovangigli [35] (with slightly modified parameters) can represent the chemistry. For rich methane-air mixtures, the DRM22 mechanism [36], including C2-chemistry, can be used. The simulations confirmed previous work on head-on-quenching towards an impermeable wall.

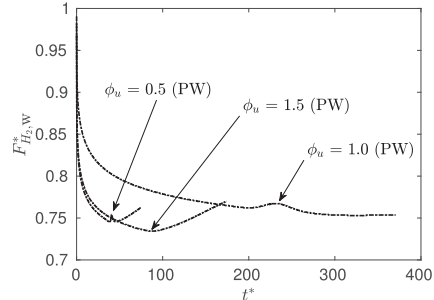
For the permeable wall, the hydrogen flow significantly altered the flame-wall interactions. Flame quenching occurred at a notable distance from the wall. It was apparent that this was neither due to lack of oxidizer nor to heat loss to the wall. Actually, quenching took place before the flame heated the wall significantly. The early quenching appeared to be a result of the mutual effects of large local concentration of H_2 , a reduced flame temperature and increased convective heat transfer away from the wall and flame. When the flame approached the wall and the increasing H_2 concentration, OH accumulation was reduced before other species (but O_2) were affected.

Subsequent to quenching, some modest reaction heat release still took place near the wall. This gave a peak wall heat flux a while after the quenching instance, although much less than for the impermeable wall.

The discussion of quenching definitions showed that some are applicable to the PW case. In the present study, the quenching instance was based on the OH gradient [46]. Also definitions based on maximum reaction heat release and of the minimum flame thickness appeared applicable. On the other hand, the definition based on maximum wall heat flux failed to capture the cease of major reaction heat release.



(a) Normalized wall heat fluxes, Φ_w^* .



(b) Normalized wall mass fluxes, $F_{\text{H}_2, \text{w}}^*$.

Fig. 13. Transient wall heat fluxes and mass fluxes for varying ϕ_u for IW and PW at $T_w = 600$ K.

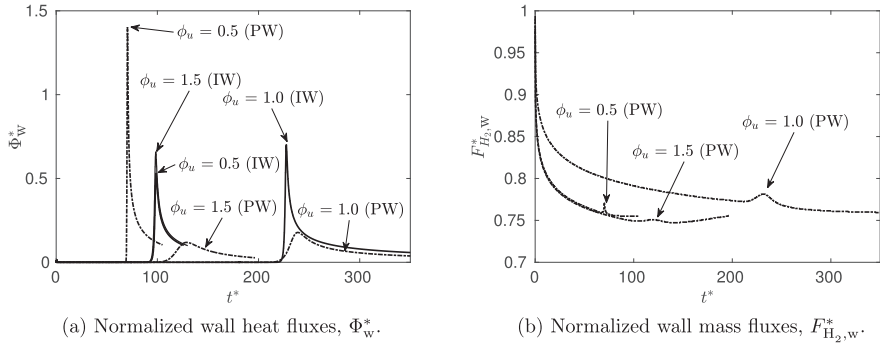


Fig. 14. Transient wall heat fluxes and mass fluxes for varying ϕ_u for IW and PW at $T_w = 750$ K.

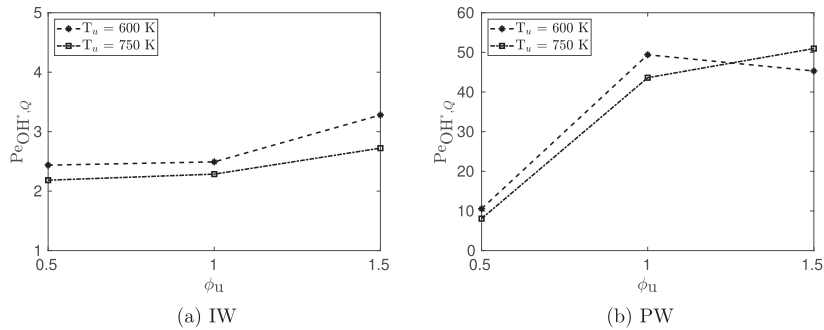


Fig. 15. Non-dimensional flame-wall distance at quenching, $Pe_{OH^*,Q}$, for $T_w = 600$ K and 750 K and varying ϕ_u .

Table 6

Results of various criteria for quenching and the associated flame-wall distances for the case $\phi_u = 1.0$ and $T_w = 600$ K. The criterion for the quenching instance is applied first; then the distance is determined at this instance.

Criterion for quenching		for IW		for PW	
instance, t_Q	distance, y_Q	t_Q^0	y_Q/δ_L	t_Q^0	y_Q/δ_L
OH gradient max Φ_w	max OH gradient	208.5	2.49	168.5	49.4
	1700 K isocontour	207.4	3.5	251.0	43.9
	1800 K isocontour		5.2		71.2
	Pe (i.e. max $\dot{\omega}$)		0.0		18.7
	Pe_F (i.e. max $(-\dot{\omega}_F)$)		1.75		20.7
min δ_L^0	δ_L^0	207.4	1.90	161.6	5.43
max $\dot{\omega}$	Pe	207.6	0.0	162.7	57.9
max $(-\dot{\omega}_F)$	Pe_F	203.5	6.40	162.7	57.7
min Pe	Pe	206.9	0.0	245.4	18.4

Declarations of interest

None.

CRediT authorship contribution statement

Prashant S. Salimath: Conceptualization, Software, Validation, Formal analysis, Investigation, Data curation, Writing - original draft, Visualization. **Ivar S. Ertesvåg:** Conceptualization, Formal analysis, Data curation, Writing - original draft, Writing - review & editing, Supervision. **Andrea Gruber:** Conceptualization, Methodology,

Software, Data curation, Writing - review & editing, Supervision.

Acknowledgments

The work of the 1st author (Salimath) was partly funded by the Research Council of Norway through the project CCERT – CO₂ Capture with Enabling Research and Technology, while the work at SINTEF (Gruber) has been funded by the Research Council of Norway through the project 280578 “Distributed Hydrogen Injection and Combustion Technology for Next Generation Pre-Combustion CCS Schemes”. We are grateful to the Norwegian Metacenter for Computational Science (NOTUR) for providing the HPC computational resources and useful technical support (project No. NN9400K).

References

- [1] Poinset T, Veynante D. Theoretical and numerical combustion. Philadelphia PA, USA: R.T. Edwards Inc; 2005.
- [2] Dreizler A, Böhm B. Advanced laser diagnostics for an improved understanding of premixed flame-wall interactions. Proc Combust Inst 2015;35(1):37–64. <https://doi.org/10.1016/j.proci.2014.08.014>.
- [3] Gruber A, Sankaran R, Hawkes E, Chen J. Turbulent flame-wall interaction: a direct numerical simulation study. J Fluid Mech 2010;658:5–32. <https://doi.org/10.1017/S0022112010001278>.
- [4] Gruber A, Salimath PS, Chen JH. Direct numerical simulation of laminar flame-wall interaction for a novel H₂-selective membrane/injector configuration. Int J Hydrogen Energy 2014;39(11):5906–18. <https://doi.org/10.1016/j.ijhydene.2014.01.148>.
- [5] Salimath PS, Ertesvåg IS, Gruber A. Premixed hydrogen-air flames interacting with a hydrogen porous wall. Int J Hydrogen Energy 2018;43(7):3822–36. <https://doi.org/10.1016/j.ijhydene.2017.12.166>.
- [6] Westbrook CK, Adamczyk AA, Lavoie GA. A numerical study of laminar flame wall

- quenching. *Combust Flame* 1981;40:81–99. [https://doi.org/10.1016/0010-2180\(81\)90112-7](https://doi.org/10.1016/0010-2180(81)90112-7).
- [7] Hasse C, Bollig M, Peters N, Dwyer HA. Quenching of laminar iso-octane flames at cold walls. *Combust Flame* 2000;122(1–2):117–29.
 - [8] Kiehne TM, Matthews RD, Wilson DE. The significance of intermediate hydrocarbons during wall quench of propane flames. *Proc Combust Inst* 1986;21(1):481–9. [https://doi.org/10.1016/S0082-0784\(88\)80276-5](https://doi.org/10.1016/S0082-0784(88)80276-5).
 - [9] Jiang B, Gordon RL, Talei M. Head-on quenching of laminar premixed methane flames diluted with hot combustion products. *Proc Combust Inst* 2019;37:5095–103. <https://doi.org/10.1016/j.proci.2018.07.120>.
 - [10] Popp P, Baum M. Analysis of wall heat fluxes, reaction mechanisms, and unburnt hydrocarbons during the head-on quenching of a laminar methane flame. *Combust Flame* 1997;108(3):327–48. [https://doi.org/10.1016/S0010-2180\(96\)00144-7](https://doi.org/10.1016/S0010-2180(96)00144-7).
 - [11] Boust B, Sotton J, Labuda SA, Bellenoue M. A thermal formulation for single-wall quenching of transient laminar flames. *Combust Flame* 2007;149(3):286–94. <https://doi.org/10.1016/j.combustflame.2006.12.019>.
 - [12] Owston R, Magi V, Abraham J. A numerical study of thermal and chemical effects in interactions of n-heptane flames with a single surface. *Combust Flame* 2007;148(3):127–47. <https://doi.org/10.1016/j.combustflame.2006.10.006>.
 - [13] Sotton J, Boust B, Labuda SA, Bellenoue M. Head-on quenching of transient laminar flame: heat flux and quenching distance measurements. *Combust Sci Technol* 2005;177(7):1305–22. <https://doi.org/10.1080/00102200590950485>.
 - [14] Ezekoye O, Greif R, Sawyer R. Increased surface temperature effects on wall heat transfer during unsteady flame quenching. *Proc Combust Inst* 1992;24:1465–72. [https://doi.org/10.1016/S0082-0784\(06\)80171-2](https://doi.org/10.1016/S0082-0784(06)80171-2).
 - [15] Popp P, Smooke M, Baum M. Heterogeneous/homogeneous reaction and transport coupling during flame-wall interaction. *Proc Combust Inst* 1996;26(2):2693–700. [https://doi.org/10.1016/S0082-0784\(96\)80105-6](https://doi.org/10.1016/S0082-0784(96)80105-6).
 - [16] Huang W, Vosen S, Greif R. Heat transfer during laminar flame quenching: effect of fuels. *Proc Combust Inst* 1986;21:1853–60. [https://doi.org/10.1016/S0082-0784\(88\)80420-X](https://doi.org/10.1016/S0082-0784(88)80420-X).
 - [17] Dabireau F, Cuenot B, Vermorel O, Poinot T. Interaction of flames of H₂ + O₂ with inert walls. *Combust Flame* 2003;135(1–2):123–33. [https://doi.org/10.1016/S0010-2180\(03\)00000-0](https://doi.org/10.1016/S0010-2180(03)00000-0).
 - [18] Mari R, Cuenot B, Rochi J-P, Selle L, Duchaine F. Effect of pressure on hydrogen/oxygen coupled flame-wall interaction. *Combust Flame* 2016;168:409–19. <https://doi.org/10.1016/j.combustflame.2016.01.004>.
 - [19] Owston R, Magi V, Abraham J. Interactions of hydrogen flames with walls: Influence of wall temperature, pressure, equivalence ratio, and diluents. *Int J Hydrogen Energy* 2007;32(12):2094–104. <https://doi.org/10.1016/j.ijhydene.2006.07.030>.
 - [20] Aghalayam P, Bui PA, Vlachos DG. The role of radical wall quenching in flame stability and wall heat flux: hydrogen-air mixtures. *Combust Theory Model* 1998;2(4):515–30. <https://doi.org/10.1088/1364-7830/2/4/010>.
 - [21] Yenerdag B, Minamoto Y, Aoki K, Shimura M, Nada Y, Tanahashi M. Flame-wall interactions of lean premixed flames under elevated, rising pressure conditions. *Fuel* 2017;189:8–14. <https://doi.org/10.1016/j.fuel.2016.10.096>.
 - [22] Vosen S, Greif R, Westbrook C. Unsteady heat transfer during laminar flame quenching. *Proc Combust Inst* 1984;20:75–83. [https://doi.org/10.1016/S0082-0784\(85\)80490-2](https://doi.org/10.1016/S0082-0784(85)80490-2).
 - [23] Ghani A, Poinot T. Flame quenching at walls: a source of sound generation. *Flow, Turbul Combust* 2017;99(1):173–84. <https://doi.org/10.1007/s10494-017-9810-5>.
 - [24] Gounder JD, Kutne P, Gruber A. Experimental Investigation of a Bluff Body Burner for Distributed Hydrogen Injection. In: GT2017, Volume 4A: Combustion, Fuels and Emissions, ISBN 978-0-7918-5084-8; 2017. <https://doi.org/10.1115/GT2017-63414>.
 - [25] Chen J, Choudhary A, de Supinski B, DeVries M, Hawkes E, Klasky S, Liao W, Ma K, Mellor-Crummey J, Podhorski N, Sankaran R, Shende S, Yoo C. Terascale direct numerical simulations of turbulent combustion using S3D. *Comput Sci Discov* 2009;2(1):15001. <https://doi.org/10.1088/1749-4699/2/1/015001>.
 - [26] Chen J. Petascale direct numerical simulation of turbulent combustion – fundamental insights towards predictive models. *Proc Combust Inst* 2011;33(1):99–123. <https://doi.org/10.1016/j.proci.2010.09.012>.
 - [27] Sankaran R, Hawkes E, Chen J, Lu T, Law C. Direct numerical simulations of turbulent lean premixed combustion. *J Phys Conf Ser* 2006;46(1):38–42. <https://doi.org/10.1088/1742-6596/46/1/004>.
 - [28] Grout RW, Gruber A, Yoo CS, Chen JH. Direct numerical simulation of flame stabilization downstream of a transverse fuel jet in cross-flow. *Proc Combust Inst* 2011;33(1):1629–37. <https://doi.org/10.1016/j.proci.2010.06.013>.
 - [29] Hawkes E, Sankaran R, Sutherland J, Chen J. Scalar mixing in direct numerical simulations of temporally evolving plane jet flames with skeletal CO/H₂ kinetics. *Proc Combust Inst* 2007;31(1):1633–40. <https://doi.org/10.1016/j.proci.2006.08.079>.
 - [30] Lignell DO, Chen JH, Smith PJ, Lu T, Law CK. The effect of flame structure on soot formation and transport in turbulent nonpremixed flames using direct numerical simulation. *Combust Flame* 2007;151(1–2):2–28. <https://doi.org/10.1016/j.combustflame.2007.05.013>.
 - [31] Sankaran R, Im HG, Hawkes ER, Chen JH. The effects of non-uniform temperature distribution on the ignition of a lean homogeneous hydrogen-air mixture. *Proc Combust Inst* 2005;30(1):875–82. <https://doi.org/10.1016/j.proci.2004.08.176>.
 - [32] Echehki T, Chen JH. Direct numerical simulation of autoignition in non-homogeneous hydrogen-air mixtures. *Combust Flame* 2003;134(3):169–91. [https://doi.org/10.1016/S0010-2180\(03\)00088-9](https://doi.org/10.1016/S0010-2180(03)00088-9).
 - [33] Kennedy CA, Carpenter MH. Several new numerical methods for compressible shear-layer simulations. *Appl Numer Math* 1994;14(804):397–433. [https://doi.org/10.1016/0168-9274\(94\)00004-2](https://doi.org/10.1016/0168-9274(94)00004-2).
 - [34] Ganter S, Heinrich A, Meier T, Kuenne G, Jaini C, Rißmann MC, Dreizler A, Janicka J. Numerical analysis of laminar methane-air side-wall-quenching. *Combust Flame* 2017;186:299–310. <https://doi.org/10.1016/j.combustflame.2017.08.017>.
 - [35] Smooke M, Giovangigli V. Formulation of the premixed and nonpremixed test problems. In: Smooke M, editor. *Lect. Notes Phys.* vol. 384. Springer Verlag; 1991. p. 1–28.
 - [36] Kazakov A, Frenklach M. Reduced Reaction Sets Based on GRI-Mech 1.2. URL: combustion.berkeley.edu/drm [accessed 19 Nov. 2019].
 - [37] Smith GP, Golden DM, Frenklach M, Eiteener B, Goldenberg M, Bowman CT, Hanson RK, Song S, Gardiner WC, Lissianski VV, Qin Z. GRI-Mech 3.0. URL: combustion.berkeley.edu/gri_mech/ [accessed 22 Nov. 2019].
 - [38] Kee RJ, Rupley FM, Miller JA. CHEMKIN-II: A FORTRAN chemical kinetics package for the analysis of gas phase chemical kinetics, SANDIA Rep. No. SAND89-8009B; 1989, pp. 3–164.
 - [39] Kee RJ, Dixon LG, Warnatz J, Coltrin ME, Miller JA, Moffat HK. A fortran chemical kinetics package for the analysis of gas-phase chemical kinetics [Tech. Rep.]. Release 3.5. Reaction Design Inc.: San Diego, CA; 1999.
 - [40] Bredesen R, Jorhal K, Bolland O. High-temperature membranes in power generation with CO₂ capture. *Chem Eng Process Process Intensif* 2004;43(9):1129–58. <https://doi.org/10.1016/j.ccep.2003.11.011>.
 - [41] Gustafsson B, Sundström A. Incompletely parabolic problems in fluid dynamics. *SIAM J Appl Math* 1978;35(2):343–57. <https://doi.org/10.1137/0135030>.
 - [42] Nordström J, Svard M. Well-posed boundary conditions for the Navier-Stokes equations. *SIAM J Numer Anal* 2005;43(3):1231–55. <https://doi.org/10.1137/040604972>.
 - [43] Strikwerda JC. Initial boundary value problems for incompletely parabolic systems. *Commun Pure Appl Math* 1977;30(6):797–822. <https://doi.org/10.1002/cpa.3160300606>.
 - [44] Yoo CS, Wang Y, Trounev A, Im HG. Characteristic boundary conditions for direct simulations of turbulent counterflow flames. *Combust Theory Model* 2005;9(1):617–46. <https://doi.org/10.1080/13647830500307378>.
 - [45] Yoo CS, Im HG. Characteristic boundary conditions for simulations of compressible reacting flows with multi-dimensional, viscous and reaction effects. *Combust Theory Model* 2007;11(2):259–86. <https://doi.org/10.1080/13647830600898995>.
 - [46] Jaini C, Rißmann M, Böhm B, Janicka J, Dreizler A. Sidewall quenching of atmospheric laminar premixed flames studied by laser-based diagnostics. *Combust Flame* 2017;183:271–82. <https://doi.org/10.1016/j.combustflame.2017.05.020>.
 - [47] Jaini C, Rißmann M, Böhm B, Dreizler A. Experimental investigation of flame surface density and mean reaction rate during flame-wall interaction. *Proc Combust Inst* 2017;36(2):1827–34. <https://doi.org/10.1016/j.proci.2016.07.113>.
 - [48] Poinot T, Haworth DC, Bruneaux G. Direct simulation and modeling of flame-wall interaction for premixed turbulent combustion. *Combust Flame* 1993;95(1–2):118–32. [https://doi.org/10.1016/0010-2180\(93\)90056-9](https://doi.org/10.1016/0010-2180(93)90056-9).
 - [49] Barlow R, Smith N, Chen J-Y, Bilger R. Nitric oxide formation in dilute hydrogen jet flames: isolation of the effects of radiation and turbulence-chemistry submodels. *Combust Flame* 1999;117(1):4–31. [https://doi.org/10.1016/S0010-2180\(98\)00071-6](https://doi.org/10.1016/S0010-2180(98)00071-6).
 - [50] Radiation models URL: www.sandia.gov/TNF/radiation.html (accessed 20 June 2019).

Article 4

Local entropy generation and entropy fluxes of a transient flame during head-on quenching towards solid and hydrogen-permeable porous walls

Prashant S. Salimath, Ivar S. Ertesvåg

Published in International Journal of Hydrogen Energy

Available online at www.sciencedirect.com

ScienceDirect

journal homepage: www.elsevier.com/locate/hydro

Local entropy generation and entropy fluxes of a transient flame during head-on quenching towards solid and hydrogen-permeable porous walls

Prashant S. Salimath, Ivar S. Ertesvåg^{*}

Department of Energy and Process Engineering, Norwegian University of Science and Technology, Kolbjørn Hejes Vei 1b, NO-7491, Trondheim, Norway

HIGHLIGHTS

- Premixed hydrogen-air flame propagating towards a hydrogen-permeating wall.
- Entropy generation due to conductivity, mass diffusion and chemical reactions.
- Effects of initial temperature, fuel-air ratio and dilution.
- Entropy generation per unit of fuel reduced by fuel permeation into lean flame.

ARTICLE INFO

Article history:

Received 10 July 2020

Received in revised form

5 February 2021

Accepted 20 May 2021

Available online 18 June 2021

Keywords:

Entropy production

Entropy flux

Transient

Head-on quenching

Components of entropy generation

Detailed chemical mechanism

ABSTRACT

Premixed H₂-air flames are studied in a one-dimensional wall-bounded configuration. The laminar flame propagates towards and quenches at a wall that is either solid or permeable. Entropy generation by each of 19 elementary reactions is evaluated. Their total contribution remains the most important up to the quenching instance. Close to quenching, the conduction entropy generation grows considerable. Mass diffusion has a modest contribution, which decreases towards quenching. Viscous forces are negligible as a source of entropy. Effects of unburnt-mixture temperature and fuel-air ratio are investigated, and also dilution with nitrogen (inert) and water vapour. The diffusive entropy flux changed direction away from the permeating wall compared that of the solid wall. A major finding is that fuel permeation through the wall tends to decrease the entropy generation per unit of converted fuel, in particular for initially lean mixtures.

© 2021 The Author(s). Published by Elsevier Ltd on behalf of Hydrogen Energy Publications LLC. This is an open access article under the CC BY license (<http://creativecommons.org/licenses/by/4.0/>).

Introduction

Strive for less-polluting, more efficient and more compact combustion devices has led to more intensive combustion

close to solid walls. These efforts also include new solutions like membrane reactors, where fuel or oxidizer are partly supplied through a porous wall into the combustor. Large efficiency losses can be the result of the concentrated fuel conversion close to solid surfaces. Some aspects of

^{*} Corresponding author.

E-mail addresses: Prashant.Salimath@ntnu.no (P.S. Salimath), Ivar.S.Ertesvag@ntnu.no (I.S. Ertesvåg).
<https://doi.org/10.1016/j.ijhydene.2021.05.142>

0360-3199/© 2021 The Author(s). Published by Elsevier Ltd on behalf of Hydrogen Energy Publications LLC. This is an open access article under the CC BY license (<http://creativecommons.org/licenses/by/4.0/>).

flame-wall interactions were investigated by direct numerical computations in our previous studies [1–3], in which also the state of the art of head-on quenching was reviewed.

Efficiency of energy conversion is determined by the first and, in particular, the second law of thermodynamics. Degrading of energy is expressed in form of exergy destruction, aka. irreversibility, and entropy generation. In classical engineering thermodynamics, 2nd law analysis has come into use for industrial process simulations in the form of exergy analysis [4,5]. This method is used to evaluate and optimize thermal plants (e.g. Refs. [6,7]). Since spatial (and to a large extent temporal) gradients are neglected, it is sometimes called a “zero-dimensional” method.

Computational fluid dynamics (CFD) provides detailed knowledge of the fields of temperature, species concentration, heat and mass fluxes. Then, the entropy generation can be provided with a similar level of detail in space and time. The recent decades have seen increasing efforts in such approaches. Som and Datta [8] reviewed the state of the art up to 2006 for reacting flows. Arpacı and Selamet [9] were in 1988 “probably the first one” (in the wording of [8]) to apply this approach in combustion; for a flat premixed flame. Later, simulations have been conducted for laminar and turbulent flames in a variety of premixed and non-premixed configurations. The laminar, premixed flames were in the form of a 1-dimensional planar flame [10–13], a counterflow jet flame [14], axisymmetric annular combustors [15,16], a cylindrical recuperated micro combustor [17], microchannel and [18–20], micro-planar combustors [21]. In spite of the variations in set-up and geometries, these studies all found chemical reactions to give the largest contribution to entropy generation, followed by heat conduction and mass diffusion. For the case of transition from a planar propagating flame front to auto-ignition, Liu et al. [13] found that the chemical contribution became dominant at autoignition and that the heat and mass transfer vanished as sources of entropy. Laminar, non-premixed flames have been investigated by several authors, both single-phase flames and gaseous flames around a fuel droplet. Datta [22] (confined jet flame), Stanciu et al. [23] (jet flame), Nishida et al. [10] (jet flame), Datta [24] (confined jet flame with gravity), Chen et al. [25] (counterflow jet flame) and Briones et al. [26] (lifted jet flame, that is, partially premixed) all found heat conduction as the most important for entropy generation, followed by reactions and then mass diffusion. On the other hand, Chen et al. [27], found the chemical reactions to be more important for entropy generation along the axis of an opposing jet flame. Raghavan et al. [28] and Pope et al. [29] found heat conduction to be the largest contributor to entropy generation in the flame around a fuel droplet, closely followed by chemical reactions, while mass diffusion was less important. All the studies, both premixed and non-premixed, agreed that the contribution of viscous dissipation was negligible in premixed and non-premixed flames, except in zones where the other contributions were very small [25].

Turbulent reacting flows can be investigated by direct numerical simulation (DNS) similar to laminar flames. This has been done for very simple flames, but usually either chemistry or turbulence, or both, have to be dealt with by some sort of

modeling and simplification. DNS with a single-step Arrhenius chemical model was used [30] to investigate entropy generation of a premixed flame in decaying turbulence at low Reynolds number. Other investigations were based on Reynolds-averaged Navier-Stokes (RANS) [23,31–34]. The modeling challenges faced by this approach were out of scope for the present study.

The majority of entropy-generation studies are made with the motivation of improving energy conversion. However, studies with other aims can also be found: Acoustic disturbances (noise) are related to entropy waves and generation of these. Investigations focused on thermal sources for such waves [35] and recently, also on differences in composition [36]. Furthermore, entropy has been related to soot formation [37], and used as a tool for reducing chemical mechanisms [38–40]. Another motivation has been to provide guidance with respect to realizability of physical submodels [41,42].

The present study was based on direct numerical computations [2] of a transient premixed laminar planar hydrogen flame propagating towards a solid wall, eventually quenching. Hydrogen permeation through the wall influences the overall head-on quenching (HOQ) process, including entropy generation and its components. Entropy generation through quenching has gained little attention in literature, and to our knowledge, entropy generation in HOQ flames has not been investigated previously.

The HOQ process involves flame propagation with reactions and heat losses. Large heat losses occur when the flame approaches the wall, which adversely affects hardware components and system performance. Conventional HOQ studies were performed for IW to understand near-wall reactions, heat transfer and flow physics. There is less focus towards understanding of irreversibilities during the HOQ process. In the present study, entropy analysis is performed for H₂ permeation on HOQ for different conditions and compared against convective impervious wall boundary results, to understand processes and also assist in design to improve performance of system such as micro combustion.

In the following, the theoretical background is given in Section [Models and numerical setup](#), with mathematical formulation of the entropy generation and entropy transport. In Section [Results and discussion](#), first results for the free propagating premixed flame will be shown and compared with other investigations. Next, results for the head-on quenching towards the wall will be shown. Here, both the impermeable and the hydrogen-permeable cases are studied for an initially stoichiometric mixture. Subsequently, the effect lean and rich mixtures, the unburnt-mixture temperature and dilution will be shown and discussed. Finally, conclusions are made.

Models and numerical setup

Governing equations, properties and constitutive relations

The governing equations and relations are described according to Chen et al. [43], which documents the code used.

Momentum balance:

$$\frac{\partial}{\partial t}(\rho u_\alpha) + \frac{\partial}{\partial x_\beta}(\rho u_\alpha u_\beta) = -\frac{\partial p}{\partial x_\alpha} + \frac{\partial}{\partial x_\beta}(\tau_{\beta\alpha}) \quad (1)$$

Energy is expressed in form of the total specific internal energy with the balance equation,

$$\frac{\partial}{\partial t}(\rho e_0) + \frac{\partial}{\partial x_\beta}((\rho e_0 + p)u_\beta) = \frac{\partial q_\beta}{\partial x_\beta} + \frac{\partial}{\partial x_\beta}(\tau_{\beta\alpha}u_\alpha). \quad (2)$$

Species mass:

$$\frac{\partial}{\partial t}(\rho Y_i) + \frac{\partial}{\partial x_\beta}(\rho Y_i u_\beta) = \frac{\partial}{\partial x_\beta}(-J_{\beta i}) + W_i \dot{\omega}_i. \quad (3)$$

The viscous stress, species diffusion velocity and heat flux are expressed as

$$\tau_{\alpha\beta} = \mu \left(\frac{\partial u_\beta}{\partial x_\alpha} + \frac{\partial u_\alpha}{\partial x_\beta} \right) - \frac{2}{3} \mu \frac{\partial u_\gamma}{\partial x_\gamma} \delta_{\alpha\beta}, \quad (4)$$

$$V_{\alpha i} = -\frac{D_i^{\text{mix}}}{X_i} d_{\alpha i} - \frac{D_i^T}{\rho Y_i} \frac{\partial}{\partial x_\alpha}(\ln T), \quad (5)$$

$$q_\alpha = -\lambda \frac{\partial T}{\partial x_\alpha} + \sum_{i=1}^{N_s} h_i J_{\alpha i} - \sum_{i=1}^{N_s} \frac{p}{\rho Y_i} D_i^T d_{\alpha i}, \quad (6)$$

$$d_{\alpha i} = \frac{\partial X_i}{\partial x_\alpha} + (X_i - Y_i) \frac{\partial}{\partial x_\alpha}(\ln p) \quad (7)$$

The species mass flux can be split into three components; the species gradient diffusion flux (Fick), the pressure diffusion flux and the thermodiffusion (Soret) flux:

$$J_{\alpha i} = \rho Y_i V_{\alpha i} = J_{\alpha i}^{\text{Fi}} + J_{\alpha i}^{\text{pd}} + J_{\alpha i}^{\text{So}} \quad (8)$$

The heat flux of Eq. (6) has three components, viz. the conductive flux (Fourier), the heat flux due to species mass fluxes $J_{\alpha i}$ (which has three components, according to Eq. (8)), and the Dufour flux:

$$q_\alpha = q_\alpha^{\text{Fo}} + q_\alpha^{\text{J}} + q_\alpha^{\text{Du}} \quad (9)$$

It can be noted that in Eqs. (1) and (7), effects of body forces (gravity, electrochemical) are left out. Moreover, the bulk viscosity is set to zero in Eq. (4). The Dufour effect (last term of Eq. (6)) was not implemented in the code, however included here for reference.

A kinetic energy equation can be deduced from the momentum equation. Using the relation

$$e_0 = h - \frac{p}{\rho} + \frac{1}{2} u_\alpha u_\alpha = e + \frac{1}{2} u_\alpha u_\alpha, \quad (10)$$

the energy equation, Eq. (2), can be reformulated to

$$\frac{\partial}{\partial t}(\rho e) + \frac{\partial}{\partial x_\beta}(\rho e u_\beta) = \frac{\partial q_\beta}{\partial x_\beta} - p \frac{\partial u_\alpha}{\partial x_\alpha} + \tau_{\beta\alpha} \frac{\partial u_\alpha}{\partial x_\beta} \quad (11)$$

The molar reaction rate of species i in Eq. (3) can be expressed from

$$\dot{\omega}_i = \sum_{j=1}^{N_R} \nu_{ij} q_j, \quad (12)$$

Here, $\nu_{ij} = \nu''_{ij} - \nu'_{ij}$ are the stoichiometric coefficients of reaction j , and

$$q_j = k_{fj} \prod_{i=1}^{N_s} \left(\frac{\rho Y_i}{W_i} \right)^{\nu'_{ij}} - k_{rj} \prod_{i=1}^{N_s} \left(\frac{\rho Y_i}{W_i} \right)^{\nu''_{ij}} \quad (13)$$

is the reaction progress. The forward rate coefficient is expressed as $k_{fj} = A_j T^{\theta_j} \exp(-E_j/(R_u T))$, while the reverse rate coefficient is expressed from the corresponding equilibrium constant, $k_{rj} = k_{fj}/K_{cj}$.

Entropy transport and generation

The numerical analysis of combustion is based on the equations above. By using the Gibbs relation for reacting systems, the entropy transport equation can be developed [44,45] as

$$\frac{\partial}{\partial t}(\rho s) + \frac{\partial}{\partial x_\beta}(\rho s u_\beta) = B_s + \sigma, \quad (14)$$

where the entropy diffusion term is

$$B_s = \frac{\partial}{\partial x_\beta} \left(\frac{1}{T} (-q_\beta^{\text{Fo}} - q_\beta^{\text{Du}}) - \sum_{i=1}^{N_s} s_i J_{\beta i} \right), \quad (15)$$

and the entropy generation rate is elaborated as the sum of contributions due to, respectively, viscous forces, conduction, Dufour flux, mass diffusion and chemical reactions:

$$\sigma = \sigma_{\text{visc}} + \sigma_{\text{cond}} + \sigma_{\text{Du}} + \sigma_{\text{diff}} + \sigma_{\text{chem}} \quad (16)$$

with

$$\sigma_{\text{visc}} = \frac{\tau_{\beta\alpha}}{T} \frac{\partial u_\alpha}{\partial x_\beta}, \quad (17)$$

$$\sigma_{\text{cond}} = \frac{1}{T^2} (-q_\beta^{\text{Fo}}) \frac{\partial T}{\partial x_\beta} = \frac{\lambda}{T^2} \left(\frac{\partial T}{\partial x_\beta} \right)^2, \quad (18)$$

$$\sigma_{\text{Du}} = \frac{1}{T^2} (-q_\beta^{\text{Du}}) \frac{\partial T}{\partial x_\beta}, \quad (19)$$

$$\sigma_{\text{diff}} = \sum_{i=1}^{N_s} (-J_{\beta i}) \left(\frac{1}{T} \frac{\partial h_i}{\partial x_\beta} - \frac{\partial s_i}{\partial x_\beta} \right), \quad (20)$$

$$\sigma_{\text{chem}} = -\frac{1}{T} \sum_{i=1}^{N_s} g_i W_i \dot{\omega}_i. \quad (21)$$

Among these, the mass-diffusion term can be decomposed into three contributions as $\sigma_{\text{diff}} = \sigma_{\text{Fi}} + \sigma_{\text{pd}} + \sigma_{\text{So}}$, according to the components of Eq. (8), while the chemical term can be decomposed into separate contributions from each elementary reaction. It should be noted that the contribution from the 2nd term of the heat flux, Eq. (9), is included in the mass-diffusion component, Eq. (20). The last term of Eq. (9), the Dufour flux, was neglected in the calculations. However, the entropy generation due to the Dufour flux, Eq. (19), should equal that of the Soret flux, according to the Onsager reciprocal relations. Therefore, this neglected amount of entropy generation can be estimated by calculating that of the Soret flux. Entropy generation due to heat sources (including radiation) and body forces (e.g., gravity) was left out.

The chemical potential (Gibbs function) for each species is expressed as $g_i = h_i - Ts_i$. For ideal gases, $dh_i = C_{p,i}dT$ and $ds_i = (C_{p,i}/T)dT - (R_i/p_i)dp_i$, with $R_i = R_u/W_i$ and $p_i = X_i p$, hence

$$\left(\frac{1}{T} \frac{\partial h_i}{\partial x_\beta} - \frac{\partial s_i}{\partial x_\beta} \right) = \frac{R_i}{p_i} \frac{\partial p_i}{\partial x_\beta} = \frac{R_u}{W_i} \left(\frac{1}{X_i} \frac{\partial X_i}{\partial x_\beta} + \frac{1}{p} \frac{\partial p}{\partial x_\beta} \right) \quad (22)$$

The specific entropy is expressed as

$$s_i = s_i^\circ(T) - \frac{R_u}{W_i} \left(\ln X_i + \ln \frac{p}{p_{\text{ref}}} \right) \quad (23)$$

The temperature part $s_i^\circ(T)$, and the enthalpy $h_i(T)$, are determined from polynomials [46,47].

The chemical term, Eq. (21), contains the volumetric reaction rate for each species. With Eqs. (12) and (13), the term can be reformulated to provide the contribution of the j th elementary reactions as

$$\sigma_{\text{chem},j} = - \sum_{i=1}^{N_s} \frac{g_i}{T} W_i \nu_{ij} q_j \quad (24)$$

The sum of these contributions will provide that of Eq. (21),

$$\sigma_{\text{chem}} = \sum_{j=1}^{N_R} \sigma_{\text{chem},j}$$

Exergy calculations

The exergy destruction rate was calculated as the product of the ambient temperature and the entropy generation rate, $T_0 \cdot \sigma$. The chemical exergy for H_2 was evaluated [4,48] to 238.16 kJ/mol for the ISO standard ambient air conditions for gas-turbine testing (15 °C, 1 atm, 60% relative humidity). In accordance with said standard, the ambient temperature was chosen as $T_0 = 288.15$ K. The calculation of chemical exergy at various ambient conditions was outlined by Ref. [4], and a comprehensive description and discussion of the accurate procedure was given by Ref. [48].

The DNS code and its assumptions

The S3D code is a massively parallel DNS solver developed at the Sandia National Labs, see Chen et al. [43]. It solves fully compressible momentum, total energy, species and mass continuity equations coupled with detailed chemistry. The code has been used for a wide range of studies of premixed (e.g. Refs. [3,49–51]) and non-premixed flames (e.g. Refs. [52–54]).

The transport equations were solved using an eighth-order explicit centered finite difference scheme in space (third-order one-sided stencils at the domain boundaries). A fourth-order six-stage explicit Runge-Kutta scheme was used for time integration [55]. Thermodynamic properties were modeled as polynomial functions of temperature and transport coefficients by the Chemkin and Transport packages [47,56].

The assumptions made in the S3D code were the ideal gas assumption for reactive fluid flow with continuum assumption for small length scales, body and buoyancy forces neglected, bulk viscosity neglected, a mixture-averaged diffusion coefficient used for all species, Dufour effect neglected, and no radiation heat transfer [43]. The Soret effect was implemented for light species (molar weight less than 5) [47], that is, H_2 and H .

Simulations of the head-on quenching flame

The present work made use of results from the previous studies, Salimath et al. [2], Gruber et al. [1]. The setup of the 1-dimensional cases is illustrated in Fig. 1. The flame front propagated in a premixed hydrogen/air mixture perpendicularly towards a solid wall facing the flame. The flame quenched when reaching the wall. Two configurations were investigated: a solid, impermeable wall (IW) and a hydrogen-permeable wall (PW). Both walls were chemically inert (no adsorption or catalytic effects). In the PW case, the flame became partly non-premixed, as H_2 seeped into the initial hydrogen-air mixture on the permeate side.

The numerical setup, models and boundary conditions are described previously, Salimath et al. [2]. Briefly outlined here, the domain had a length of $L = 0.02$ m, resolved in a uniform mesh of 4096 nodes and the time step fixed to $1.0 \cdot 10^{-9}$ s for all simulations. The air was assumed as 21% O_2 and 79% N_2 , molar based. The chemical mechanism of Li et al. [57] was used, with 19 elementary reactions (Table 1) comprising 8 species (H_2 , O_2 , H_2O , OH , H , O , HO_2 and H_2O_2) in addition to inert N_2 . The reactions are listed in Table 1, enumerated from R1 to R19. In the following, f and r will denote the forward and reverse net contributions of each reaction. The wall was assumed isothermal, and its temperature set equal to the unburnt-gas temperature, $T_w = T_u$. The pressure of the gas mixture was maintained at 1 atm. For the permeable wall, H_2 permeation occurred from $t = 0$.

It can be noted that for presentation purposes, results were extracted at every 1000 timesteps, i.e. at intervals of $1.0 \cdot 10^{-6}$ s. Furthermore, to provide correspondance with results from Ref. [2], the non-dimensional distance and time are used as $x^* = x/\delta_L$ and $t^* = t \cdot S_L^0/\delta_L$. Here, the laminar flame speed and thickness were used for the normalization.

The cases investigated had unburnt-mixture temperatures at 750 K, 500 K and 300 K, all with equivalence ratios at 0.5, 1.0 and 1.5. In addition, the stoichiometric cases at 750 K were diluted with nitrogen (two cases) and water vapour (two cases). All these 13 conditions were investigated for IW and for PW.

Results and discussion

Free propagating flame: verification and comparison

After initiation, the planar flame front moved undisturbed in the initially premixed fuel-air mixture. For a while, it behaved like a simple quasi-steady, 1-dimensional plane premixed flame. In our previous studies, it was seen that profiles from the undisturbed hydrogen-air [2] and methane-air [3] flames in S3D were virtually identical to results from Chemkin.

For comparison with previous work [10–12], the case of stoichiometric mixture and unburnt temperature 300 K was investigated.

Fig. 2 shows the spatial profiles of total entropy generation rate and its components due to chemical reactions, heat conduction and mass diffusion. The viscous contribution was

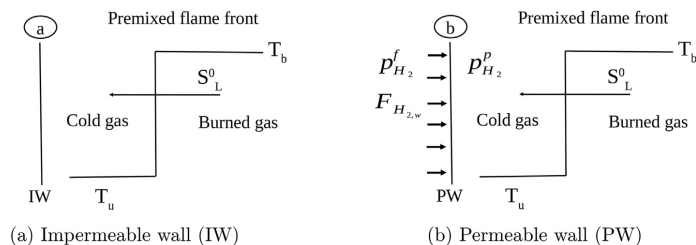


Fig. 1 – Head-on quenching configurations of impermeable and permeable walls with hydrogen flux.

Table 1 – Elementary reactions in the H_2 – O_2 chemical mechanism, Li et al. [57].

No.	Reactions
R1	$O_2 + H \rightleftharpoons OH + O$
R2	$H_2 + O \rightleftharpoons OH + H$
R3	$OH + H_2 \rightleftharpoons H + H_2O$
R4	$H_2O + O \rightleftharpoons 2OH$
R5	$H_2 + M \rightleftharpoons 2H + M$
R6	$2O + M \rightleftharpoons O_2 + M$
R7	$H + O + M \rightleftharpoons OH + M$
R8	$OH + H + M \rightleftharpoons H_2O + M$
R9	$O_2 + H + M \rightleftharpoons HO_2 + M$
R10	$H + HO_2 \rightleftharpoons O_2 + H_2$
R11	$H + HO_2 \rightleftharpoons 2OH$
R12	$O + HO_2 \rightleftharpoons OH + O_2$
R13	$OH + HO_2 \rightleftharpoons O_2 + H_2O$
R14	$2HO_2 \rightleftharpoons O_2 + H_2O_2$
R15	$H_2O_2 + M \rightleftharpoons 2OH + M$
R16	$H + H_2O_2 \rightleftharpoons OH + H_2O$
R17	$H + H_2O_2 \rightleftharpoons H_2 + HO_2$
R18	$O + H_2O_2 \rightleftharpoons HO_2 + OH$
R19	$OH + H_2O_2 \rightleftharpoons H_2O + HO_2$

left out as it could not visually be distinguished from the zero line. Also the entropy diffusion is included (Eq. (15)).

These results were found to be within the results of the previous studies. The chemical and mass-diffusion exergy flow rate, were virtually identical to those of Zhang et al. [11], while our peak of the conductive component was larger, close to that of Nishida et al. [10]. The results of Acampora and Marra

[12] seemed to be a little higher for all three components compared with our and the other results. The deviations may be attributed to differences in chemical mechanisms, transport models and numerical procedures.

Table 2 shows the quantities integrated spatially through the free propagating flame for some cases. Here, the chemical-reactions entropy generation is decomposed into the contributions from each of the 19 elementary reactions. Furthermore, the entropy generation due to mass diffusion is decomposed into the three components due to species gradient (Fick), pressure gradient and thermodiffusion (Soret).

In the table, the exergy destruction rate associated with the total entropy generation rate is also compared with the chemical exergy of the consumed hydrogen. The ratio of said quantities is included.

Head-on quenching

Fig. 3 shows the entropy generation and its components as function of time through quenching. For each timestep, the quantities were integrated over the length of the domain, $\int_0^L \sigma dx$. Also the integral of the diffusion, $\int_0^L B_s dx$ (Eq. (15)), is shown in the graphs.

The entropy generation due to reactions had a significant increase before the flame front reached the PW before fading off after quenching, while the IW case showed a gradual fade off.

The entropy generation of the most important elementary reactions are shown in Fig. 4. It is seen that the increase in the (overall) chemical component before quenching in the PW case was primarily due to reaction R8. Spikes from R5 and R8

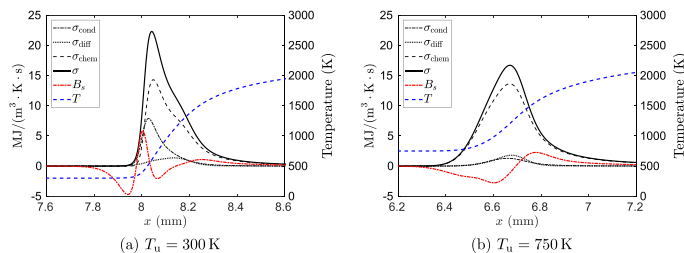


Fig. 2 – Components of entropy generation rate in the free propagating planar stoichiometric flame.

Table 2 – Components of entropy generation rate in a one-dimensional, quasi-steady planar H₂-air premixed flame (spatially integrated through the flame), fuel exergy and terms of the entropy equation.

ϕ_u (–)	1.0	1.0	0.5	1.5
T_u (K)	300	750	750	750
Total entropy generation rate (kW/(m ² K))	3.825	4.595	2.316	5.421
Heat conduction (fraction of total)	0.241	0.0615	0.0571	0.0636
Mass diffusion (of total)	0.0719	0.0698	0.0642	0.0702
Chemical reactions (of total)	0.687	0.869	0.879	0.866
Viscous forces (of total)	$3.2 \cdot 10^{-6}$	$5.4 \cdot 10^{-6}$	$2.3 \cdot 10^{-6}$	$6.2 \cdot 10^{-6}$
Species gradient (fraction of mass diffusion)	0.922	0.962	0.953	0.973
Pressure gradient (fraction of mass diffusion)	$1.08 \cdot 10^{-5}$	$4.4 \cdot 10^{-5}$	$1.7 \cdot 10^{-5}$	$4.6 \cdot 10^{-5}$
Thermal (Soret) (fraction of mass diffusion)	0.078	0.038	0.0475	0.0266
R1 (fraction of chem. Component)	0.0170	0.0318	0.0146	0.0501
R2	0.0208	0.0332	0.0262	0.0402
R3	0.117	0.162	0.160	0.164
R4	$9.9 \cdot 10^{-4}$	$3.6 \cdot 10^{-4}$	$9.8 \cdot 10^{-4}$	$2.0 \cdot 10^{-4}$
R5	0.0167	0.0305	0.101	0.0566
R6	$3.3 \cdot 10^{-4}$	$5.7 \cdot 10^{-4}$	$1.3 \cdot 10^{-3}$	$1.6 \cdot 10^{-4}$
R7	0.0276	0.0490	0.0387	0.0385
R8	0.231	0.289	0.193	0.288
R9	0.247	0.174	0.236	0.156
R10	0.0312	0.0258	0.0316	0.0235
R11	0.203	0.176	0.207	0.167
R12	0.0120	$9.3 \cdot 10^{-3}$	0.0312	0.0049
R13	0.0686	0.0126	0.0381	0.0070
R14	$6.4 \cdot 10^{-4}$	$3.9 \cdot 10^{-4}$	$9.6 \cdot 10^{-5}$	$3.1 \cdot 10^{-5}$
R15	0.00125	$8.2 \cdot 10^{-4}$	$1.6 \cdot 10^{-3}$	$4.0 \cdot 10^{-4}$
R16	$3.02 \cdot 10^{-3}$	$2.5 \cdot 10^{-3}$	$2.8 \cdot 10^{-3}$	$1.6 \cdot 10^{-3}$
R17	$4.1 \cdot 10^{-4}$	$5.9 \cdot 10^{-4}$	$4.8 \cdot 10^{-4}$	$3.9 \cdot 10^{-4}$
R18	$2.2 \cdot 10^{-4}$	$3.3 \cdot 10^{-4}$	$8.3 \cdot 10^{-4}$	$6.4 \cdot 10^{-5}$
R19	$1.98 \cdot 10^{-3}$	$2.2 \cdot 10^{-3}$	$4.6 \cdot 10^{-3}$	$5.9 \cdot 10^{-4}$
Fuel exergy converted (kW/m ²)	5337	11,375	4311	12,637
Exergy destruction ratio (–)	0.207	0.127	0.155	0.124
Entropy transient term (kW/(m ² K))	–11.77	–23.5	–12.6	–26.2
Entropy convection rate (kW/(m ² K))	15.59	28.1	15.0	31.6
Entropy diffusion rate (kW/(m ² K))	0.0035	–0.0016	$-2.3 \cdot 10^{-5}$	0.0050
Entropy generation rate (kW/(m ² K))	3.825	4.595	2.316	5.421

were counteracted by decrease in other reactions and were not visible in the chemical component, Fig. 3b.

Heat-conduction entropy generation had a notable increase through the quenching, and became the largest contribution after quenching. The mass diffusion contribution diminished to a negligible value for IW. For PW, the H₂

permeation caused some entropy generation also after quenching. The contribution from viscous forces was evaluated, but not included in the graphs, as the curves were not visibly distinguishable from zero. At quenching (t_Q^*), the non-dimensional viscous entropy generation σ_{visc}^* (cf. Fig. 3) had values of $2.2 \cdot 10^{-4}$ for IW and $6.9 \cdot 10^{-7}$ for PW.

The mass diffusion has three components (Eq. (8)). Their contributions are shown in Fig. 5. The pressure diffusion was very small due to a nearly constant pressure. The contribution of the Soret diffusion can be of particular interest, since it is usually neglected. The computations confirmed that the Soret entropy generation was very small. Just after quenching for PW, it peaked to 0.008 times the free-flame total entropy generation. Its contribution to the total entropy generation remained less than 1% for all times throughout quenching for PW and had a lesser contribution for IW.

When the flame approached the wall, the Soret entropy generation showed negative values. This was caused by a combination of a positive temperature gradient (negative Soret flux) and negative species gradients (primarily H₂). Negative contribution to entropy generation by the Soret effect was also observed by Torabi et al. [58]. It should be noted that a positive total entropy generation was maintained also at these instances.

Although the Dufour effect was not implemented in the code, its contribution to entropy generation can be evaluated from that of the Soret effect, which is of equal value.

The entropy diffusion components, Eq. (15), due to heat conduction and mass diffusion, respectively, had opposite signs. Both increased considerably towards the quenching instance, and then decreased. Since their relative weights were different for PW and IW, the resulting total entropy diffusion B_s had different signs for the two configurations, as seen in Fig. 3.

It was noted that the IW results showed a small, but marked step at $t^* = 547.1$. Since it occurred well after the quenching instance, we did not make further investigations. However, it was observed that at this instance, the flow velocity was reduced towards zero in most of the domain and had changed direction close to the wall.

The detailed temporal development of the entropy generation and its main components through quenching is shown in Fig. 6 for PW. Contributions from selected elementary reactions are shown in Fig. 7. It can be noted that the ordinates of these graphs are dimensional, while the non-dimensional distance and time are retained from Ref. [2] for easier comparison. The corresponding results for IW are shown in Figs. 8 and 9. It was seen that the diffusion contribution became lower, both absolutely and relatively, when the flame came close to the wall. Hence, the species concentrations gradients were reduced towards quenching.

Effects of fuel-air ratio

The investigations were conducted for a lean ($\phi_u = 0.5$) and a rich ($\phi_u = 1.5$) mixture, in addition to the stoichiometric cases in the preceding section. The total entropy generation rate and its components were integrated over the spatial domain, $\int_0^L \sigma(x,t) dx$, as described above. This transient quantity was then multiplied

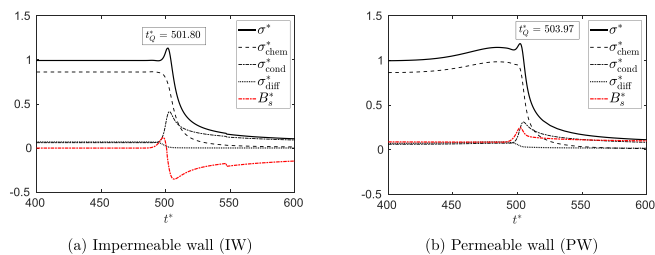


Fig. 3 – Entropy generation rate components and entropy diffusion integrated over the length of the domain as a function of time, $\phi_u = 1.0$, $T_u = 750$ K. Values are made non-dimensional with the integral of the total entropy generation through the free propagating flame.

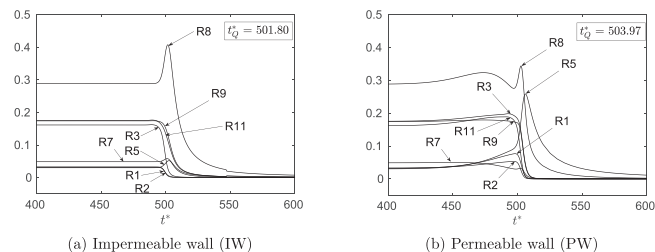


Fig. 4 – Entropy generation rate components due to some elementary reactions, integrated over the length of the domain as a function of time, $\phi_u = 1.0$, $T_u = 750$ K. Values are made non-dimensional with the integral of the total entropy generation through the free propagating flame.

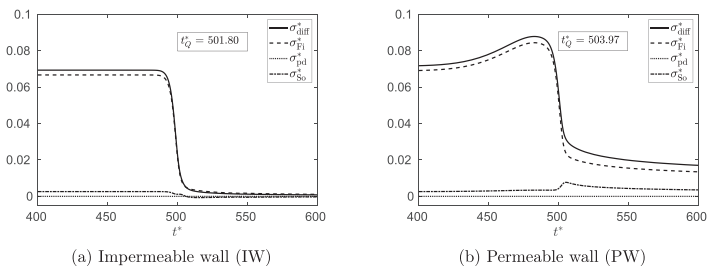


Fig. 5 – Entropy generation rate due to mass diffusion and its components integrated over the length of the domain as a function of time, permeable wall, $\phi_u = 1.0$, $T_u = 750$ K. Values are made non-dimensional with the integral of the total entropy generation through the free propagating flame.

with the ambient temperature, T_0 , to provide the exergy destruction rate (ED) in the domain at each timestep. These results are shown in Fig. 10. Also shown is the rate of conversion of H_2 chemical exergy (CE), that is, $\epsilon_{H_2}^{ch} \cdot \int_0^L (-\dot{\omega}_{H_2}(x, t))dx$. This comparison was found relevant, since IW and PW had different amounts of fuel, due to permeation through the wall. Although H_2 alone did not give the complete image of the chemical conversion, it gave a clear indication. For a comparison between the different mixtures, the integrated rates are shown as

dimensional quantities. For convenience, the chemical-exergy conversion rates were scaled by a factor of 0.2 in the graphs.

As observed previously [1,2], the conductive heat flux for the IW configuration varied notably with the equivalence ratio near quenching. This also led to a strong variation in the corresponding entropy generation rate. As seen in Fig. 10a for the rich case, the conduction component was the largest contributor at quenching. For the stoichiometric and lean IW cases, this component was notably smaller, both relatively

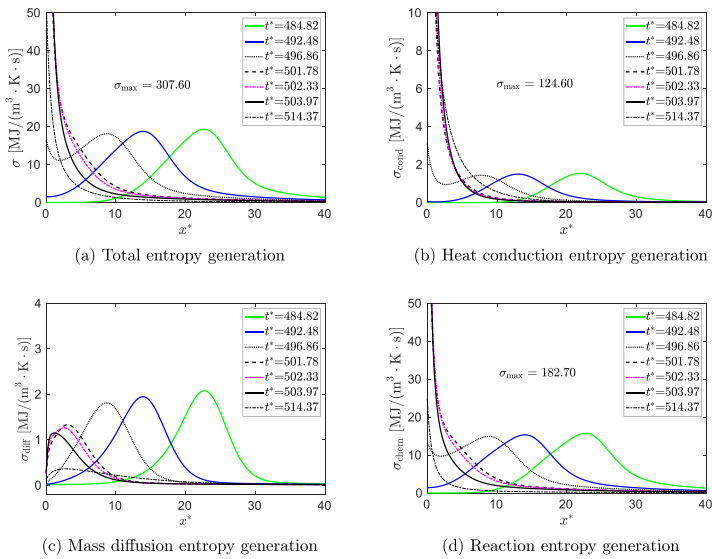


Fig. 6 – Entropy generation rates vs. distance from wall for various time. Permeable wall, $\phi_u = 1.0$, $T_u = 750$ K.

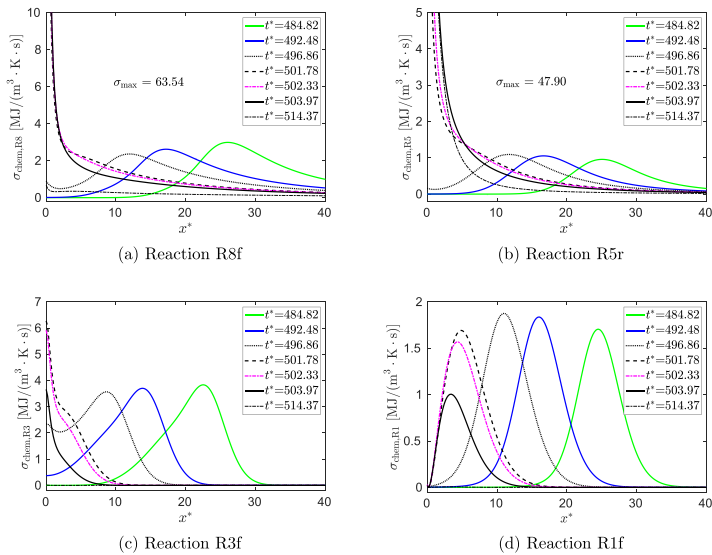


Fig. 7 – Entropy generation rates vs. distance from wall for various time for selected elementary reactions. Permeable wall, $\phi_u = 1.0$, $T_u = 750$ K.

and absolutely. While the conduction component peaked, the chemical and diffusive components just faded off at quenching for all stoichiometries.

For the PW configuration, the peak of conductive heat flux at quenching did not show much variation with equivalence ratio. It was slightly reduced with increasing

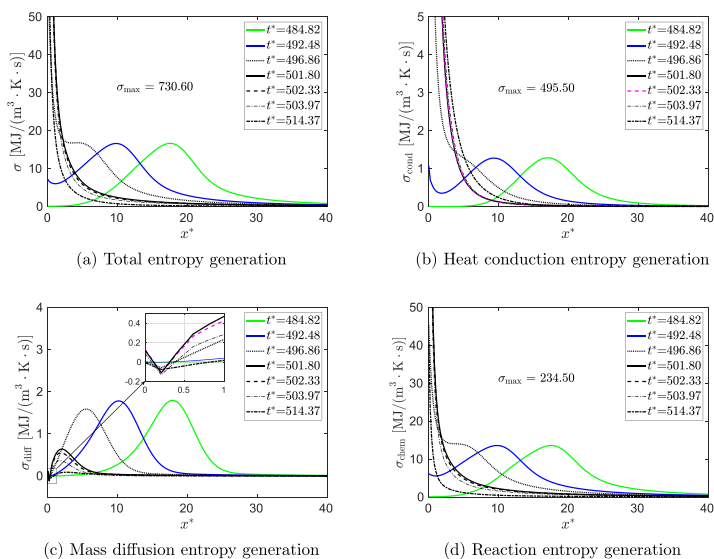


Fig. 8 – Entropy generation rates vs. distance from wall for various time. Impermeable wall, $\phi_u = 1.0$, $T_u = 750$ K.

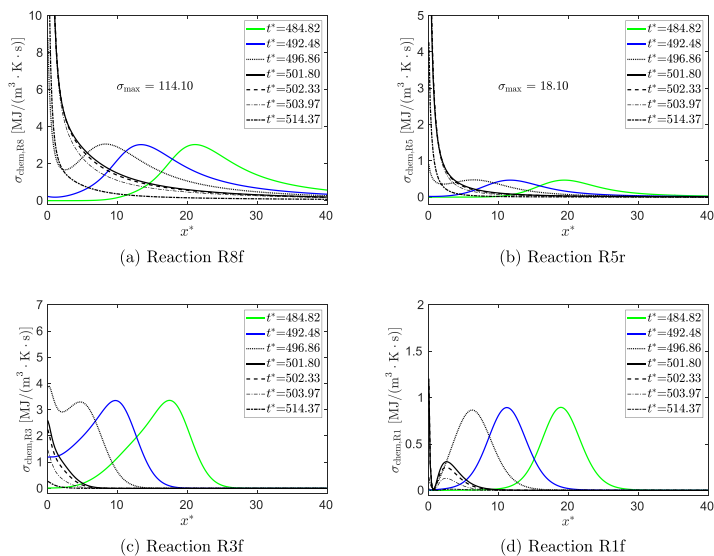


Fig. 9 – Entropy generation rates vs. distance from wall for various time for selected elementary reactions. Impermeable wall, $\phi_u = 1.0$, $T_u = 750$ K.

equivalence ratio, similar to the wall heat flux (displayed in Ref. [1]). On the other hand, the chemical component of entropy generation showed more variation, in particular, between the lean case and the stoichiometric and rich

cases. For the lean case, and to some extent the stoichiometric case, a higher content of fuel close to the hydrogen-permeable wall led to an increased chemical conversion and more entropy generation. Therefore, the chemical

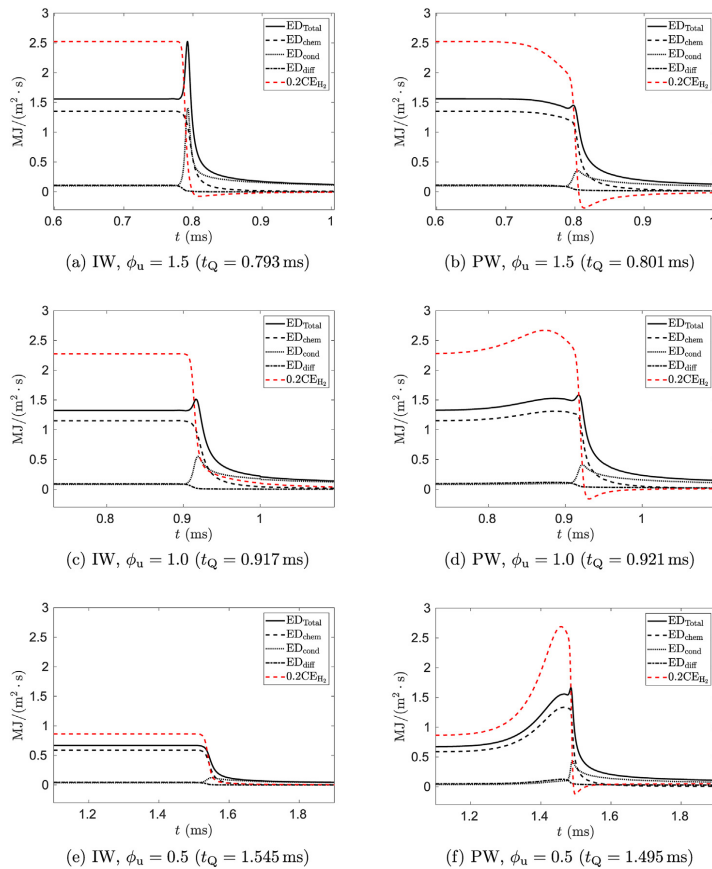


Fig. 10 – Exergy destruction (ED) rate components and hydrogen chemical exergy conversion (CE) rate (notice scale), integrated over the length of the domain as a function of time for $T_u = 750$ K and different equivalence ratios.

component of entropy generation increased as the flame approached the wall. Close to the quenching instance, the chemical component of these cases also decreased and eventually faded off. In comparison, the conductive component had a slower fade off after quenching, and it became the biggest contributor to entropy generation in the weakly reacting mixture after quenching.

For all these cases, the already modest diffusive component of entropy generation faded off before quenching.

Inspecting the contributions of individual elementary reactions, the overall view was to some extent similar to the stoichiometric case, Fig. 4. However, some deviations were noted. For the free propagating flame, the rich case was not very different from the stoichiometric. The most important reaction was R8f, followed by R11f, R3f and R9f. Also R5r, R1f and R2f had notable contributions. All these reactions had a moderately larger entropy generation in

the rich case. In the lean case, the contributions were considerably lesser. In particular, R8 was reduced to one-third compared to stoichiometric case, falling below R9 and R11.

When the flame approached the impermeable wall (IW) for the rich case, R8 and R5 had spikes similar to the stoichiometric case. The other chemical contributions declined before these spikes, and the sum of chemical contributions faded off, as seen in Fig. 10a. For the lean case, all important reactions just faded off.

For the permeable wall (PW) rich case, R8 began decreasing some time before quenching, before it got a peak close to quenching. For the other reactions, the behaviour was similar to that of the stoichiometric case. In the lean case, the reactions mentioned (R11f, R3f, R9f, R5r, R1f, R2f) had an increase when the flame approached the wall. In particular, R8 rose to a level like that of the stoichiometric case. For all PW

cases, and to lesser extent the rich IW case, R5 showed a strong increase in entropy generation just before quenching, when other reactions decreased. For these cases, R5 remained the largest contributor after quenching, although at a much lower level. The negative H_2 consumption seen in Fig. 10 can be associated with the reverse R5 recombining $2H$ into H_2 .

As noted in the Introduction, previous studies on non-premixed and some partially premixed flames had found the conduction to be the largest contributor to entropy generation. For premixed flames, chemical reactions have been found to dominate. On this background, it is worth noting that the permeation of hydrogen from the wall, i.e. a non-premixed supply of fuel, can increase the weight of the chemical reactions in entropy generation.

Effects on the entropy diffusion flux B_s , Eq. (15), are shown in Fig. 11 presented as $\int_0^L B_s dx$. As in Fig. 4, the values were made non-dimensional with the integral of the total entropy generation through the free propagating stoichiometric flame. It was seen that the entropy flux was virtually zero in the free propagating flame (cf. Table 2). For IW, the lean flame had a flux towards the wall (i.e. negative) when approaching quenching. With increasing fuel-air ratio, a period with positive flux appeared shortly before quenching. In the $\phi_u = 1.5$ case, this became the main effect. For PW, the permeating fuel gave a positive (non-zero) entropy flux near the wall for the entire period, with a strong increase just before quenching.

For an overall comparison, the spatially integrated exergy destruction rate was also integrated for a time interval ending at the quenching instance:

$$ED = T_0 \int_{t_1}^{t_0} \int_0^L \sigma(x, t) dx dt \quad (25)$$

For PW, the integral was taken from the time t_1 , where the wall permeation began affecting the flame (beginning of “Stage II”, cf [2]). For IW, t_1 was chosen so that the time interval $(t_0 - t_1)$ had the same value for each pair of IW and PW cases. The exergy destruction, Eq. (25), can be compared with the exergy of the converted fuel in the same interval, $CE = \epsilon_{H_2}^{ch} \cdot \int_{t_1}^{t_0} \int_0^L (-\dot{\omega}_{H_2}(x, t)) dx dt$.

The fraction of entropy generation due to conduction increased for IW with increasing equivalence ratio, from 5.9%

for $\phi_u = 0.5$ and 6.7% for $\phi_u = 1.0$, to 10% for $\phi_u = 1.5$. The diffusion fraction had a maximum at 7.1% at stoichiometric conditions, with a small reduction for rich and lean. The chemistry dominated ($\approx 86\%$) and had a slightly reduced share with increasing equivalence ratio. Compared with the H_2 chemical exergy conversion (CE), Fig. 12, all components of exergy destruction had a minimum at stoichiometric conditions. The conduction and diffusion components had small increases for rich and lean mixtures, while the chemical term increased most notably for lean conditions. For the PW configuration, the variations were similar to, but less than those of IW.

From Eq. (18), showing σ_{cond} inversely proportional to the square of the temperature, an increase in this component was expected at a reduced temperature. On the contrary, the diffusion component, Eqs. (20) and (22), does not have a direct relation to temperature. The chemical component, Eq. (21), is inversely proportional to the temperature, and proportional to the reaction rate involving an exponential function. The latter relation will also affect the fuel conversion. Since the reaction Gibbs energy difference varies more with temperature than the corresponding enthalpy difference, the entropy generation variation differs from that of the heat release.

Our previous results [1,2] showed that for IW, the lean flame had lower temperatures, while the rich flame had approximately

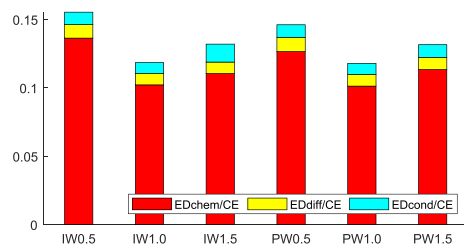


Fig. 12 – Effect of equivalence ratio: Components of exergy destruction (ED) in the domain for a time interval up to quenching as fractions of the converted fuel chemical exergy (CE), $T_u = T_w = 750$ K.

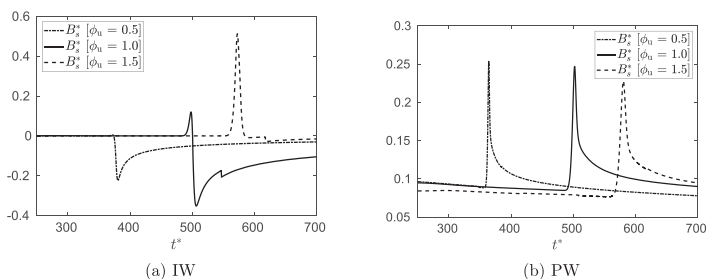


Fig. 11 – Entropy diffusion rate integrated over the length of the domain as a function of time, $T_u = 750$ K at different equivalence ratios. Values are made non-dimensional with the integral of the total entropy generation through the free propagating flame for $\phi_u = 1.0$.

the same temperatures as the stoichiometric. For PW, the permeation led to a higher local equivalence ratio close to the wall. The (initially) lean and stoichiometric mixtures gave similar temperatures, while the rich flame got lower values. Compared to IW, the lean PW case had higher temperatures, the stoichiometric case was on par with IW, while for the rich mixture the temperatures were lower than for IW.

The entropy generation caused by the isothermal expansion of H_2 through the membrane, from the feed pressure (10 atm) to the partial pressure on the permeate side, was not included in the results above. It was estimated to approximately 1% of the total entropy generation.

Effects of mixture temperature

Both configurations, with rich, stoichiometric and lean mixtures, were computed with temperatures of the unburnt mixture and the wall ($T_u = T_w$) at 500 K and 300 K [2].

The exergy destruction for the domain and the time interval was compared with the chemical exergy of the converted fuel, as described above. The results are shown in Fig. 13. It was seen that lower temperatures gave larger values both for the total and the components of exergy destruction. The fraction due to diffusion was slightly larger at lower temperatures, while the conduction fraction of total entropy generation increased considerably (from 7% at 750 K to 25% at 300 K, stoichiometric). The variations with equivalence ratio were similar to those at the higher temperature in the preceding section.

Effects of dilution with nitrogen or water vapour

The stoichiometric cases at 750 K (Case D0, IW and PW as above) were diluted by increasing the unburnt-mixture nitrogen-oxygen molar ratio from 3.762 (undiluted Case D0, with no H_2O) to 4.0 (Case D1) and 4.762 (Case D2), for both configurations. Furthermore, water vapour was added such that the H_2O-O_2 ratio of the unburnt mixture increased from zero (Case D0) to 0.12 (Case D3) and 3.147 (Case D4), as described in Ref. [2].

Basically, dilution will reduce the reaction temperatures and the effects can be expected similar to those of the reduced temperature in the preceding section.

The exergy destruction integrated over the domain and the time interval was compared with the chemical exergy of the converted fuel, as described above. The results are shown in Fig. 14.

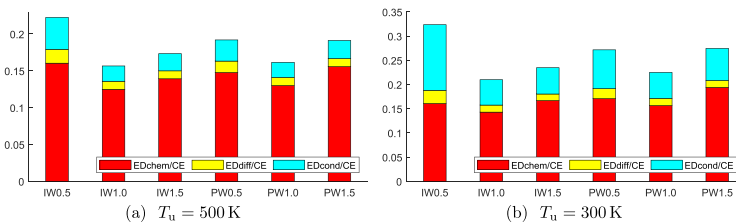


Fig. 13 – Effect of unburnt temperature: Components of exergy destruction (ED) in the domain for a time interval up to quenching as fractions of the correspondingly converted fuel chemical exergy (CE).

Dilution with (inert) N_2 (Cases D1 and D2) gave modest increases in total exergy destruction as fraction of converted fuel exergy and in the chemical component. Dilution with H_2O had a different effect for the smaller amount (Cases D3). Then, the chemical component (relative to converted fuel exergy) was reduced. The reasons seemed to be that some additional H_2O gave an increased conversion of fuel (H_2). Further dilution with more vapour (Cases D4) had the same effect as dilution with N_2 , i.e. modest increases. The effects were similar for both configurations.

Permeable vs. impermeable wall

The entropy generation primarily followed inversely the temperature. Lower unburnt-mixture temperature, deviation from stoichiometry and dilution all gave lower temperatures and higher total entropy generation and exergy destruction per unit of converted fuel.

The effects of fuel permeation were more complex. It had a cooling effect close to the wall due to thermal dilution [1,3]. Entering a lean mixture, additional fuel gave increased fuel conversion and a higher temperature near the wall. The higher temperature due to reaction heat release was more pronounced on entropy generation than the cooling effect. When fuel permeated into an initially stoichiometric or rich mixture, the local mixture became richer. Therefore, the temperature was lowered, and the entropy generation increased.

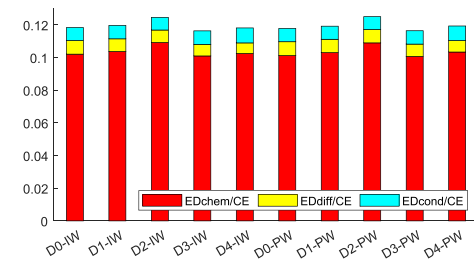


Fig. 14 – Effect of dilution: Components of exergy destruction (ED) in the domain for a time interval up to quenching as fractions of the correspondingly converted fuel chemical exergy (CE).

The main contributions to entropy generation were reactions and conduction. Diffusion had, in general, a minor impact. Even though permeation influenced diffusion, the effect of this on entropy generation was small.

The investigations of permeable walls are motivated by, among other, potential emissions reduction and efficiency improvement. The permeation zone will be a smaller part of a combustor. When incomplete fuel conversion occurs, it will be a localized phenomenon, and the conversion can be completed elsewhere in the combustor. Accordingly, the primary interest will be to observe the entropy generation per unit of converted fuel. Permeating fuel increased the entropy generation because the fuel conversion increased. The entropy generation per unit of converted fuel was either decreased (lean mixtures) or marginally affected (stoichiometric or rich mixtures) by permeation.

Conclusions

Previous investigations [1,2] on 1-D head-on premixed H_2 -air flame interacting with an impermeable wall (IW) or a permeable wall (PW) were extended with computations of entropy generation and entropy fluxes. Additional fuel was supplied through the permeable wall.

In general, fuel permeation through the wall increased both entropy generation and fuel conversion.

The permeating fuel had a diversity of effects. First, it had a cooling effect close to the wall. Separately, this thermal dilution reduced the local temperature and contributed to increased entropy generation. However, for initially lean and stoichiometric mixtures, the additional fuel provided more reaction heat release, leading to higher temperature and reduced entropy generation per unit of converted fuel. Permeation also increased the mass flux, and thereby the entropy flux, away from the wall. The effects of mass diffusion on entropy generation were modest, and the altered mass diffusion made small changes from IW to PW. The Soret diffusion (thermodiffusion) had small contribution to the mass diffusion entropy generation. During quenching it became even smaller for IW, while it had an increase for PW. The effects of pressure diffusion were negligible.

The effects of permeation were similar for all unburnt-temperatures investigated (750 K, 500 K, 300 K). As expected from theory and other studies, a lower temperature gave higher entropy generation. Furthermore, in accordance with literature, the chemical reaction gave the major part of entropy generation, with conduction as the second most important source. Mass diffusion was of modest importance, while viscous forces had vanishing effects.

Permeation to a lean mixture reduced entropy generation per unit of fuel converted. The effect was stronger for lower temperatures because then the conduction had a greater share of the total entropy generation. At the higher unburnt-mixture temperature, similar results were seen for rich mixtures, as well. For the lower temperature, permeation into a rich mixture increased the entropy generation per unit of converted fuel.

The elementary reactions most important for entropy generation towards quenching were R8 ($OH + H + M \rightleftharpoons H_2O + M$, net forward), R5 ($H_2 + M \rightleftharpoons 2H + M$, net reverse) and

R3 ($OH + H_2 \rightleftharpoons H + H_2O$, net forward). In particular, the recombining R5r had a notable relative increase towards the quenching instance. Both R8f and R5r had high peaks of entropy generation rate when the flame reached the wall and quenched.

Declaration of competing interest

The authors declare that they have no known competing financial interests or personal relationships that could have appeared to influence the work reported in this paper.

Acknowledgments

We are grateful to the Norwegian e-infrastructure for Research and Education (Uninett Sigma2 AS) for providing the HPC computational resources and useful technical support (project No. NN9400K).

Nomenclature

A_j	factor in reaction-rate model, reaction j
B_s	entropy diffusion term ($J/(s \cdot m^3 \cdot K)$)
$C_p, C_{p,i}$	specific heat capacity at constant pressure (for species i) ($J/(kg \cdot K)$)
d_{ai}	diffusion driving force of species i in x_α direction (m^{-1})
D_i^{mix}	mixture-averaged mass diffusivity of species i (m^2/s)
D_i^T	thermal diffusion coefficient of species i ($kg/(ms)$)
e	specific internal energy (J/kg)
E_j	activation energy in reaction j ($J/(mol \cdot K)$)
g_i	specific chemical potential (Gibbs function) for species i (J/kg)
h_i	specific enthalpy for species i (J/kg)
J_{ai}	diffusive mass flux of species i in x_α direction ($kg/(s \cdot m^2)$)
k_{fj}, k_{rj}	forward, reverse rate coefficients of reaction j
K_{cj}	equilibrium constant of reaction j (–)
L	length of domain (m)
N_R	number of reactions (–)
N_S	number of species (–)
p, p_{ref}	pressure, reference pressure (Pa)
q_j	reaction progress of elementary reaction j ($mol/(m^3 s)$)
q_α	heat flux in x_α direction ($J/(s \cdot m^2)$)
R_u	universal gas constant ($J/(mol \cdot K)$)
s, s_i	specific entropy ($J/(kg \cdot K)$)
s_i°	specific entropy at reference pressure ($J/(kg \cdot K)$)
S_L^0	laminar flame speed (m/s)
t	time (s)
T, T_0	temperature, ambient temperature (K)
u_α	velocity component in x_α direction (m/s)
V_{ai}	mass diffusion velocity of species i in x_α direction (m/s)
W_i	molar mass of species i (kg/mol)
x, x_α	spatial coordinate (m)

X_i	mole fraction of species i (–)
Y_i	mass fraction of species i (–)
β_j	exponent in reaction-rate model, reaction j (–)
$\delta_{\alpha\beta}$	Kronecker delta (–)
δ_L	Laminar flame thickness (m)
ϵ_i^{ch}	chemical specific exergy for species i (kJ/kg)
λ	thermal conductivity (J/(s·m·K))
μ	viscosity (Pa·s)
ν_{ij}	reaction coefficient of species i in reaction j (–)
ν_{ij}', ν_{ij}''	reaction coefficients of species i (reactant, product) in reaction j (–)
ρ	mass density (kg/m ³)
σ	volumetric entropy generation rate (J/(s·m ³ ·K))
$\tau_{\alpha\beta}$	viscous stress tensor (Pa)
ω_i	volumetric molar reaction rate of species i (mol/(m ³ s))
Superscripts/Subscripts	
*	non-dimensional
Du	Dufour
Fi	Fick (species gradient diffusion)
Fo	Fourier (thermal gradient conduction)
J	mass diffusion
pd	pressure diffusion
Q	quenching
So	Soret

REFERENCES

- Gruber A, Salimath PS, Chen JH. Direct numerical simulation of laminar flame-wall interaction for a novel H₂-selective membrane/injector configuration. *Int J Hydrogen Energy* 2014;39(11):5906–18. <https://doi.org/10.1016/j.ijhydene.2014.01.148>.
- Salimath PS, Ertesvåg IS, Gruber A. Premixed hydrogen–air flames interacting with a hydrogen porous wall. *Int J Hydrogen Energy* 2018;43(7):3822–36. <https://doi.org/10.1016/j.ijhydene.2017.12.166>.
- Salimath PS, Ertesvåg IS, Gruber A. Computational analysis of premixed methane–air flame interacting with a solid wall or a hydrogen porous wall. *Fuel* 2020;272:117658. <https://doi.org/10.1016/j.fuel.2020.117658>.
- Szargut J, Morris DR, Steward FR. Exergy analysis of thermal, chemical, and metallurgical processes. New York: Hemisphere; 1988.
- Kotas TJ. The exergy method for thermal plant analysis. London, UK: Butterworths; 1985.
- Rian AB, Ertesvåg IS. Exergy analysis of a steam production and distribution system including alternatives to throttling and the single pressure steam production. *Energy Convers Manag* 2011;52(1):703–12. <https://doi.org/10.1016/j.enconman.2010.07.049>.
- Ertesvåg IS. Exergy calculations based on a fixed standard reference environment vs. the actual ambient conditions: gas turbine and fuel cell examples. *Int J Exergy* 2015;16(2):239–61. <https://doi.org/10.1504/IJEX.2015.068209>.
- Som SK, Datta A. Thermodynamic irreversibilities and exergy balance in combustion processes. *Prog Energy Combust Sci* 2008;34(3):351–76. <https://doi.org/10.1016/j.peccs.2007.09.001>.
- Arpaci VS, Selamet A. Entropy production in flames. *Combust Flame* 1988;73(3):251–9. [https://doi.org/10.1016/0010-2180\(88\)90022-3](https://doi.org/10.1016/0010-2180(88)90022-3).
- Nishida K, Takagi T, Kinoshita S. Analysis of entropy generation and energy loss during combustion. *Proc Combust Inst* 2002;29(1):869–74. [https://doi.org/10.1016/S1540-7489\(02\)80111-0](https://doi.org/10.1016/S1540-7489(02)80111-0).
- Zhang J, Han D, Huang Z. Second-law thermodynamic analysis for premixed hydrogen flames with diluents of argon/nitrogen/carbon dioxide. *Int J Hydrogen Energy* 2019;44(10):5020–9. <https://doi.org/10.1016/j.ijhydene.2019.01.041>.
- Acampora L, Marra FS. Second law thermodynamic analysis of syngas premixed flames. *Int J Hydrogen Energy* 2020;45(21):12185–202. <https://doi.org/10.1016/j.ijhydene.2020.02.142>.
- Liu D, Wang H, Zhang Y, Liu H, Zheng Z, Yao M. On the entropy generation and exergy loss of laminar premixed flame under engine-relevant conditions. *Fuel* 2021;283:119245. <https://doi.org/10.1016/j.fuel.2020.119245>.
- Chen S. Analysis of entropy generation in counter-flow premixed hydrogen–air combustion. *Int J Hydrogen Energy* 2010;35(3):1401–11. <https://doi.org/10.1016/j.ijhydene.2009.11.080>.
- Jejurkar SY, Mishra DP. Effects of wall thermal conductivity on entropy generation and exergy losses in a H₂–air premixed flame microcombustor. *Int J Hydrogen Energy* 2011;36(24):15851–9. <https://doi.org/10.1016/j.ijhydene.2011.08.116>.
- Jejurkar SY, Mishra DP. Numerical analysis of entropy generation in an annular microcombustor using multistep kinetics. *Appl Therm Eng* 2013;52(2):394–401. <https://doi.org/10.1016/j.applthermaleng.2012.12.021>.
- Jiang D, Yang W, Chua KJ. Entropy generation analysis of H₂/air premixed flame in microcombustors with heat recuperation. *Chem Eng Sci* 2013;98:265–72. <https://doi.org/10.1016/j.ces.2013.05.038>.
- Li Z, Chou S, Shu C, Yang W. Entropy generation during microcombustion. *J Appl Phys* 2005;97(8):084914. <https://doi.org/10.1063/1.1876573>.
- Jiang D, Yang W, Teng J. Entropy generation analysis of fuel lean premixed CO/H₂/air flames. *Int J Hydrogen Energy* 2015;40(15):5210–20. <https://doi.org/10.1016/j.ijhydene.2015.02.082>.
- Zuo W, Zhang Y, Li J, Li Q, He Z. A modified micro reactor fueled with hydrogen for reducing entropy generation. *Int J Hydrogen Energy* 2019;44(51):27984–94. <https://doi.org/10.1016/j.ijhydene.2019.09.009>.
- Wang W, Zuo Z, Liu J, Yang W. Entropy generation analysis of fuel premixed CH₄/H₂/air flames using multistep kinetics. *Int J Hydrogen Energy* 2016;41(45):20744–52. <https://doi.org/10.1016/j.ijhydene.2016.08.103>.
- Datta A. Entropy generation in a confined laminar diffusion flame. *Combust Sci Technol* 2000;159:39–56. <https://doi.org/10.1080/00102200008935776>.
- Stanciu D, Isvoranu D, Marinescu M, Gogus Y. Second law analysis of diffusion flames. *Int J Therm* 2001;4(1):1–18.
- Datta A. Effects of gravity on structure and entropy generation of confined laminar diffusion flames. *Int J Therm Sci* 2005;44:429–40. <https://doi.org/10.1016/j.ijthermalsci.2004.10.003>.
- Chen S, Liu Z, Liu J, Li J, Wang L, Zheng C. Analysis of entropy generation in hydrogen-enriched ultra-lean counter-flow methane–air non-premixed combustion. *Int J Hydrogen Energy* 2010;35(22):12491–501. <https://doi.org/10.1016/j.ijhydene.2010.08.048>.
- Briones AM, Mukhopadhyay A, Aggarwal SK. Analysis of entropy generation in hydrogen-enriched methane–air propagating triple flames. *Int J Hydrogen Energy* 2009;34(2):1074–83. <https://doi.org/10.1016/j.ijhydene.2008.09.103>.
- Chen S, Han H, Liu Z, Li J, Zheng C. Analysis of entropy generation in non-premixed hydrogen versus heated air

- counter-flow combustion. *Int J Hydrogen Energy* 2010;35:4736–46. <https://doi.org/10.1016/j.ijhydene.2010.02.113>.
- [28] Raghavan V, Gogos G, Babu V, Sundararajan T. Entropy generation during the quasi-steady burning of spherical fuel particles. *Int J Therm Sci* 2007;46:589–604. <https://doi.org/10.1016/j.ijthermalsci.2006.07.006>.
- [29] Pope DN, Raghavan V, Gogos G. Gas-phase entropy generation during transient methanol droplet combustion. *Int J Therm Sci* 2010;49:1288–302. <https://doi.org/10.1016/j.ijthermalsci.2010.02.012>.
- [30] Farran R, Chakraborty N. A direct numerical simulation-based analysis of entropy generation in turbulent premixed flames. *Entropy* 2013;15(5):1540–66. <https://doi.org/10.3390/e15051540>.
- [31] Ertesvåg IS, Kolbu J. Entropy Production modeling in CFD of turbulent combustion flow. In: Kjelstrup S, et al., editors. *Proc. ECOS 2005 18th Int. Conf. On efficiency, cost, optimization, simulation and environmental impact of energy systems*, Trondheim 20–22 June 2005. Trondheim, Norway: Tapir Academic Press; 2005. p. 265–72.
- [32] Emadi A, Emami MD. Analysis of entropy generation in a hydrogen-enriched turbulent non-premixed flame. *Int J Hydrogen Energy* 2013;38(14):5961–73. <https://doi.org/10.1016/j.ijhydene.2013.02.115>.
- [33] Gholamalizadeh E, Alimoradi A, Saeed AD, Amiri A, Moghaddam MG. Study of the heat transfer characteristics and entropy generation rate for the reacting flows inside tubes. *Appl Therm Eng* 2019;149:1435–44. <https://doi.org/10.1016/j.applthermaleng.2018.12.119>.
- [34] Rajabi V, Amani E. A computational study of swirl number effects on entropy generation in gas turbine combustors. *Heat Tran Eng* 2019;40(3–4):346–61. <https://doi.org/10.1080/01457632.2018.1429056>.
- [35] Marble F, Candel S. Acoustic disturbance from gas non-uniformities convected through a nozzle. *J Sound Vib* 1977;55(2):225–43. [https://doi.org/10.1016/0022-460X\(77\)90596-X](https://doi.org/10.1016/0022-460X(77)90596-X).
- [36] Magri L, O'Brien J, Ihme M. Compositional inhomogeneities as a source of indirect combustion noise. *J Fluid Mech* 2016;799:R4. <https://doi.org/10.1017/jfm.2016.397>.
- [37] Bazdidi-Tehrani F, Abedinejad MS, Mohammadi M. Analysis of relationship between entropy generation and soot formation in turbulent kerosene/air jet diffusion flames. *Energy Fuels* 2019;33(9):9184–95. <https://doi.org/10.1021/acs.energyfuels.9b01671>.
- [38] Kooshkbaghi M, Frouzakis CE, Boulouchos K, Karlin IV. Entropy production analysis for mechanism reduction. *Combust Flame* 2014;161(6):1507–15. <https://doi.org/10.1016/j.combustflame.2013.12.016>.
- [39] Porras S, Bykov V, Gol'dshtein V, Maas U. Joint characteristic timescales and entropy production analyses for model reduction of combustion systems. *Entropy* 2017;19(6):264. <https://doi.org/10.3390/e19060264>.
- [40] Ream AE, Slattery JC, Cizmas PG. A method for generating reduced-order combustion mechanisms that satisfy the differential entropy inequality. *Phys Fluids* 2018;30(4):043601. <https://doi.org/10.1063/1.5022691>.
- [41] Sadiki A, Hutter K. On thermodynamics of turbulence: development of first order closure models and critical evaluation of existing models. *J. Non-Equil. Thermodyn.* 2000;25:131–60. <https://doi.org/10.1515/JNETDY.2000.009>.
- [42] Ahmadi G, Cao J, Schneider L, Sadiki A. A thermodynamical formulation for chemically active multiphase turbulent flows. *Int J Eng Sci* 2006;44:699–720. <https://doi.org/10.1016/j.jengsci.2006.06.001>.
- [43] Chen J, Choudhary A, de Supinski B, DeVries M, Hawkes E, Klasky S, Liao W, Ma K, Mellor-Crummey J, Podhorski N, Sankaran R, Shende S, Yoo C. Terascale direct numerical simulations of turbulent combustion using S3D. *Comput Sci Discov* 2009;2(1):15001. <https://doi.org/10.1088/1749-4699/2/1/015001>.
- [44] Haase R. *Thermodynamics of irreversible processes*. Reading, Massachusetts: Addison-Wesley; 1963.
- [45] de Groot S, Mazur P. *Non-equilibrium thermodynamics*. New York: Dover Publications; 1984.
- [46] Kee RJ, Dixon-Lewis G, Miller JA. A fortran computer code package for the evaluation of gas-phase multicomponent transport properties. SANDIA Rep. No. SAND86-8246, Sandia National Laboratories, Livermore, CA. 1986.
- [47] Kee RJ, Dixon LG, Warnatz J, Coltrin ME, Miller JA, Moffat HK. A fortran chemical kinetics package for the analysis of gas-phase chemical kinetics. In: *Tech. Rep., release 3.5*. San Diego, CA: Reaction Design Inc.; 1999.
- [48] Ertesvåg IS. Sensitivity of the chemical exergy for atmospheric gases and gaseous fuels to variation in ambient conditions. *Energy Convers Manag* 2007;48:1983–95. <https://doi.org/10.1016/j.enconman.2007.01.005>.
- [49] Echehki T, Chen JH. Direct numerical simulation of autoignition in non-homogeneous hydrogen-air mixtures. *Combust Flame* 2003;134(3):169–91. [https://doi.org/10.1016/S0010-2180\(03\)00088-9](https://doi.org/10.1016/S0010-2180(03)00088-9).
- [50] Sankaran R, Hawkes ER, Chen JH, Lu TF, Law CK. Direct numerical simulations of turbulent lean premixed combustion. *J. Phys. Conf. Series* 2006;46(1):38–42. <https://doi.org/10.1088/1742-6596/46/1/004>.
- [51] Gruber A, Sankaran R, Hawkes ER, Chen JH. Turbulent flame wall interaction: a direct numerical simulation study. *J Fluid Mech* 2010;658:5–32. <https://doi.org/10.1017/S0022112010001278>.
- [52] Grout RW, Gruber A, Yoo CS, Chen JH. Direct numerical simulation of flame stabilization downstream of a traverse fuel jet in cross-flow. *Proc Combust Inst* 2011;33(1):1629–37. <https://doi.org/10.1016/j.proci.2010.06.013>.
- [53] Hawkes ER, Sankaran R, Sutherland JC, Chen JH. Scalar mixing in DNS of temporally-evolving plane jet flames with detailed CO/H₂ kinetics. *Proc Combust Inst* 2007;31(1):1633–40. <https://doi.org/10.1016/j.proci.2006.08.079>.
- [54] Lignell DO, Chen JH, Smith PJ, Lu T, Law CK. The effect of flame structure on soot formation and transport in turbulent nonpremixed flames using direct numerical simulation. *Combust Flame* 2007;151(1–2):2–28. <https://doi.org/10.1016/j.combustflame.2007.05.013>.
- [55] Kennedy CA, Carpenter MH. Several new numerical methods for compressible shear layer simulations. *Appl Numer Math* 1994;14(804):397. [https://doi.org/10.1016/0168-9274\(94\)00004-2](https://doi.org/10.1016/0168-9274(94)00004-2).
- [56] Kee RJ, Rupley FM, Miller JA. CHEMKIN-II: a FORTRAN chemical kinetics package for the analysis of gas phase chemical kinetics. SANDIA Rep 1989-3–164. No. SAND89-8009B.
- [57] Li J, Zhao Z, Kazakov A, Dryer FL. An updated comprehensive kinetic model of hydrogen combustion. *Int J Chem Kinet* 2004;36(10):566–75. <https://doi.org/10.1002/kin.20026>.
- [58] Torabi M, Torabi M, Peterson GPB. Entropy generation of double diffusive forced convection in porous channels with thick walls and Soret effect. *Entropy* 2017;19(4):171. <https://doi.org/10.3390/e19040171>.

B Chemical kinetics mechanism

Hydrogen–air chemical mechanism

Table 1: Elementary reactions in the H₂-air chemical mechanism with rate coefficients $k_f = AT^\beta \exp(-E_0/RT)$ [64].

No.	Reaction	A	β	E_0
R1	$\text{O}_2 + \text{H} \rightleftharpoons \text{OH} + \text{O}$	3.547E+15	-0.406	16599.0
R2	$\text{H}_2 + \text{O} \rightleftharpoons \text{OH} + \text{H}$	0.508E+05	2.67	6290.0
R3	$\text{OH} + \text{H}_2 \rightleftharpoons \text{H} + \text{H}_2\text{O}$	0.216E+09	1.51	3430.0
R4	$\text{H}_2\text{O} + \text{O} \rightleftharpoons 2\text{OH}$	2.970E+06	2.02	13400.0
R5	$\text{H}_2 + \text{M} \rightleftharpoons 2\text{H} + \text{M}$	4.577E+19	-1.40	104380.0
R6	$2\text{O} + \text{M} \rightleftharpoons \text{O}_2 + \text{M}$	6.165E+15	-0.50	0.0
R7	$\text{H} + \text{O} + \text{M} \rightleftharpoons \text{OH} + \text{M}$	4.714E+18	-1.00	0.0
R8	$\text{OH} + \text{H} + \text{M} \rightleftharpoons \text{H}_2\text{O} + \text{M}$	3.800E+22	-2.00	0.0
R9	$\text{O}_2 + \text{H} + \text{M} \rightleftharpoons \text{HO}_2 + \text{M}$	1.475E+12	0.60	0.0
R10	$\text{H} + \text{HO}_2 \rightleftharpoons \text{O}_2 + \text{H}_2$	1.660E+13	0.00	823.0
R11	$\text{H} + \text{HO}_2 \rightleftharpoons 2\text{OH}$	7.079E+13	0.00	295.0
R12	$\text{O} + \text{HO}_2 \rightleftharpoons \text{OH} + \text{O}_2$	0.325E+14	0.00	0.0
R13	$\text{OH} + \text{HO}_2 \rightleftharpoons \text{O}_2 + \text{H}_2\text{O}$	2.890E+13	0.00	-497.0
R14	$2\text{HO}_2 \rightleftharpoons \text{O}_2 + \text{H}_2\text{O}_2$	4.200E+14	0.00	11982.0
R15	$\text{H}_2\text{O}_2 + \text{M} \rightleftharpoons 2\text{OH} + \text{M}$	2.951E+14	0.00	48430.0
R16	$\text{H} + \text{H}_2\text{O}_2 \rightleftharpoons \text{OH} + \text{H}_2\text{O}$	0.241E+14	0.00	3970.0
R17	$\text{H} + \text{H}_2\text{O}_2 \rightleftharpoons \text{H}_2 + \text{HO}_2$	0.482E+14	0.00	7950.0
R18	$\text{O} + \text{H}_2\text{O}_2 \rightleftharpoons \text{HO}_2 + \text{OH}$	9.550E+06	2.00	3970.0
R19	$\text{OH} + \text{H}_2\text{O}_2 \rightleftharpoons \text{H}_2\text{O} + \text{HO}_2$	5.800E+14	0.00	9557.0

Methane–air chemical mechanism

Table 2: Reduced chemical mechanism by Smooke and Giovangigli [65] with rate coefficients $k_f = AT^\beta \exp(-E_0/RT)^1$. For rich mixtures, DRM mechanism [66] was used. Detailed GRI 3.0 mechanism was used for validation of FWI results [71].

No.	Reaction	A	β	E_0
R1	$\text{H} + \text{O}_2 \rightarrow \text{OH} + \text{O}$	2.00E+14	0.0	16800.0
R2	$\text{O} + \text{H}_2 \rightarrow \text{OH} + \text{H}$	1.80E+10	1.0	8826.0
R3	$\text{H}_2 + \text{OH} \rightarrow \text{H}_2\text{O} + \text{H}$	1.17E+09	1.30	3626.0
R4	$\text{OH} + \text{OH} \rightarrow \text{O} + \text{H}_2\text{O}$	6.00E+08	1.300	0.0
R5	$\text{H} + \text{O}_2 + \text{M} \rightarrow \text{HO}_2 + \text{M}$	2.30E+18	-0.80	0.0
R6	$\text{H} + \text{HO}_2 \rightarrow \text{OH} + \text{OH}$	1.50E+14	0.000	1900.0
R7	$\text{H} + \text{HO}_2 \rightarrow \text{H}_2 + \text{O}_2$	2.50E+13	0.0	700.0
R8	$\text{OH} + \text{HO}_2 \rightarrow \text{H}_2\text{O} + \text{O}_2$	2.00E+13	0.0	1000.0
R9	$\text{CO} + \text{OH} \rightarrow \text{CO}_2 + \text{H}$	1.51E+07	1.30	-758.0
R10	$\text{CH}_4 + (\text{M}) \rightarrow \text{CH}_3 + \text{H} + (\text{M})$	2.30E+38	-7.0	114363.0
R11	$\text{CH}_4 + \text{H} \rightarrow \text{CH}_3 + \text{H}_2$	2.20E+04	3.0	8750.0
R12	$\text{CH}_4 + \text{OH} \rightarrow \text{CH}_3 + \text{H}_2\text{O}$	1.60E+06	2.10	2460.0
R13	$\text{CH}_3 + \text{O} \rightarrow \text{CH}_2\text{O} + \text{H}$	6.80E+13	0.0	0.0
R14	$\text{CH}_2\text{O} + \text{H} \rightarrow \text{HCO} + \text{H}_2$	2.50E+14	0.0	10500.0
R15	$\text{CH}_2\text{O} + \text{OH} \rightarrow \text{HCO} + \text{H}_2\text{O}$	3.00E+13	0.0	167.0
R16	$\text{HCO} + \text{H} \rightarrow \text{CO} + \text{H}_2$	4.00E+13	0.0	0.0
R17	$\text{HCO} + \text{M} \rightarrow \text{CO} + \text{H} + \text{M}$	1.60E+14	0.0	14700.0
R18	$\text{CH}_3 + \text{O}_2 \rightarrow \text{CH}_3\text{O} + \text{O}$	7.00E+12	0.0	25652.0
R19	$\text{CH}_3\text{O} + \text{H} \rightarrow \text{CH}_2\text{O} + \text{H}_2$	2.00E+13	0.0	0.0
R20	$\text{CH}_3\text{O} + \text{M} \rightarrow \text{CH}_2\text{O} + \text{H} + \text{M}$	2.40E+13	0.0	28812.0
R21	$\text{HO}_2 + \text{HO}_2 \rightarrow \text{H}_2\text{O}_2 + \text{O}_2$	2.00E+12	0.0	0.0
R22	$\text{H}_2\text{O}_2 + \text{M} \rightarrow 2\text{OH} + \text{M}$	1.30E+17	0.0	45500.0
R23	$\text{H}_2\text{O}_2 + \text{OH} \rightarrow \text{H}_2\text{O} + \text{HO}_2$	1.00E+13	0.0	1800.0
R24	$\text{OH} + \text{H} + \text{M} \rightarrow \text{H}_2\text{O} + \text{M}$	2.20E+22	-2.0	0.0
R25	$\text{H} + \text{H} + \text{M} \rightarrow \text{H}_2 + \text{M}$	1.80E+18	-1.0	0.0

¹ coefficients are from [72].